

Small-scale spatio-temporal dynamics of snowmelt and its influence on runoff generation in a high Alpine catchment

THÈSE N° 8559 (2018)

PRÉSENTÉE LE 28 JUIN 2018

À LA FACULTÉ DE L'ENVIRONNEMENT NATUREL, ARCHITECTURAL ET CONSTRUIT
LABORATOIRE DES SCIENCES CRYOSPHERIQUES
PROGRAMME DOCTORAL EN GÉNIE CIVIL ET ENVIRONNEMENT

ÉCOLE POLYTECHNIQUE FÉDÉRALE DE LAUSANNE

POUR L'OBTENTION DU GRADE DE DOCTEUR ÈS SCIENCES

PAR

Tristan Jonas BRAUCHLI

acceptée sur proposition du jury:

Prof. J.-L. Scartezzini, président du jury
Prof. M. Lehning, Dr W. H. Huwald, directeurs de thèse
Prof. B. Schaefli, rapporteuse
Dr T. Jonas, rapporteur
Prof. A. Berne, rapporteur



ÉCOLE POLYTECHNIQUE
FÉDÉRALE DE LAUSANNE

Suisse
2018

Life is like riding a bicycle.
To keep your balance, you must keep moving.
— Albert Einstein

A ma maman, mon papa
A Valérie, à notre étoile filante et au futur toi. . .



Acknowledgements

First of all, I would like to sincerely thank Michi Lehning and Hendrik Huwald, my director and co-director respectively, for giving me this fantastic opportunity. I learned so many things during these five years: technical skills behind a computer or in the field, avalanche safety tricks but also the pleasure of assistantship and the mysteries of the academic world. Thank you for your help and your guidance throughout the thesis. I would also like to thank Ernesto Trujillo for all the good moments spent together including during long scans in the Dischma valley. Your help was really valuable and greatly contributed to this thesis. Finally, I would like to acknowledge the other members of my committee: Prof. Bettina Schaepli, Prof. Alexis Berne, Dr. Tobias Jonas and Prof. Jean-Louis Scartezzini. I especially appreciated the long and fruitful discussion during my private defense. These moments are not so frequent but very rewarding!

Research is often a question of team and I was extremely fortunate on that point with the most amazing group: *CRYOS*! I finish this adventure with so many good memories! Merci Aurélien pour ta collaboration et ton aide avec cette créature nommée *Alpine3D*. Même si cela n'a pas toujours été une partie de plaisir, c'était au moins agréable de pouvoir en parler ensemble. Et encore désolé pour cette journée infernale sur le terrain! Varun, thanks for so many things! Your sense of humor (or craziness...), your curiosity about our world, your encouragement (and relativism) and your help at the end of my thesis! Greatly appreciated! Comola, thanks for all the nice moments spent together and I will always be amazed by your cooking skills: how can you transform a zucchini and a tomato into an incredible pasta sauce? Thanks to Annelen, the tireless coach, I am really impressed by your energy (Jérôme, t'as bien du courage de la suivre)! It was a pleasure to share the office with you. Margaux, merci pour ta bonne humeur permanente! J'espère que tu trouveras rapidement ta voie. Merci Johan pour la "pointe" de folie que tu amènes en permanence au labo! Merci à Adrien pour les pauses syndicales à discuter des *Genferei* et autres rivalités valdo-genevoises. A la nouvelle génération, Adrien, Jérôme, Mahdi, Yasmine, profitez de cette belle expérience, même s'il

Acknowledgements

faut être un peu fou malgré tout! Merci à Jacques pour son aide lors de la construction des différents instruments de mesure. Jessica, merci de te battre à notre place contre le monde obscur de l'administration de l'EPFL. All the past glories, Natalya, Benoisif, Ernesto, Marco, Stuart, Isabelle, I am happy to have shared some time with you. Finally, I remember all the amazing bike rides to L'Isle with their sprint finish! Of course, at the end, a German always wins!

I would like to highlight the help I get from different civilists throughout my thesis. Nicolas, Arnaud, Antoine, Igor et Jonas. Merci à vous! I don't forget all the people from EFLUM lab with whom I discovered the joy of fieldwork in Val Ferret, was initiated to serious running and scientific tinkering. Thank you in particular to Raph, Steven, Théophile, Ciocca and Marc! I would also sincerely thank all the people from the surrounding labs at EPFL, the ECHO lab and their pasta, the SBER with their nice offices and people from SLF in Davos for their help and collaboration.

Une thèse, c'est beaucoup de travail, mais on n'est quand même pas des surhommes! Merci donc à Pierre, Flavio et Lorenzo de m'avoir permis de décompresser lors de diverses activités annexes qu'elles soient poudreuses, asphaltées, houblonnées ou apicoles. Je garde également de super souvenirs des nocturnes au Pralet et bien sûr du boui-boui thaï. Merci donc aux compagnons de sortie: Hugues et Flo, Tim, Claire, Valérie, Haldi et Xav! Il y a également eu tous ces weekends pour se changer les idées avec l'équipe *Jmbh* ou faire des réserves hivernales lors des Thanksgiving à Anzère. De très beaux souvenirs!

J'aimerais également remercier l'incroyable équipe du *Brame du Cerf*, Xavier, Davu et Greg, pour toutes les belles sorties en peau de phoque, avec une mention spéciale pour la fondue de l'igloo des Pantalons Blancs et évidemment la patrouille 2016. On a passé de super moments ensemble et cela restera des souvenirs inoubliables. Vivement les prochaines sorties!

Merci à Nans pour ton amitié de longue date. Malgré la distance et une vie bien occupée, tu as toujours été disponible pour aller skier, boire une bière ou organiser une partie de *crabing*! J'ai particulièrement apprécié nos nombreuses discussions parfois sans fin. Je suis vraiment admiratif de ta curiosité sans limite et de ta volonté!

Au final, si j'ai réussi ce parcours, c'est grâce à tout ce que vous, maman et papa, m'avez appris et aux valeurs que vous m'avez transmises. Merci, je n'aurais pas pu espérer mieux! Un grand merci également à toute ma famille qui a dû parfois supporter ma mauvaise humeur: Erel, Loris, Jasmine, Chantal, les Constantin, Carine et Vincent. Et un merci particulier à Sasha pour tous les chouettes moments passés ensemble, sauf au Gina ;-)

Finalement, un immense merci à toi, Valérie, pour ton soutien et ta patience presque sans fin. Une thèse n'est que rarement un long fleuve tranquille, la mienne a parfois ressemblé à un torrent de montagne lors de la fonte des neiges. On en est néanmoins sorti grandi! Les derniers temps nous ont rappelé que la vie ne se passe malheureusement jamais exactement comme prévu. Je suis convaincu que des moments heureux reviendront rapidement et je me réjouis de partager la suite de l'aventure avec toi!

Lausanne, Juin 2018

T. J. B.



Résumé

La neige est l'un des matériaux les plus complexes trouvés dans la nature. Dans les nuages, elle peut être vue comme des cristaux de différentes formes ou une ressource d'eau douce qui va finir sa course à la surface terrestre. Une fois au sol, elle peut être décrite comme une matrice thermodynamiquement instable ou un matériau fritté contenant des faiblesses structurelles qui peuvent engendrer des avalanches. A haute altitude ou latitude, la neige se transforme lentement en glace pure et fournit de la masse aux glaciers ainsi qu'aux calottes polaires. Finalement, elle peut aussi être vue comme un matériau relativement chaud proche de son point de fusion, qui va changer de phase en fondant et s'infiltrer dans le sol pour finalement se retrouver dans la rivière. Dans cette thèse, nous investiguons plusieurs aspects de cette dernière définition en suivant les particules d'eau du versant à la rivière. Le terrain d'expérimentation choisi est celui de la Dischma en Suisse.

En combinant un modèle à base physique et spatialement distribué avec des données expérimentales (lysimètre de neige, hauteur de neige, débit), nous examinons, dans les deux premiers chapitres, l'influence de la variabilité spatiale de la neige et du transport d'eau liquide dans le manteau neigeux sur la dynamique du débit. L'analyse, qui va de l'échelle locale à celle du bassin versant, démontre l'importance d'avoir un manteau neigeux réaliste au moment du maximum d'accumulation afin de modéliser précisément la réponse hydrologique à l'exutoire. La valeur ajoutée d'un module de transport d'eau liquide plus complexe dans le manteau neigeux est claire à l'échelle de la station mais diminue à plus large échelle. Nos résultats montrent non seulement l'importance mais aussi la difficulté d'obtenir une distribution des hauteurs de neige réaliste, même dans une région bien instrumentée. Cette étude présente également une validation à l'aide de jeux de données décrivant plusieurs échelles spatiales. De plus, nous montrons comment les flux d'énergie qui font fondre la neige changent au cours de l'année.

Abstract

Dans le troisième chapitre, nous mettons la modélisation de côté et investiguons expérimentalement la variabilité spatio-temporelle de la neige et de sa fonte. A l'aide d'un scanner terrestre longue distance, l'évolution de la couche de neige est mesurée à très haute résolution spatiale sur différentes pentes du bassin de la Dischma pendant la saison de fonte au printemps 2015. L'analyse des données révèle que la dynamique d'ablation à l'échelle de la pente suit une distribution bi-modale qui diverge au cours de la saison. L'origine de cette bi-modalité est expliquée par les facteurs limitants de la fonte de neige : l'énergie disponible et la masse de neige encore présente.

Pour conclure, nous nous éloignons du monde de la cryosphère mais continuons à étudier les échanges entre la surface terrestre et l'atmosphère. Dans le cadre d'un Observatoire Citoyen, nous avons développé un capteur bon marché de flux de chaleur sensible. L'instrument a été validé avec une référence de l'état de l'art. Le capteur montre des résultats prometteurs en donnant une bonne estimation du flux sensible sur plusieurs types de sol (herbe, gravier). Les limites du capteur actuel ainsi que ses potentielles améliorations sont discutées en détail. Grâce à son coût modéré, l'instrument a un grand potentiel : il pourrait être utilisé pour mesurer la variabilité spatiale du flux de chaleur sensible ou intégré dans un réseau de capteurs sans fil.

Mots clefs : fonte de neige, bassin versant alpin, terrain complexe, génération des débits, variabilité spatio-temporelle, distribution de la neige, scanner laser terrestre, modèle à base physique.



Abstract

Snow is one of the most complex materials occurring in nature. In clouds, it can be seen either as a crystal with various shapes or as a freshwater resource that will fall down to the Earth's surface. Once on the ground, it can be described as a thermodynamically unstable matrix or as a sintered material with inherent structural weaknesses that ultimately results in avalanches. At high elevations or latitudes, snow slowly transforms into pure ice and supplies mass to glaciers and polar ice caps. Finally, it can also be seen as a relatively warm material close to its fusion point that will experience a phase change, melt, and infiltrate into the ground, ultimately feeding a river system. In this dissertation, we investigate several aspects of the latter definition by following the water particles from the hillslope to the river network. The playground of these experiments is a high Alpine catchment, the Dischma river basin in Switzerland.

By combining a physically based and spatially distributed snow model with experimental data (snow lysimeter, snow depth, discharge), we examine, in the first two chapters, the influence of the spatial variability of snow and liquid water transport within the snowpack on runoff dynamics. The analysis, conducted from point scale to watershed scale, highlights the importance of having a realistic snowpack at peak accumulation to accurately model the hydrological response at the basin outlet. The added value of a more complex liquid water transport scheme is obvious at the site scale but decreases at larger scales. Our results highlight not only the importance but also the difficulty of getting a realistic snowpack distribution even in a well-instrumented area and present a model validation from multiscale experimental data sets. Additionally, we show how the energy fluxes driving the snow ablation change during the course of a year.

In the third chapter, we put the modeling part aside and investigate experimentally the spatio-temporal variability of snow and its melt. Using an ultra-long range Terrestrial Laser Scanner

Abstract

(TLS), we measure the evolution of the snow cover at a very high spatial resolution on different hillslopes of the upper Dischma valley during the 2015 ablation season. Data analysis reveals that the ablation dynamics at the slope scale follow a bi-modal distribution of ablation rate with diverging behavior during the course of the melt season. The emergence of this bimodality is explained on the basis of associated limiting factors: remaining snow mass and available energy for melt.

To conclude this dissertation, we move away from the cryospheric world but still study the energy exchanges between the Earth's surface and the atmosphere. In the framework of a Citizen Observatory, a low-cost sensible heat flux sensor was developed. The instrument was tested and validated against a state-of-the-art reference. The sensor shows promising results by giving good estimates over different surface types (grass, gravel). The limitations of the current sensor and potential improvements are also discussed in detail. Thanks to its low cost, the sensor has a great potential: it could be used to measure the spatial variability of sensible heat flux or be integrated within a Wireless Sensor Network.

Key words: Snowmelt, High Alpine Catchment, Complex Terrain, Runoff Generation, Spatio-temporal Variability, Snow Distribution, Terrestrial Laser Scanning (TLS), Physically Based Modeling.

Contents

Acknowledgements	v
Abstract (French/English)	vii
1 Introduction	1
1.1 The seasonal snow cover as a water resource	1
1.2 From snowflakes to water droplets	2
1.3 The Dischma River experimental watershed	4
1.4 Research questions and organization of the thesis	6
2 Influence of Slope-Scale Snowmelt on Catchment Response Simulated With the <i>Alpine3D</i> Model	9
2.1 Introduction	9
2.2 Study Area	11
2.3 Data	12
2.3.1 Snow Lysimeter	12
2.3.2 Meteorological Data	13
2.3.3 Discharge Data	14
2.3.4 Snow Depth Map	14
2.4 Models and Methods	15
2.4.1 <i>Alpine3D</i> setup	15
2.4.2 <i>StreamFlow</i> setup	16
2.5 Results	17
2.5.1 Snow Depths at Peak Accumulation	17
2.5.2 Site-Scale Comparison of Snow Accumulation and Melt	18
2.5.3 Snowmelt Dynamics at the Basin Scale	22
2.5.4 Hydrological Response	26
2.6 Discussion	28
2.7 Conclusions	30
2.8 Acknowledgments	31
3 Energy partitioning during the snowmelt season in a high Alpine catchment	33
3.1 Introduction	33
3.2 Methods	34

Contents

3.2.1	Snow energy balance	34
3.2.2	Model setup	35
3.3	Results	36
3.3.1	Snow depth	36
3.3.2	Hydrologic response	37
3.3.3	Melt energy	37
3.3.4	Melt energy partitioning	39
3.4	Discussion	40
3.5	Conclusions	41
4	Spatio-temporal variability of snowmelt observed with an ultra-long range Terrestrial Laser Scanner	43
4.1	Introduction	43
4.2	Methods and data	44
4.2.1	Study site	44
4.2.2	Instruments	46
4.2.3	Point cloud post-processing	47
4.3	Results	49
4.3.1	Snow depth change	49
4.3.2	Ablation rate	54
4.4	Conclusions	54
5	A low-cost Sensible Heat Flux sensor for Wireless Sensor Networks	59
5.1	Introduction	59
5.2	Materials and Methods	61
5.2.1	Flux Variance Method	61
5.2.2	Choice of the temperature sensor	63
5.2.3	Sensor interfacing	64
5.2.4	Eddy Covariance Method	67
5.2.5	Experimental Setup	68
5.3	Results	69
5.3.1	Comparison of temperature measurements	69
5.3.2	Comparison of sensible heat flux	73
5.4	Conclusions and Outlook	76
6	Conclusions and Outlook	79
A	Slope-Scale Snowmelt and Catchment Response	85
A.1	Supporting Information	85
B	Energy partitioning during the snowmelt season	91

C Spatio-temporal variability of snowmelt	93
C.1 Post-processing procedure of the TLS data	93
C.1.1 Correction of the inclination errors	93
C.1.2 Calculation of azimuth	95
D A low-cost Sensible Heat Flux sensor for WSN	97
D.1 Mathematical derivation of the 30-min variance	97
D.2 Comparison of temperature measurements	99
Bibliography	120
Curriculum Vitae	121

1 Introduction

1.1 The seasonal snow cover as a water resource

The cryosphere is a fundamental component of our planet. Through its thermal and radiative properties, it strongly influences the energy balance of the earth by reducing heat conduction, reflecting a large fraction of the incident solar radiation, and by emitting in the longwave range almost as a perfect blackbody (Geiger et al. [2003]). In addition, at the beginning of the 21st century, the cryosphere is still considered as the largest reserve of fresh water on earth (Rodda and Shiklomanov [2003]) and supplies this critical resource to natural ecosystems and, of course, to humans. This is particularly true in mountainous regions where a substantial part of the precipitation falls in a solid form and is stored as snow or ice for several months, years, or even decades (Beniston [1997]). Additionally, these regions get on average more precipitation than lowland areas (Viviroli and Weingartner [2004]). Due to these characteristics, mountains are symbolically named "water towers" of the world (Liniger et al. [1998], Viviroli et al. [2007]).

The available water mass and its seasonality have in turn strong impacts on the land surface. Plants and animals, constituting ecosystems, are continuously adapting themselves and evolving with the climate. In the Sierra Nevada mountain range, in the Western United States, Trujillo et al. [2012] showed that the vegetation greenness was directly related to snow accumulation during the antecedent winter. Westerling [2006] demonstrated that the wildfire activity in the Western U.S., observed during the last decades, was not only linked to the air temperature but also strongly related to the presence of snow. In particular, it was found that

earlier spring melt increased the wildfire frequency and their duration as well as prolonging the wildfire season. Many human activities are directly impacted by the snow cover and the water release when it melts. For example, the development of agriculture in dry areas of the Alps has been achieved thanks to the construction of complex irrigation systems taking water from rivers primarily fed by snow melt and glacier melt, conducting it to the fields (Crook and Jones [1999]). In the more recent past, the use of hydropower has allowed for a significant economic growth of entire regions of the Alps. In addition, winter tourism, and its associated snow sports, has been an important factor for the development for many rural and mountainous areas. The significance of the freshwater temporarily stored in the mountains becomes even more important for low altitude and often drier regions located downstream from the mountain ranges (Viviroli et al. [2007]) where this resource is essential for drinking water, irrigation and energy production (for exempling, the cooling system of a nuclear power plant or for hydropower).

It is expected and very likely that during this century, the cryosphere will change drastically due to the ongoing climate change ensuing from human activities (Barnett et al. [2005], Pachauri et al. [2014]). In mountainous regions at low elevations, the snowpack will be thinner or even disappear completely due to the rise of the 0° C isothermal altitude (Bavay et al. [2009]). As a result, the seasonal water storage will be reduced proportionally, negatively impacting the hydropower production (Schaepli et al. [2007]). In spring, snowmelt will start and end earlier, radically affecting the hydrological regime of rivers (Burn [1994], Horton et al. [2006]) by moving the maximum discharge earlier in the season. Climate change will coincidentally increase the water demand during the summer months for agriculture and industrial use resulting in additional stress on freshwater resources (Middelkoop et al. [2001], Addor et al. [2014]).

1.2 From snowflakes to water droplets

In mountainous terrain, the snowpack shows a very high spatial and temporal variability (Brown and Goodison [2006], Sturm and Benson [2004], Elder et al. [1991]). This heterogeneity is due to a combination of several processes taking place at different scales (Blöschl [1999]) and overlapping with each other. At the regional scale (~10-1000 km), complex interactions between air masses and mountain ranges lead to above-average amounts of precipitation as well as significant spatial gradients (Roe [2005], Isotta et al. [2014], Sevruk [1997]). At the watershed scale (~0.1-10 km), the local topography (valley, ridge) influences precipitation through orographic enhancement and preferential deposition (Lehning et al. [2008], Grünewald et al. [2014], Mott et al. [2014]). At the hillslope scale (~10-1000 m), snow redistribution by the wind (drifting, blowing) combined with gravitational influence (avalanche, sloughing) are dominant. Finally, at the point scale (<5 m), the snow cover is mainly shaped by the surface roughness and the local vegetation (Clark et al. [2011]).

Once on the ground, the snowpack undergoes metamorphic changes driven by internal temperature and vapor gradients (Colbeck [1982]). These phenomena are due to energy

exchange between the snow and its environment. In fact, the local energy balance varies significantly as a function of seasonal and diurnal variations in energy input (solar radiation), but also spatially due to shading by clouds or induced by the rugged terrain and the radiative properties of snow, e.g. reflection and emission from surrounding slopes (Lehning [2006], Male and Granger [1981], Marks and Dozier [1992]). The presence of vegetation, either low shrubs or a forest canopy, modifies the micro-meteorological conditions (e.g. albedo, surface roughness, wind profile, etc., see Harding and Pomeroy [1996]), and most importantly interferes with snow when it is falling or transported by the wind during snow drift. This results in interception of potentially significant amounts of snow on the vegetation with important implications on the energy balance.

All these processes lead to a non-uniform snowpack (in term of mass, energy and internal properties) and consequently will generate inhomogeneous snowmelt as soon as sufficient energy is added to the system. These circumstances are nicely illustrated in Figure 1.1a showing two hillslopes with opposite aspects in the Dischma valley (Davos, Switzerland) having experienced differential melt after an early snowfall in October 2015. The patchy nature of the snow cover makes the system even more complex (Figure 1.1b): the snow-free terrain has different radiative properties (lower albedo) and thus increases the energy input also of the snow-covered area through turbulent sensible heat transfer finally enhancing local melting (Mott et al. [2013, 2015], Grünewald et al. [2010]). Moreover, the snow disappearance initiates a positive feedback loop as more bare ground becomes uncovered. From a hydrological point of view, the response is much more complex than in a rain-fed basin, where the output is proportional to the direct mass input from the atmosphere. In snowmelt- or glacier-fed watersheds, the hydrological response is a complex combination of the mass accumulated during the winter and the spatially distributed energy balance varying as a function of local topography (Lundquist and Dettinger [2005], Woo [2006]).



Figure 1.1 – Illustration of the spatial snow variability captured in the Dischma valley. a) Differential melt between south- and north- facing slopes in the Rinertaelli side valley. October 2015. b) Patchy snow cover in the headwater catchment during the melt season. May 2015.

1.3 The Dischma River experimental watershed

The Dischma River basin has been selected as the experimental watershed for this study and is located in the Swiss Alps near the town of Davos, (Figure 1.2). This high-alpine catchment, covering an area of 43.2 km^2 with an elevation range from 1668 to 3146 m, is an ideal testbed for studying snow accumulation, snow melt processes and the resulting hydrological response. Situated in the inner Alpine region, the basin is rather sheltered compared to northern or southern flanks of the Alps and receives relatively limited amounts of precipitation (Frei and Schär [1998], Sevruk [1997]). The land use is characteristic of the mountainous areas with subalpine meadows, bare soils or bedrock but limited forested area (FOEN [2017]) due to the local tree line at around 2000 m. At the southern end of the catchment, a small glacier, the "Scalettagletscher", is located on a north-facing, high-altitude slope, covering only 2% of the total surface. The Dischma river ("Dischmabach" in German) has the particularity of having two headwaters: the first one is located close to the "Scalettapass" on the southwestern border of the catchment and the second one at a place called "Fuorcla da Grialetsch" on the southeastern edge (see Figure 1.2). The two streams merge just upstream of the "Duerrboden" site. The Dischma river itself joins the Landwasser river in Davos, which is part of the Alpine Rhine basin and thus eventually leads into the North Sea.

The vicinity of the Institute for Snow and Avalanche Research (SLF) in Davos has certainly contributed to its popularity as a major scientific site for conducting snow-related studies investigating, for example, avalanche processes (Baggi and Schweizer [2009]), rain-on-snow events (Juras et al. [2017]) or for testing new snow depth mapping techniques using photogrammetry and drones (Bühler et al. [2015, 2016]). From 2014 to 2017, the Dischma Valley Experiment ('Dischmex') investigated the land-atmosphere interactions during the winter and spring seasons. Gerber et al. [2017] studied how the flow field is influencing the snow accumulation over a ridge during a snow storm. To do so, they not only used remote sensing techniques (Doppler Wind Lidar and Terrestrial Laser Scanner (TLS)) to measure the wind field and the snow accumulation but they also modeled it with the help of a combined land-atmosphere model chain. During the same experiment, Mott et al. [2017] investigated the snow ablation dynamics at smaller scale using eddy covariance measurements and TLS data. They showed how, under certain conditions, a patchy snow cover can influence the lower atmospheric boundary layer by decoupling it from the air above and reducing the sensible heat flux exchanges toward the snowpack.

In the Dischma valley, alpine ecology, notably the dynamics of the protection forest, has been a significant area of research at the treeline study site "Stillberg" (Barbeito et al. [2012], Wipf et al. [2009]). This site is equipped with a long-term weather station (1975-present) measuring standard meteorological and snow variables together with short- and longwave radiation (Bebi [2016]). The "Weissfluhjoch" study site, operated by the SLF Institute since 1936, also provides a comprehensive dataset of the snow-related and meteorological variables (WSL Institute for Snow and Avalanche Research SLF [2015, 2018]). From the Dischma outlet, this site is at a distance of only 7 km on the mountain range north of Davos. Last but not the least, the SLF Institute is operating and maintaining a high-altitude automatic weather station network

1.3. The Dischma River experimental watershed

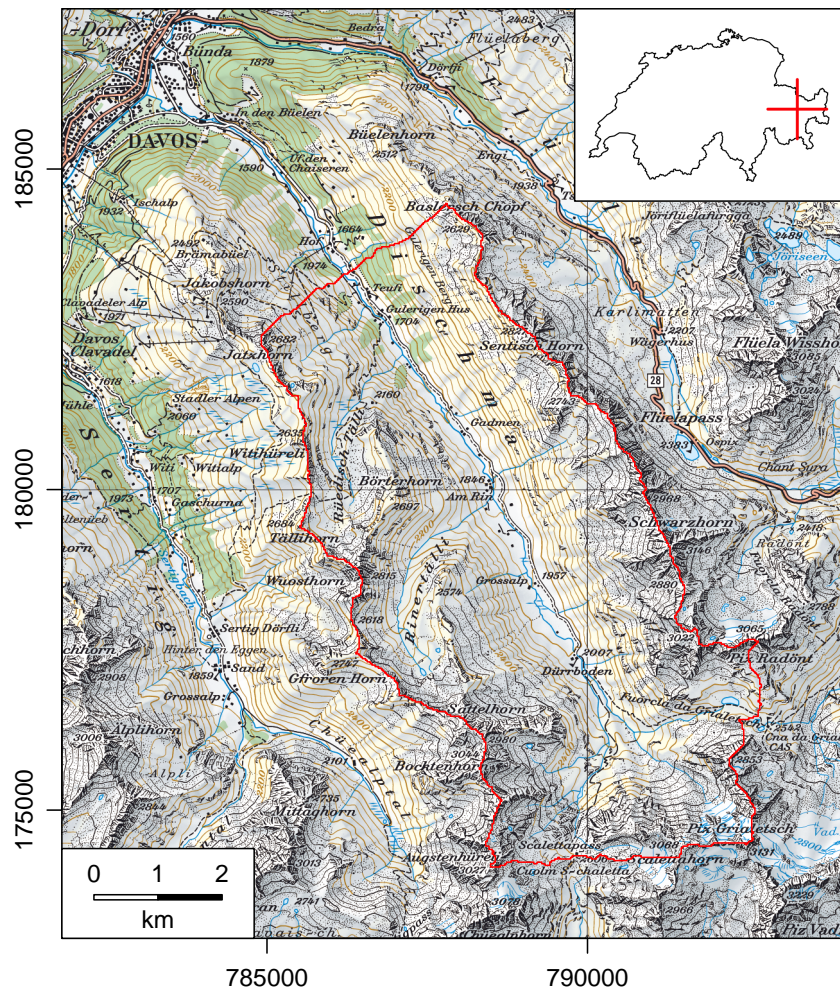


Figure 1.2 – The Dischma river basin (delineated in red) and its surroundings. Reproduced with permission from swisstopo (JA110138).

called *IMIS* (Intercantonal Measurement and Information System) originally designed for the avalanche warning service in Switzerland (Lehning et al. [1998]). Several IMIS stations are located around the Dischma basin. Each site is composed of a snow station located on a flat and sheltered terrain and a wind station installed on a nearby mountain ridge, measuring the following variables: air temperature, relative humidity, wind speed and direction, snow depth, reflected shortwave radiation, surface temperature, soil temperature and temperature at three different levels within the snowpack. Due to power constraints, sensors are neither heated nor ventilated. Data from all the described stations are a fundamental base for any snow-related research in the region.

The Swiss Federal Office for the Environment (FOEN) has defined the Dischma basin as a Hydrological Study Area of Switzerland (FOEN [2018]). The aim of this network covering different climatic regions of the country is observing long-term changes in the natural hydrological

regimes. For that reason, the discharge of the Dischmabach has been monitored since 1964 at the basin outlet "Kriegsmatte". The water level is measured over a concrete weir and then converted into discharge applying a specific rating curve (FOEN [2017]). The catchment has been subject of extensive hydrological research over the past decades, including the pioneering work of Martinec [1975, 1980] and Martinec and Rango [1987] who combined a temperature index model with snow-cover depletion curves derived from Landsat images. More recently, Zappa et al. [2003] evaluated the seasonal water balance of the Dischma river basin with different model setups (degree-day, simplified energy balance and full energy balance approaches). Schaepli [2016] proposed new hydrological signatures based on air/water temperature for constraining parameter choice during model calibration and applied them in the Dischma catchment.

Given all the above-mentioned instrumentation, this watershed qualifies as an exceptionally well monitored and studied catchment. To complement the existing networks, we set up some specific instruments to address snowmelt dynamics in the Dischma valley in particular. Firstly, we installed snow lysimeters on different slopes (Figure 1.3a) to monitor the spatial variability of snowmelt. These instruments, embedded in the ground, measure the liquid water output at the base of the snowpack (Kattelmann [1984], Kinar and Pomeroy [2015]). For the present research, we designed and built our own lysimeter using a tipping bucket rain gauge and a collecting funnel (see Subsection 2.3.1 for more details). The design was inspired by the instrument used by Würzer et al. [2016]. The choice of the installation site is crucial: it must be representative of the hillslope in terms of aspect and snow accumulation but most importantly it must be outside potential avalanche tracks. In addition, we learned a posteriori that the water table can "flood" our instrument from below during the snowmelt, which led to malfunctioning but also to a better knowledge of the ground water dynamics. Secondly, we installed two pressure sensors in streams (Figure 1.3b) to measure the hydrological response of the sub-basins. The first one is located in "Duerrboden" on the main river and is monitoring the headwaters of the Dischma basin (12.1 km^2 , 28% of the total area). The second one is installed on a small tributary (close to the hamlet "Am Rin", Figure 1.2) monitoring the "Rinertalli" side valley (4.3 km^2 , 10% of the entire basin). To convert the pressure data into discharge, we applied the salt tracer method (Day [1976]) for a wide range of water levels and established a rating curve for each site.

1.4 Research questions and organization of the thesis

The goal of this dissertation is to improve the understanding of snowmelt dynamics and its influence on timing and magnitude of river discharge in a high Alpine catchment. To this end, several stages of the water travel from the hillslope to the river have to be investigated. Starting from its solid form in the alpine landscape, the ablation of the snow cover in space and time needs to be measured in an extensive season-long field campaign. This research attempts to measure slope-scale snow depth using repeated terrestrial laser scanning (TLS) from peak accumulation throughout the ablation season. Upon the onset of the melt season, detailed and time-resolved measurements of the liquid water flux at the snow-soil interface

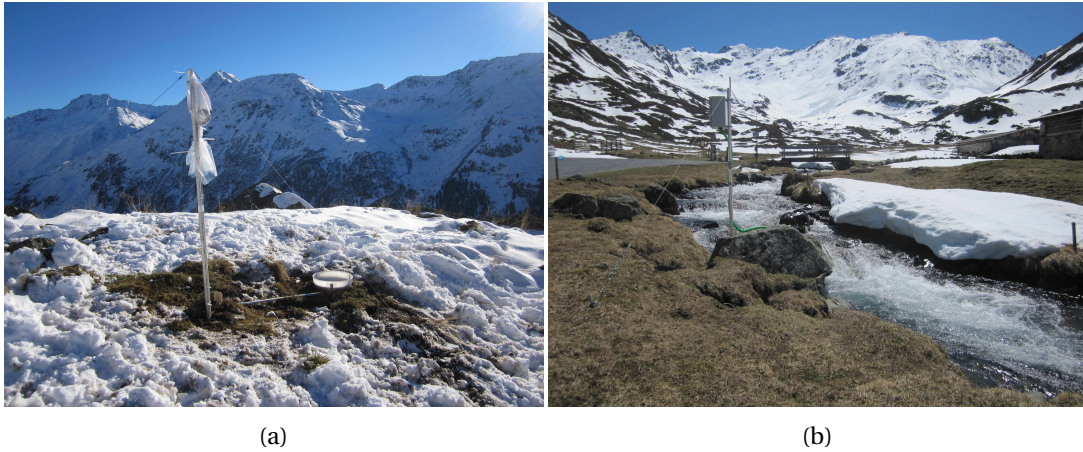


Figure 1.3 – Instruments installed in the Dischma valley. a) A snow lysimeter just after the first snowfall of the winter. October 2015. b) Water level gauge installed in Duerrboden to monitor the headwaters. May 2015.

are necessary which is planned using custom-made snow lysimeters. Finally, before water is leaving the catchment, the discharge at a defined gauging point needs to be quantified. The combination of a large, multi-source observational data set with an advanced numerical snow model are expected to provide a better understanding of this complex system. The present thesis addresses these questions in 4 chapters and is organized as follows:

- **Chapter 2** examines how the spatial variability of snow, as a function of topography, and liquid water transport within the snowpack influences runoff dynamics. For this study, a dual approach is applied, combining the physically based and spatially distributed snow model *Alpine3D* (Lehning et al. [2006]) and its hydrological extension *StreamFlow* (Gallice et al. [2016]), with multiscale observations of the snowpack and its melt dynamics (snow lysimeter, distributed snow depths, discharge at several locations). To obtain the most realistic snow distribution, a classical interpolation scheme relying only on rain gauge observations is compared to a more advanced approach assimilating a snow depth map proposed by Vögeli et al. [2016]. In addition, two liquid water transport schemes in the snowpack are compared to evaluate the respective influence on water percolation and performance of the approaches implemented in the model: (a) the bucket approach and (b) the Richards equation recently implemented for snow by Wever et al. [2014]. We investigate these differences at different spatial scales (plot, subcatchment/hillslope, and catchment).
- **Chapter 3** builds on the previous chapter using the same model setup but an extended time period from 2002 to 2016. The objective here is to perform a long-term physically based simulation of the Dischma river basin to test the robustness of such a model chain coupling *Alpine3D* and *StreamFlow*. The chapter further investigates the energy balance during the snowmelt season at the basin scale to identify the dominant components and to study the inter-annual variability of these fluxes.

- The research presented in **Chapter 4** is exclusively based on observational data and investigates experimentally the spatio-temporal variability of the snow cover and its melt dynamics. The recent development of terrestrial remote sensing techniques opens up new horizons for observing and monitoring the cryosphere and in particular the snow cover. The use of an ultra-long range Terrestrial Laser Scanner (TLS) is expected to provide spatially distributed information on the snow cover on the hillslopes in the upper Dischma river basin targeting slopes of different aspect and large elevation ranges. During the 2015 snowmelt season, we perform multiple scans beginning with peak accumulation in April until mid-June. Comparing multiple TLS measurements from different moments over a snowmelt season enable estimates of snow ablation that has occurred between individual surveys. Thanks to the large spatial resolution of such scans, it is possible to observe small-scale features that are not captured with traditional surveying techniques.
- **Chapter 5** may appear as an outlier with respect to the main topic of the dissertation as it deals with the development and testing of a new low-cost sensible heat flux sensor. This work was carried out in the framework of the EU FP7 project *WeSenseIt* (Ciravegna et al. [2013]). The main goal of this project was the implementation of a "Citizen Observatory of water" and water-related variables to monitor the different components of the water cycle. In this framework, several instruments were provided to the citizens, namely water level gauges, rain gauges, snow depth gauges and low-cost automatic weather stations. While flood risk management was a principal objective, the project endeavored to tackle other challenges in environmental sensing. In a warming climate, water scarcity will become a major problem notably for agriculture and natural ecosystems. However, the independent measurement of all surface energy balance components is rare mainly for cost reasons. This motivated an initiative to go beyond traditional water variables and develop a low-cost sensible heat flux sensor applying the flux variance method based on convective scaling (Albertson et al. [1995]). This chapter presents the development of the sensible heat flux sensor, its testing and validation against reference instrumentation (sonic anemometer using the eddy covariance method), and the results from the field experiments in real outdoor conditions.
- Finally, the **Conclusions** summarize the main findings of this thesis and present some outlook for future research on snowmelt and how it controls runoff.

2 Influence of Slope-Scale Snowmelt on Catchment Response Simulated With the *Alpine3D* Model

An edited version of this chapter was published in *Water Resources Research*:

Brauchli T., Trujillo E., Huwald H., Lehning M., 2017: Influence of Slope-Scale Snowmelt on Catchment Response Simulated With the Alpine3D Model, *Water Resources Research*, **53**, 10723–10739. doi:10.1002/2017WR021278

2.1 Introduction

Snow is an essential component of the hydrologic cycle of mountain regions across the globe (Beniston [1997], Serreze et al. [1999]). Mountain snowpacks are a major water resource for regional ecosystems, groundwater recharge, human consumption, agriculture, and hydropower, among others. The hydrology of mountain regions is expected to be strongly affected by climate change (Barnett et al. [2005], Stewart [2009]), with shorter snow seasons and reduced snowpack storage (Bavay et al. [2009], Burn [1994], Horton et al. [2006]) and slower melt as a result of earlier snowmelt seasons (Marty et al. [2017], Musselman et al. [2017]). These changes in snow regimes can have a negative impact for hydropower production (Schaepli et al. [2007]), winter sports (Schmucki et al. [2015], Scott et al. [2008]) and mountain forests (Trujillo et al. [2012], Westerling [2006], Bales et al. [2011]), evapotranspiration, and carbon uptake (Winchell et al. [2016]).

Chapter 2. Influence of Slope-Scale Snowmelt on Catchment Response Simulated With the *Alpine3D* Model

Accurate snowpack modeling is paramount to properly understand how these expected changes in climate affect snowpack processes in mountain regions (Bales et al. [2006], Viviroli et al. [2011]). However, significant challenges in snow modeling still exist because of the complexity of snow processes across multiple scales (Blöschl [1999], Clark et al. [2011]). Snow accumulation and melt are highly variable in space and time and are difficult to represent in snow models (Dozier [2011]). Precipitation is very heterogeneous featuring complex patterns both at regional and watershed scales (Roe [2005], Sevruk [1997], Mott et al. [2014], Sommer et al. [2015]). Wind, topography, and vegetation control deposition and redistribution of snow, impacting the distribution patterns across scales (Grünewald et al. [2014], Lehning et al. [2008], Mott et al. [2014], Schirmer et al. [2011], Trujillo et al. [2007, 2009]). Following deposition, snow distribution is affected by avalanching and sloughing (Blöschl and Kirnbauer [1992]), radiation processes controlled by seasonal changes in temperature, solar radiation, cloud cover, topographic shading, and snow radiative properties (Lehning [2006], Marks and Dozier [1992]). Vegetation influences the mass and energy balance by modifying the micrometeorological conditions and changing the radiative fluxes (Harding and Pomeroy [1996]). All these processes lead to highly heterogeneous snow distribution and snow physical properties. As a result, energy balance and snowmelt processes are also heterogeneous in space. This heterogeneity is accentuated later in the snowmelt season by the patchy nature of the snow cover modifying radiative and turbulent heat fluxes, and ultimately snow melt (Grünewald et al. [2010], Mott et al. [2013]). The hydrological response is then no longer proportional to the direct mass input from the atmosphere but rather to the combination of locally accumulated mass and the site specific energy balance (Lundquist and Dettinger [2005], Woo [2006]).

Physically based snow models (e.g., *Crocus* (Brun et al. [1989]), *Isnobal* (Marks et al. [1999]) and *SNOWPACK* (Lehning et al. [1999])) have become increasingly popular due to the availability of higher quality and higher (spatial) density of required meteorological input, and improvements in modeling and numerical methods. Better validation through recent snow measuring techniques and remote sensing technologies has also increased acceptance of more complicated models (e.g., Wever et al. [2017]). While computationally intensive and often more vulnerable to data quality issues (Schlögl et al. [2016]), these models require reduced parameter calibration and are expected to be more reliable when extrapolated to different conditions (e.g., climate change scenarios) or interpolated spatially over a larger region (Essery et al. [2009], Etchevers et al. [2004]). However, complexity increases along with the necessity to accurately model some of the detailed processes involved at the range of scales over which the processes take place (Blöschl [1999]). The spatial resolution will define which processes are explicitly resolved and which ones are parameterized or simply not represented (Clark et al. [2011]). In many cases, the computing power still remains a limiting factor.

In the present study, we assess the impact of recent developments in the physically based *Alpine3D* model (Lehning et al. [2006]) on snowpack simulation and its melt. The objective of this study is to analyze the ability of *Alpine3D* to reproduce the snow cover evolution across multiple scales. Two recent advances are of particular interest for studying the hydrological response. First, Wever et al. [2014] implemented the Richards equation to model the liquid

water transport in the snow cover. Second, Vögeli et al. [2016] proposed a new methodology that assimilates snow depth measurements in the precipitation interpolation scheme. We assess the impact of these new schemes by comparing model output to different experimental field data. In particular, we carry out detailed multiscale (plot, subcatchment/hillslope, and catchment) analyses of heterogeneity in snow cover and snowmelt patterns and their consequences on timing and magnitude of streamflow. The study focuses on spatial scales relevant for the accurate representation of the hydrological response of a complex high-alpine headwater catchment, the Dischma River basin in Switzerland (Figure 2.1), during the water year 2014-2015. Two components of the modeling system are instrumental for the analysis: (1) *Alpine3D*, the spatially distributed version of *SNOWPACK*, enables a detailed representation of the atmosphere-vegetation-soil continuum. It has been extensively used for studying the snow cover evolution (Comola et al. [2015b], Schmucki et al. [2014]), its sensitivity to climate change (Bavay et al. [2013, 2009]), snow transport (Mott et al. [2010]), and glacier hydrology (Michlmayr et al. [2008]). (2) The *StreamFlow* model (Gallice et al. [2016]), which coupled to *Alpine3D*, enables simulation of hydrological response at the catchment scale.

2.2 Study Area

The Dischma River basin (Figure 2.1) covers an area of 43.2 km² with an elevation range between 1,668 and 3,146 m (mean: 2,372 m). The basin has a SE-NW orientation, with two dominating hillslopes facing northeast and southwest, respectively. The headwaters of the catchment form a north-facing bowl with a small glacier (0.9 km², 2.1% of the contributing area) at the highest elevations. On the southwest side of the main valley, there are two small subwatersheds with north- and south-facing slopes. The land cover is representative of the alpine region: 36% of the valley is covered by subalpine meadows; bare soil and exposed bedrock cover about 50% of the basin; forest and shrubs less than 10%. On the hillslopes, soils (mainly Orthents, Rankers, and Entisols) are relatively shallow (<0.50 m on average), highly permeable (mean hydraulic conductivity: 4.3×10^{-4} m s⁻¹), and with limited water retention capacity (mean: 17.8 mm; FOEN [2017]). Deeper soils (Fluents) are found along the valley bottom with a more significant groundwater storage (Gurtz et al. [2003]). The geological bedrock is mainly composed of crystalline rocks (orthogneiss, paragneiss, and amphibolites; Verbunt et al. [2003]).

From a climatological point of view, the Dischma catchment is located at the border between the wetter northern flank of the Alps and the drier inner-alpine area (Frei and Schär [1998]). Due to its position, the basin is rather sheltered and receives below-average precipitation (mean annual precipitation in Switzerland (1961-1990): 1,458 mm; Spreafico and Weingartner [2005]). The mean annual precipitation in Davos (located at 1,594 m and 5 km northward) over the period 1974-2015 amounts to 1,039 mm yr⁻¹. At "Kesch" hut, located at 2,570 m southwest of the Dischma basin, the average annual precipitation is 1,251 mm yr⁻¹ over the same period. The resulting altitudinal gradient of 22 mm/100 m (or 2%/100 m) is small for the alpine region but in agreement with corresponding values in the literature (Sevruk [1997]). Finally, evapotranspiration is moderate (~250 mm yr⁻¹; Menzel et al. [1999]).

Chapter 2. Influence of Slope-Scale Snowmelt on Catchment Response Simulated With the *Alpine3D* Model

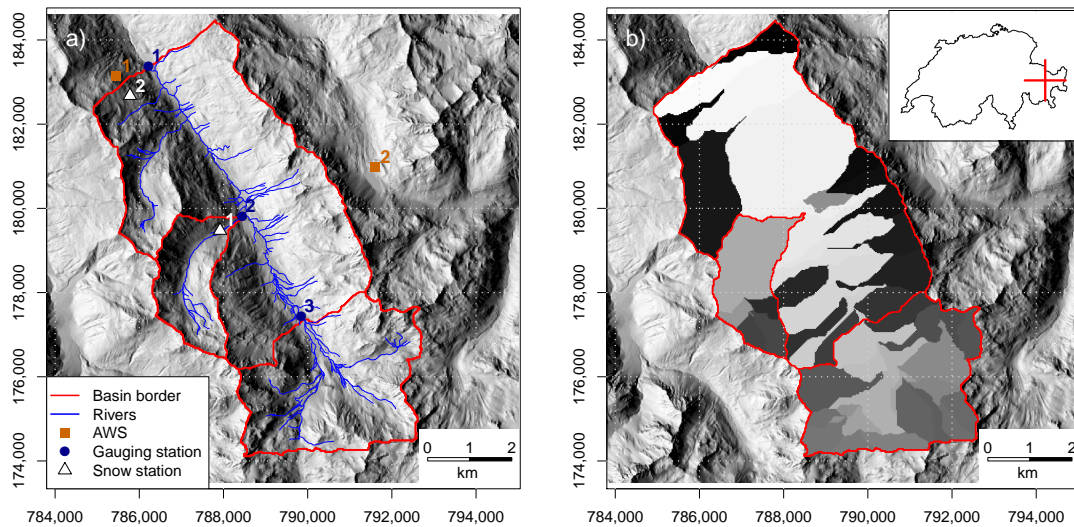


Figure 2.1 – **a)** The Dischma River basin and the two monitored subcatchments are delineated in red with their outlet in dark blue: (1) Kriegsmatte, (2) Am Rin, and (3) Duerrboden. White triangles indicate the snowmelt lysimeter stations: (1) the Rinertaelli site and (2) the Stillberg site. Automatic weather stations are marked with orange squares: (1) the Stillberg *IMIS* station and (2) the Fluelapass *IMIS* station. The river network is shown in blue. **b)** The Dischma River basin divided into 55 subbasins for hydrological modeling. Reproduced with permission from *swisstopo* (JA110138).

The hydrological regime is glacio-nival (Aschwanden et al. [1985]) with low flows during winter and high flows in springtime and summer due to snow and ice melt. During this period, the diurnal variation in energy input mainly controls the magnitude and timing of the discharge. The mean annual discharge over the period 1961-1980 was $1,245 \text{ mm yr}^{-1}$ (Schädler and Weingartner [1992]).

2.3 Data

2.3.1 Snow Lysimeter

Snow lysimeters were deployed to quantify water output at the base of the snowpack and to detect the onset of the melting season. This type of instrumentation has been used in multiple snow studies to measure runoff from snowmelt (Kinar and Pomeroy [2015]). Permanent instrumentation generally have larger collecting areas to increase data representativeness (Kattelmann [2000]), which is especially important for heavily stratified and heterogeneous snowpacks. For this study, nonpermanent instruments of smaller size (0.45 m of diameter) were deployed with a setup similar to Würzler et al. [2016] (Figure 2.2). Instrument sites are indicated in Figure 2.1a: (a) on a south-facing slope in the "Rinertaelli" side-valley and (b) on a northeast-facing slope close to the "Stillberg" weather station. The two sites are chosen at a similar elevation in order to facilitate direct comparison: differences in snow accumulation and melt are mainly influenced by aspect and topography.

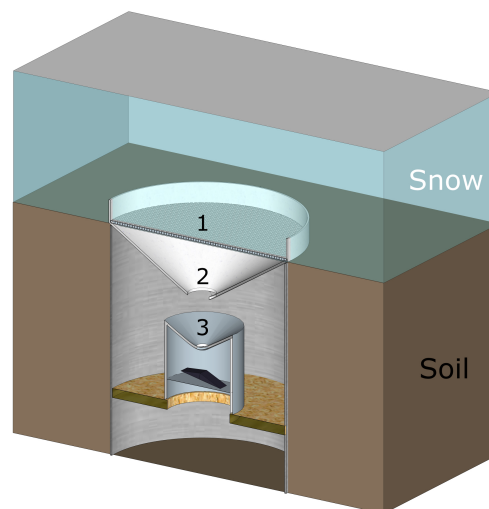


Figure 2.2 – Illustration of a snow lysimeter: the instrument is buried into the ground and collects melt water from the snowpack through a stainless steel sieve cover (1) in a funnel (2). The output signal is measured through a standard rain gauge (3). A rim with 5 cm depth prevents any lateral inflow at the snow-soil interface.

2.3.2 Meteorological Data

For the chosen configuration (detailed in Section 2.4.1), *Alpine3D* requires the meteorological variables listed in Table 2.1. Two networks are used to complement the required data in the Dischma catchment area:

1. The Swiss Federal Office of Meteorology, *MeteoSwiss*, operates an automatic weather station (AWS) network covering the entire country. In the Dischma area, two stations are used: (i) "Davos" (DAV) and (ii) "Weissfluhjoch" (WFJ) on the mountain range northward of Davos. Data analysis of the precipitation time series (1974-2015) revealed that the WFJ rain gauge recorded consistently more precipitation than the storage precipitation gauge in "Kesch" hut ($1,359 \text{ mm yr}^{-1}$ at WFJ versus $1,251 \text{ mm yr}^{-1}$, $\Delta P = 108 \text{ mm}$ or 9%) located at similar elevation 20 km southward. These differences can be explained by the north-south precipitation gradient discussed in Section 2.2. Therefore, we only used precipitation amounts from the "Davos" station and applied an altitudinal gradient estimated from the difference between the DAV station and the "Kesch" hut.
2. The Inter-cantonal Measurement and Information System (*IMIS*) is a network of AWS covering high-altitude areas (2,500-3,500 m) in Switzerland (Lehning et al. [1999]). As a result of limited power supply, *IMIS* station sensors are not heated or ventilated. The stations located around the Dischma catchment are listed in Table 2.1, two of them are shown in Figure 2.1a. It is worth noting that these snow depth measurements are only used for validation purposes.

Chapter 2. Influence of Slope-Scale Snowmelt on Catchment Response Simulated With the *Alpine3D* Model

Table 2.1 – Automatic Weather Stations (AWS), Position (Easting/Northing in Geodetic Datum CH1903), and Measured Meteorological Variables (TA, Air Temperature; RH, Relative Humidity; WV, Wind Speed; ISWR, Incoming Shortwave Radiation; ILWR, Incoming Longwave Radiation; P: Precipitation; HS: Snow Depth) Part of the MeteoSwiss (MCH) and IMIS Networks. Variables marked with an 'x' are measured at that station and used in the modeling process. Notation 'V' means used for validation purposes only. The '+' are measured but not used in the modeling. The '-' signs indicate variables that are not measured at the weather station.

Station name / Type	Position (m)	Altitude (m)	TA	RH	WV	ISWR	ILWR	PSUM	HS
Weissfluhjoch (MCH + IMIS)	780'853 / 189'229	2540	x	x	x	x	x	+	V
Davos (MCH)	783'514 / 187'457	1594	x	x	x	x	x	x	V
Davos - SLF (IMIS)	783'800 / 187'400	1560	x	+	x	-	-	-	V
Stillberg (IMIS)	785'455 / 183'136	2085	x	x	x	x	x	+	V
Puelscheggia (IMIS)	797'300 / 175'080	2680	x	x	x	-	-	-	V
Fluelapass (IMIS)	791'600 / 180'975	2390	x	x	x	-	-	-	V
Baerentaelli (IMIS)	782'100 / 174'760	2560	x	x	x	-	-	-	V

2.3.3 Discharge Data

The Swiss Federal Office for the Environment is monitoring discharge from the Dischma River catchment at the "Kriegsmatte" outlet (blue circle in Figure 2.1a), which is considered the reference discharge of the watershed. Two additional gauging stations were installed in early 2015 at upstream locations with the aim of capturing the hydrological response of subwatersheds with different geomorphological characteristics. The first station, "Am Rin", is located on a lateral tributary just before its confluence with the main stream (Figure 2.1a). The side-valley "Rinertaelli" covers an area of 4.3 km² (10% of the entire basin) and has southeast-facing and north-facing slopes. The second gauging station is "Duerrboden" on the main stream monitoring the headwaters of the Dischma River. This subwatershed is composed of a large cirque facing north and covering 12.1 km² (28% of the basin). Discharge was estimated using the salt dilution method (Day [1976]). A rating curve for each site was derived allowing for the transformation of water depth into discharge following Weijs et al. [2013].

2.3.4 Snow Depth Map

Digital surface models (DSM) were derived from stereo imaging captured by airborne digital sensors (ADS; Bühler et al. [2015]). Two flights covering the Dischma basin were carried out, one during summer (3 September 2013) and one close to peak accumulation (15 April 2015). The snow depth data set is obtained by subtracting the summer DSM from the winter surface.

The spatial resolution is 2 m and its accuracy ± 30 cm (Bühler et al. [2015]). The data set contains spatial gaps because of the limitations of ADS to measure snow height over buildings, vegetated areas, and water bodies. The data were then averaged over 100 m grid cells to match the *Alpine3D* grid. A minimum of 50% of valid data coverage was set as a threshold (similar to Vögeli et al. [2016]) to ensure consistency in the aggregated snow depths. This data set is used for validation of the modeled snow cover and is assimilated as a correction factor in the precipitation interpolation (Section 2.4.1).

2.4 Models and Methods

2.4.1 *Alpine3D* setup

The one-dimensional *SNOWPACK* model Lehning et al. [1999], Bartelt and Lehning [2002], Lehning et al. [2002b,a] computes the energy and mass balance of a multilayer snowpack and its underlying soil layers. Its spatially distributed version, *Alpine3D*, runs the same algorithm on a regular mesh grid without considering lateral exchange in the soil-snow-vegetation column. The model is run at a 15 min time step with a grid cell size of 100 m over a domain of 154 by 128 elements. The Dischma area is represented in terms of topography and land use by incorporating the digital elevation model and soil properties provided by the Federal Office of Topography. The turbulent heat fluxes are simulated based on Monin Obukhov (MO) similarity theory and stability corrections as described by Michlmayr et al. [2008]. The roughness length of the snow cover is set to 0.007 m. Vegetation influence is simulated with a two-layer canopy model developed for evergreen coniferous forests (Gouttevin et al. [2015]).

Interpolation of meteorological forcing data is carried out using meteoIO (Bavay and Egger [2014]). This module contains routines for spatio-temporal interpolation and filtering of erroneous data. This study uses the following model setup:

- For precipitation, data from *MeteoSwiss* station DAV are corrected for precipitation undercatch (Goodison et al. [1997]). Spatial interpolation is performed by applying a fractional lapse rate of 2%/100 m (see Section 2.2). The precipitation phase is determined based on an air temperature threshold of $+1.5^\circ\text{C}$; above this value all precipitation is considered liquid. The hillslope-scale snow variability is modeled by assimilating snow depth data in the precipitation interpolation scheme (Vögeli et al. [2016]). This method consists in applying a spatial correction factor to the precipitation field based on observed snow depth fields. This results in a more realistic snow height distribution while conserving the mass balance over the entire catchment. In practice, precipitation $P_{i,t}$ at a given grid point i and at time t is computed as follows:

$$P_{i,t} = \frac{HS_i}{HS_{avg}} \times P_{avg,t} \quad (2.1)$$

where $P_{avg,t}$ is the average interpolated precipitation over the basin at time t , HS_i the measured snow depth at the given grid point i , and HS_{avg} is the mean ADS snow depth

Chapter 2. Influence of Slope-Scale Snowmelt on Catchment Response Simulated With the *Alpine3D* Model

over the catchment. Note that we could not run the snow transport module of *Alpine3D*, which is computationally too demanding for the size of the area but would significantly increase the heterogeneity of snow (Mott and Lehning [2010]).

- For the incoming shortwave radiation (ISWR), the atmospheric attenuation coefficient and direct/diffuse radiation apportionments are computed for each station separately as a function of the local potential maximum solar radiation. These values are then interpolated over the grid using inverse distance weighting (IDW) and taking into account topographic shading.
- All other meteorological variables are interpolated applying IDW and an altitude-dependent lapse rate (Bavay and Egger [2014]).

Liquid water transport in the snow cover and in the soil layer is simulated either by a simple bucket approach or using the Richards equation (RE; Wever et al. [2014]). In the first approach, the liquid water content of a layer is constrained by an upper threshold; once this water holding capacity is exceeded, water is drained down to the next layer. The water holding capacity is a direct function of the volumetric ice/soil content (Wever et al. [2014]). The second method relies on the Richards equation originally developed for water movement in unsaturated soils and recently implemented for the vertical water movement in snow by Wever et al. [2014]. This implementation relies on the Van Genuchten [1980] water retention model and the parameterization proposed by Yamaguchi et al. [2012].

For comparison *Alpine3D* is run in four different configurations:

- Reference + Bucket scheme (Ref-BK): Precipitation is interpolated based on measurements from the Davos station plus a fractional lapse rate of 2%/100 m. Liquid water transport in the snowpack is simulated following the bucket approach.
- Scaling + Bucket scheme (Scal-BK): Precipitation is scaled following the method of Vögeli et al. [2016] as described above. Liquid water transport in the snowpack is based on the bucket approach.
- Reference + Richards equation (Ref-RE): Precipitation is interpolated based on measurements from the Davos station plus an altitudinal gradient of 2%/100 m. Liquid water transport in the snowpack is simulated using the Richards equation.
- Scaling + Richards equation (Scal-RE): Precipitation is scaled following the method of Vögeli et al. [2016]. Liquid water transport in the snowpack is simulated using the Richards equation.

2.4.2 *StreamFlow* setup

StreamFlow (Gallice et al. [2016]) is the hydrological extension of *Alpine3D*. This spatially explicit model relies on the travel time distribution (Botter et al. [2010], Comola et al. [2015a]) of water particles in a subcatchment. For each subcatchment, the mass balance is described by

two superimposed linear reservoirs mimicking the fast and slow subsurface runoff, respectively. The lower bucket is supplied by the soil runoff originating from *Alpine3D* up to a maximum recharge rate R_{max} (m s^{-1}) while the upper reservoir collects the excess water. The runoff generation itself is controlled by the mean travel time $\tau_{res,u}$ and $\tau_{res,l}$ (s) of water particles in each reservoir. The subwatershed runoff is then injected into the stream network and routed to the outlet. Using the TauDEM algorithm (Tarboton [1997]), the Dischma basin was divided into 55 subwatersheds with a mean area of 0.79 km^2 and its stream network was delineated (Figure 2.1b). For the calibration, we opted for a Monte-Carlo approach and chose the best parameter values for R_{max} , $\tau_{res,u}$ and $\tau_{res,l}$ by optimizing the Nash-Sutcliffe model efficiency (NSE) coefficient (Nash and Sutcliffe [1970]) independently for each of the four model configurations. With this individual calibration, the differences in model results highlight the influence of water input on the hydrological response and we avoid biases induced by suboptimal parameter sets. The calibration is carried out on measured discharge at the Dischma basin outlet only. Observations from the subbasins are used for validation purposes. The streamflow seasonality is evaluated through the centroid in time (CT) of the daily discharge proposed by Stewart et al. [2005]. Finally, the results presented below are the average of the 100 best simulations for each model configuration in order to have a more robust signal.

2.5 Results

2.5.1 Snow Depths at Peak Accumulation

In high-altitude alpine catchments, snow cover at peak accumulation can be considered as the initial condition of the system for the spring melting season. The results of the reference simulation (Ref-BK) fail to reproduce the observed snow depth distribution patterns (Figure 2.3a, $R^2 = 0.34$) with most of the modeled values between 1 and 2 m. Shallow snow depths are largely overestimated, especially on south-facing slopes (green range in the color scale in Figure 2.3a), while the deeper snow depths are largely underestimated. Simulated snow depths barely reach values larger than 2 m, whereas observations can reach up to 3.5-4 m. The scaling approach (Scal-BK) brings the distribution of modeled snow depths much closer to the observed values (Figure 2.3b). The range is also wider with values between 0 and 4 m, and the scatter around the 1:1 line is significantly reduced ($R^2 = 0.96$). The root-mean-squared error is only 0.27 m compared to 0.62 m for the Ref-BK simulation. The scaling method shows a small positive bias (mean absolute error [MAE] = 0.25 m) for values between 0.5 and 4 m. During this period, a strong settling or compaction of the snowpack was observed over the entire basin, which could partially explain these differences (supporting information Figure A.1, see also extensive discussion in Vögeli et al. [2016]). On the other hand, the Scal-BK simulation results slightly underestimate snow depth values below 0.5 m (MAE = 0.12 m). The ADS snow depths were obtained around peak accumulation, but some low-elevation parts or south-facing slopes of the basin had already experienced limited melt. *Alpine3D* assimilates the data set, inherently containing this bias, but the model computes the melting and settling processes again. This leads to an overestimation of these two phenomena (i.e., melt and settling) and consequently

Chapter 2. Influence of Slope-Scale Snowmelt on Catchment Response Simulated With the *Alpine3D* Model

leads to an underestimation of the snow thickness (especially at lower elevations). These results are similar to the findings of Vögeli et al. [2016] for the winters of 2011/2012, 2012/2013, and 2013/2014.

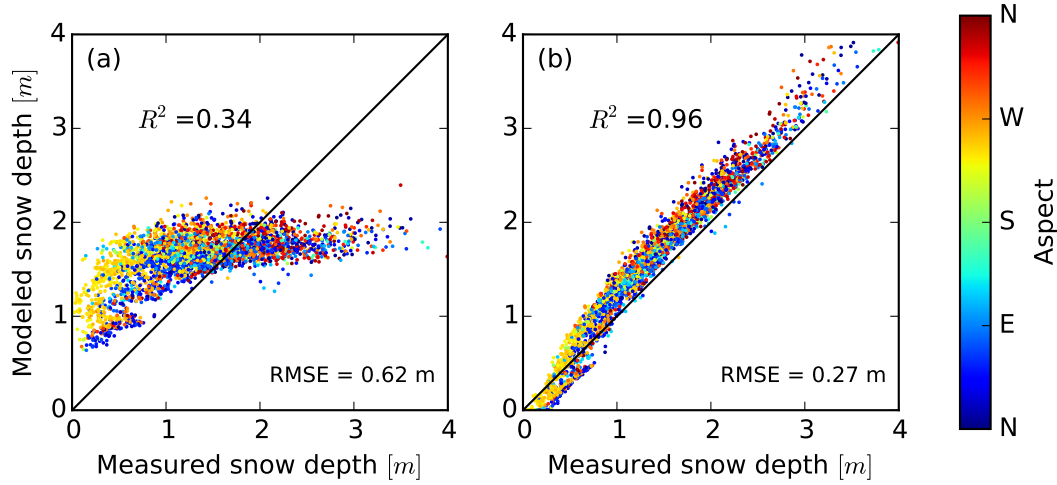


Figure 2.3 – Modeled versus measured (ADS) snow depths over the Dischma River basin on 15 April 2015 (around peak accumulation). (a) Reference simulation (Ref-BK) and (b) the scaling method (Scal-BK). Color indicates the aspect of each grid cell.

The peak accumulation snow variability is also a good indicator of which part of the natural processes the model is able to reproduce. As expected, the scaling approach is performing much better (snow depth coefficient of variation (CV) = 0.46-0.48 compared to 0.5 for the ADS data) than the reference scheme (CV = 0.20-0.21). More interestingly, the original ADS data at 2 m resolution have a CV of 0.7, which is likely still smaller than the true spatial variability of the snowpack. At the chosen resolution, the snow variability in the model is significantly filtered out. Detailed statistics are presented in supporting information Table A.1.

2.5.2 Site-Scale Comparison of Snow Accumulation and Melt

The temporal snowpack evolution at Rinertaelli (SE facing) and Stillberg (NE facing) highlights the deficiency of the reference precipitation interpolation scheme for reproducing the snowpack spatial heterogeneity (Figure 2.4 and supporting information Figure A.1 for a comparison with measurements). Even though the two sites have opposite aspects, their evolution throughout the winter is relatively similar, which should not be the case (due to melt events at the beginning of the winter and the local energy balance leading to enhanced settling at southerly expositions). At the end of the accumulation season, the difference in snow water equivalent (SWE) is only about 10%. During the ablation period, the heterogeneity of melt patterns between the two sites (as a consequence of differences in the local energy balance) seems well captured by *Alpine3D* with a much faster disappearance of snow on the south-facing slope (20 days earlier).

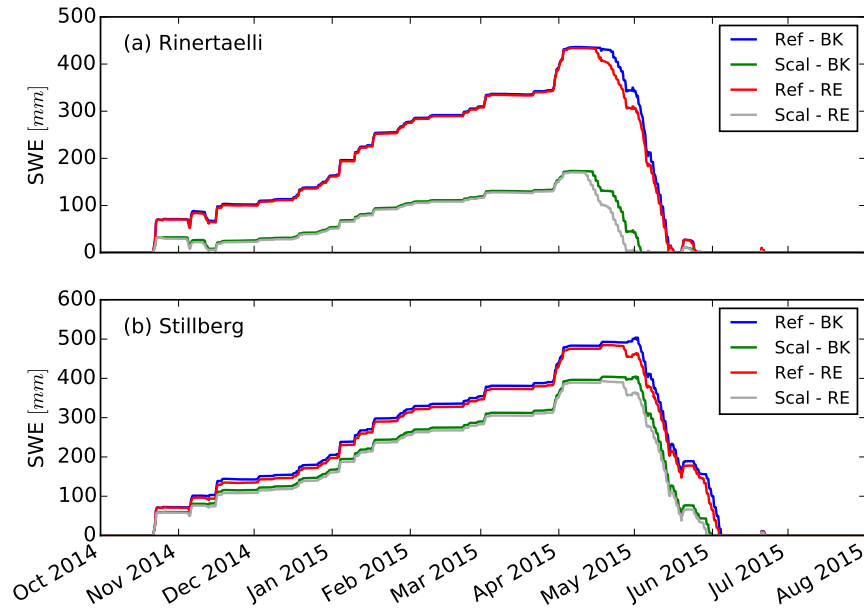


Figure 2.4 – Comparison of modeled SWE at (a) the Rinertaelli and (b) the Stillberg sites for the four configurations: (1) reference interpolation and bucket scheme (Ref-BK), (2) scaling method and bucket scheme (Scal-BK), (3) reference interpolation and Richards equation (Ref-RE), and (4) scaling method and Richards equation (Scal-RE).

At Rinertaelli, the precipitation scaling sharply reduces snow accumulation, reaching only 40% SWE at the maximum compared to the reference simulation, and is much closer to observations (45 cm in the ADS data set versus 40 cm in the model, supporting information Figure A.1). Shallower snowpacks require less energy to reach isothermal conditions, and melting starts 3-4 days earlier (14 April versus 17 April with the BK scheme and 11 April versus 15 April with RE scheme). The combination of these two factors results in a shorter snow cover duration and the site becomes snow free 11-12 days earlier than in the reference simulation depending on the liquid water transport scheme.

At the Stillberg site, the impact of the precipitation scaling method is smaller. At peak accumulation (20 April 2015), SWE is only 18% lower than in the reference simulation. Compared to Rinertaelli, this difference is not large enough to notably change the thermal state of the snowpack (not shown) but still reduces the snow duration by 4 days. When validating the model output with the snow depth measured at the Stillberg meteorological station (located 500 m away from our site, and at similar elevation), the scaling approach leads to improved results in snowpack evolution, melt dynamics and snow disappearance date (supporting information Figure A.1). The above two examples show how increased snow depth variability results in larger spatial heterogeneity in melt dynamics, and in consequence, in meltout dates.

When using the Richards equation, melt water is routed faster through the snowpack that becomes isothermal earlier (not shown). Thus, liquid water is released at the base of the snowpack a few days earlier than for the bucket scheme. This effect is visible at both sites, although the difference in water release between the two schemes is more pronounced at the

Chapter 2. Influence of Slope-Scale Snowmelt on Catchment Response Simulated With the *Alpine3D* Model

shallower Rinertaelli site (Figure 2.4a). These observations are in agreement with the results of Wever et al. [2015], who found a change of the snow internal energy budget with the Richards equation.

The two lysimeters enable an original comparison of snowpack liquid water output at the site scale with model output. On the southeast-facing slope (Figure 2.5a), the shallow snowpack produces rapid outflow following mid-April. The scaling approach combined with the Richards equation performs really well with respect to timing: the melt season starts on 11 April, 1 day earlier compared to the observations. The reproduction of daily cycles is satisfactory (Table 2.2, $NSE_{Scal-RE} = 0.234$), although the intensities are underestimated (Figure 2.6a). Simulated snowpack runoff increases rapidly in the morning and reaches a maximum in the early afternoon, slightly delayed compared to measurements. The subsequent recession limb approaches zero around midnight. Observed outflow never entirely reaches 0. When classic interpolation is used in combination with the Richards equation, the runoff peak is delayed due to longer travel times through the deeper snowpack while dynamics remain similar ($NSE_{Ref-RE} = -1.356$). The signal resulting from the bucket scheme is less accurate: timing and magnitude are satisfactory but the threshold effect prevents accurate reproduction of the recession curve ($NSE_{Ref-BK} = -1.67$, $NSE_{Scal-BK} = -0.05$). Also this observation is consistent with the results from Wever et al. [2014], who showed that the RE scheme clearly outperforms the bucket scheme at subdaily time scales. When looking at the slopes of cumulative runoff for the Rinertaelli site (Figure 2.5a), no simulation is able to reproduce the observed output rates leading to an noticeable discrepancy at the end of the melt season. In terms of mass balance, the reference interpolation scheme overestimates the cumulative outflow by about a factor of 2 while the scaling approach is much closer to the observations (30% underestimation). These results corroborate the negative bias noticed above for shallow snowpack at peak accumulation.

At the Stillberg site (NE facing), melt dynamics are different than at Rinertaelli (Figure 2.5a versus Figure 2.5b). Snowmelt starts on 18 April, 6 days later than at Rinertaelli, and produces very limited outflow during the first 3 days. The deeper snowpack holds a nonnegligible part of the liquid water in the snow matrix during that period. Starting on 21 April, runoff slightly increases. None of the model configurations is able to reproduce the onset of the melt season perfectly; however, simulations using the Richards equation are closer to the observed onset and produce larger melt rates than with the bucket scheme. Snowmelt sharply increases at the beginning of May when the snowpack at Rinertaelli has already disappeared. The daily cycle, notably the timing, is very well captured in the model configurations using the Richards equation (Figure 2.6b, $NSE_{Ref-BK} = 0.593$). These simulations reproduce the recession curve very well and even sustain an outflow during nighttime. Contrary to the south-facing site, the maximum intensities are slightly larger than observed. The scaling approach compensates for the total volume error by slightly reducing the total precipitation. Discrepancies between the observed and modeled cumulative runoff are very minor (Figure 2.5b) indicating correct representation of melt dynamics. Note that ISWR and ILWR are measured at the Stillberg weather station and both are used in the modeling calculations. Thus, interpolation errors for

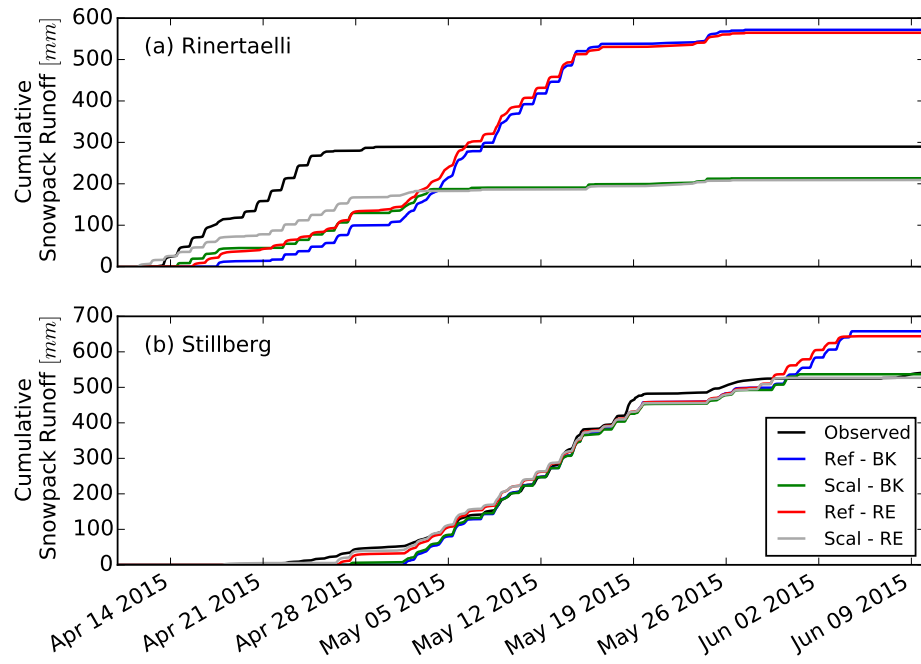


Figure 2.5 – Cumulative liquid water output at the base of the snowpack at (a) Rinertaelli and (b) Stillberg for the four model configurations.

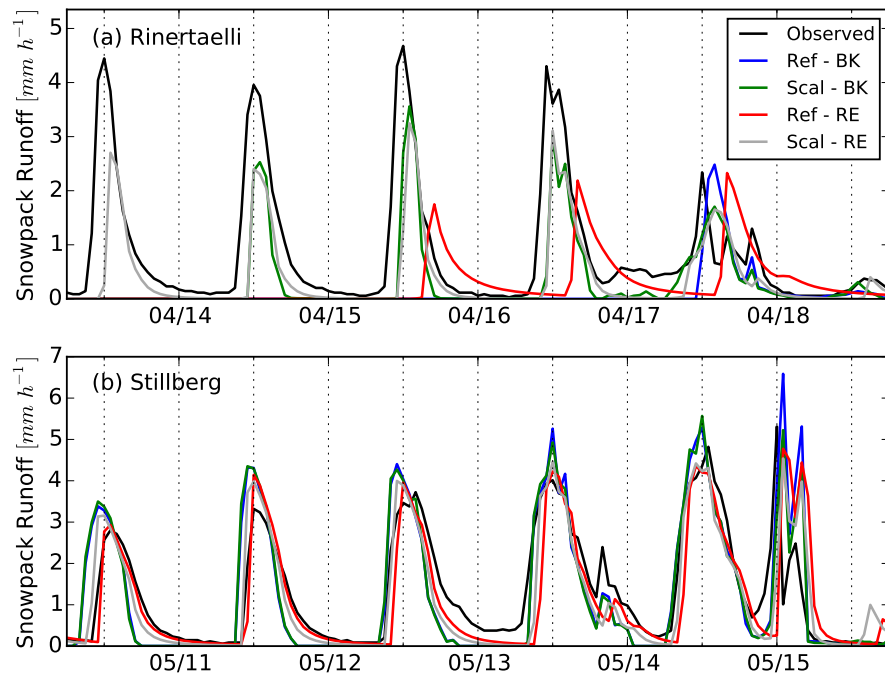


Figure 2.6 – Comparison of observed and simulated liquid water output at the base of the snowpack in (a) Rinertaelli and (b) Stillberg for the four model configurations.

Chapter 2. Influence of Slope-Scale Snowmelt on Catchment Response Simulated With the *Alpine3D* Model

these quantities are small due to the vicinity of the station to the snow site.

Table 2.2 – Nash-Sutcliffe Efficiency Coefficient (NSE) and Coefficient of Determination (R²) of the Liquid Water Output and Its Cumulative Value in Rinertaelli and Stillberg for the Four Different Model Configurations.

		Liquid output		Cumulative liquid output	
		NSE	R ²	NSE	R ²
Rinertaelli	Ref-BK	-1.67	0.00	-1.96	0.56
	Scal-BK	-0.05	0.10	0.32	0.85
	Ref-RE	-1.36	0.00	-1.69	0.61
	Scal-RE	0.23	0.25	0.45	0.95
Stillberg	Ref-BK	-0.14	0.40	0.95	0.97
	Scal-BK	0.36	0.55	0.99	0.99
	Ref-RE	0.16	0.44	0.96	0.98
	Scal-RE	0.59	0.66	0.99	0.99

The combination of the Richards equation and the scaling approaches results in improved performances in term of NSE coefficient and coefficient of determination (Table 2.2). Moreover, model results are much more accurate at Stillberg versus Rinertaelli, which can be partially explained by the proximity of the AWS station to the Stillberg site. These statistics also show that the precipitation interpolation method has a higher impact on model performance than the liquid water transport scheme.

2.5.3 Snowmelt Dynamics at the Basin Scale

At the basin scale, melt dynamics also change considerably for the different model configurations: this is illustrated by the temporal evolution of total SWE and the snow depletion curves (SDC) over the Dischma basin (Figure 2.7). From mid-April to mid-May, the RE scheme generates slightly more liquid water output from the snowpack compared to the bucket scheme (Figure 2.7a). Afterward, the influence of the snow distribution becomes predominant: with increased snow heterogeneity, parts of the basin become snow free earlier, evident by the earlier decrease in snow-covered area (SCA) in the simulations using the scaling approach (Figure 2.7b). However, the scaling also leads to slower melt, and thus to larger SWE volumes and higher SCA values than in the reference case during the second half of the melting season. In late June, the difference between the two interpolation methods reaches up to 10% in SCA and more than $2.7 \times 10^6 \text{ m}^3$ of SWE, doubling the remaining snow volume. The same dynamics are observed for the headwater catchment (not shown) with a difference in SCA of 20% and three times more SWE in early July.

The spatial patterns of snow distribution at peak accumulation obtained using the classic precipitation interpolation scheme (Figure 2.8a) show little heterogeneity (mean snow depth $HS_{Ref-BK} = 1.56 \text{ m}$, standard deviation $\sigma_{Ref-BK} = 0.32 \text{ m}$, compared to $HS_{obs} = 1.42 \text{ m}$, $\sigma_{obs} = 0.71 \text{ m}$). This spatial homogeneity is highlighted by the basin-wide histograms of

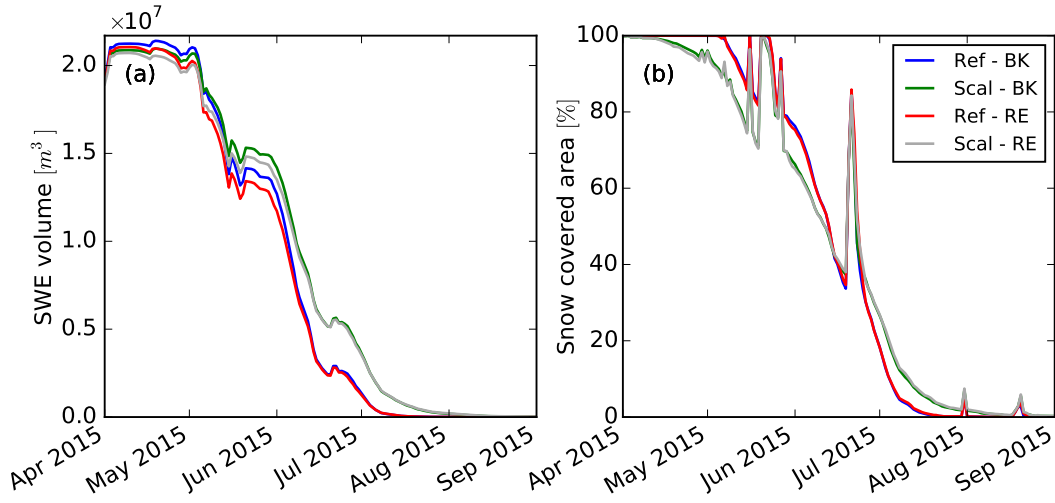


Figure 2.7 – a) Total SWE volume and (b) snow depletion curve (SDC) of the Dischma basin for the four model configurations. The spikes in the SDC correspond to snowfall events.

snow depth at peak accumulation (supporting information Figure A.2). Modeled variability for the reference scheme is principally controlled by the precipitation elevational gradient (supporting information Figure A.3). The repeated melt events and rain-on-snow events that took place between October 2014 and January 2015 had little effect on the resulting snow heterogeneity and above statistics at peak accumulation (15 April 2017). Similarly, aspect variations across the basin did not play a dominant role in the resulting snow distribution during the accumulation season (supporting information Figure A.4). Once the onset of spring melt sets in, a small increase in variability is observed ($\sigma_{Ref-BK} = 0.4$ m, supporting information Figure A.2) as a result of the spatial variability of radiative fluxes induced by topography. Nevertheless, the initial snowpack heterogeneity is still the dominant control on the general dynamics of melt (supporting information Figure A.2). This homogeneity is also clearly visible spatially: the symmetry is noticeable between the two main valley flanks (Figure 2.8b) while one would expect earlier snow melt on the southwest-facing slope. Finally, this uniformity leads to a shortening of the melting season because deeper accumulation areas are scarce (supporting information Figure A.2).

With the scaling interpolation scheme, the heterogeneity of snow distribution (Figure 2.8 and supporting information Figure A.2) throughout the melting season is enhanced since it includes effects of snow transport and early melt. The snow distribution at the onset of melt also agrees very well with the observations ($HS_{Scal-BK} = 1.55$ m, $\sigma_{Scal-BK} = 0.72$ m versus $HS_{obs} = 1.42$ m, $\sigma_{obs} = 0.71$ m). Snow accumulation as a function of elevation also differs significantly between the two precipitation interpolation methods, with lower accumulation below 2,300-2,400 m and a maximum between 2,500 and 2,600 m for the scaling interpolation scheme (supporting information Figure A.3). There is a decrease in snow accumulation on southwest-facing slopes and an increase on all north-facing slopes (from northwest to northeast) with the scaling interpolation method (supporting information Figure A.4). As observed at the site scale, the southeast-facing slopes of the Rinertaelli side-valley have a

Chapter 2. Influence of Slope-Scale Snowmelt on Catchment Response Simulated With the *Alpine3D* Model

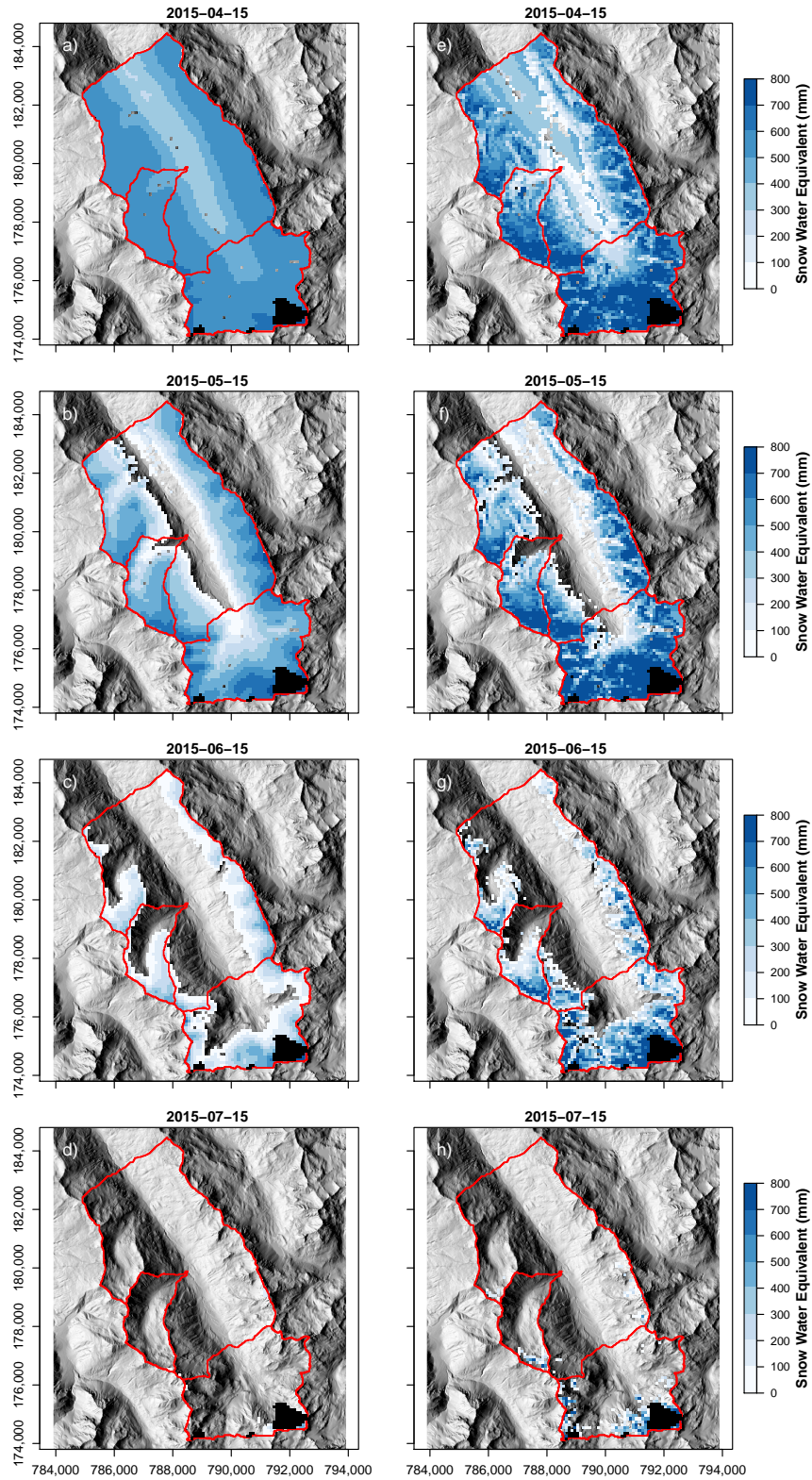


Figure 2.8 – Comparison of the snow water equivalent (SWE) during the melting season for (a-d) the Ref-BK simulation and (e-h) the Scal-BK. The glacier is masked in black.

noticeably shallower snow accumulation. As the melt dynamics are strongly determined by the initial snowpack distribution, these features persist throughout the melt season (Figure 2.8 and supporting information Figure A.2). Later, during the second half of the melt season, deeper snow accumulations remain on slopes close to ridges, while in the reference case, only shallow snow is present in these areas (compare maps c and g, d and h in Figure 2.8).

In the following paragraphs, we compare measured discharge at the outlet of two subbasins and the entire basin to cumulative soil runoff close to the surface (at 5 cm depth) integrated over each contributing area (Figure 2.9). This allows for a comparison between observations and modeling results without calibration. For the Rinertaelli subbasin, the total mass balance is almost independent of the chosen interpolation scheme but the snowpack distribution changes (Figure 2.9a and supporting information Figure A.2). The heterogeneous snowpack leads to more melt water at the very beginning of the melt season, while later the reference configuration produces more runoff because the shallower snowpack portions in the scaling simulations have already disappeared and the remaining contributing area is smaller. On the other hand, the snowmelt season lasts longer due to deeper accumulations generated by the scaling approach. The water transport scheme changes the response only marginally due to averaging effects at the basin scale. Compared to the observed discharge, which starts earlier and has a larger magnitude, melt in April is consequently somewhat underestimated. This is coherent with the site-observations from the Rinertaelli, where the model underestimates the observed melt rate on south-facing slopes. In addition, the negative bias observed for shallow snow (0-0.5 m; Figure 2.3 and supporting information Figure A.2) could also partly explain this underestimation.

In the Duerrboden catchment (Figure 2.9b), the influence of the snowpack spatial distribution on the soil runoff is even more evident than in the previous case since the mass balance is not conserved locally at the subbasin scale as the reference interpolation largely underestimates snow accumulations on the upper part of the basin (supporting information Figure A.2). At the end of June, the simulations are diverging with snowmelt runoff remaining considerably lower in the reference simulations. Relative to the observations, this underestimation is clear; the soil runoff cannot sustain the measured runoff. Physically this would be possible if significant groundwater storage volume was available, however this is not the case in the upper Dischma basin.

By definition, the scaling method conserves mass over the entire Dischma catchment (Figure 2.9c). The results for the whole basin are partly similar to the ones observed previously, i.e., the hydrological response is mainly driven by the snow distribution (in contrast to the liquid water transport scheme). The scaling method slightly changes the beginning of the melt season (by 2-3 days) but most importantly extends its duration by more than a month. Compared to observations, the start of the melt season is heavily delayed (by more than 15 days). This last feature has already been observed when using *Alpine3D* for snow simulations of alpine catchments (e.g., Gallice et al. [2016], Lehning et al. [2006]).

Chapter 2. Influence of Slope-Scale Snowmelt on Catchment Response Simulated With the *Alpine3D* Model

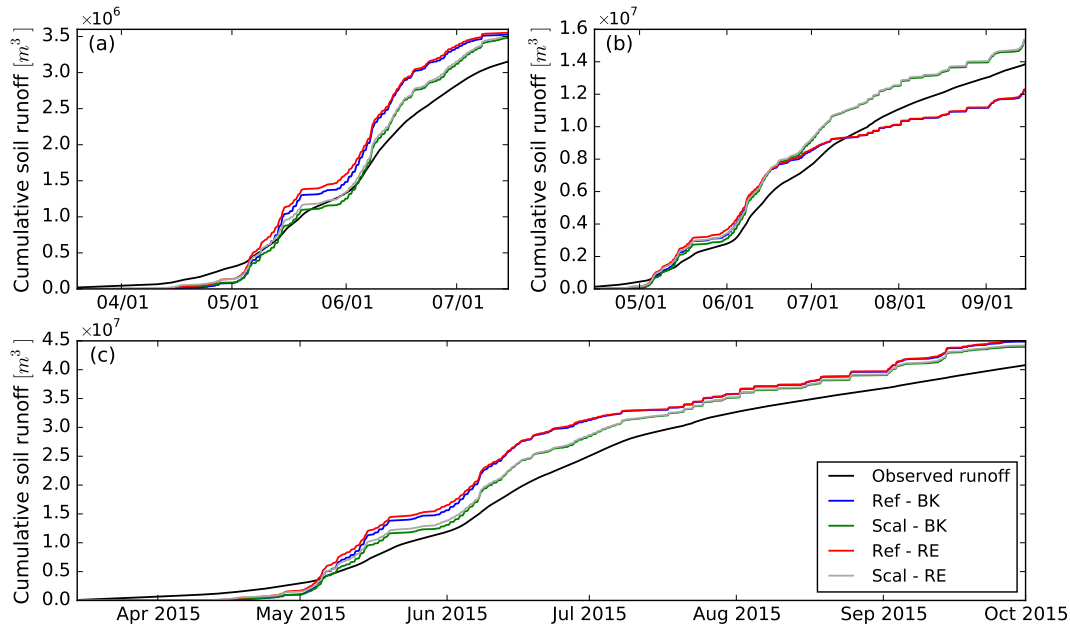


Figure 2.9 – Comparison of cumulative soil infiltration runoff (at 5 cm depth) for the different model configurations and the observed discharge for (a) the Rinertaelli subbasin, (b) the Duerrboden subbasin, and (c) the entire Dischma basin.

2.5.4 Hydrological Response

In the Rinertaelli basin, the general runoff pattern is fairly well represented by all configurations (Figure 2.10a) and model performances expressed as NSE coefficient are very similar (Table 2.3). However, some interesting features can be pointed out. First, the model fails to capture the timing of the onset of the melt season, with the first melt pulse occurring 30 days later than in the observations resulting in a strong underestimation of the discharge during that time. In May and June, the general streamflow dynamics are well captured but the magnitude is underestimated. On the contrary, from end of June, the discharge is overestimated in the four scenarios, which could be a direct consequence of the previously observed runoff underestimation (from April to June). Even if these results are consistent with the ones at the site scale (underestimated melt intensities on south-facing slope, section 2.5.2) and subbasin scale (delayed onset of the melt season, section 2.5.3), the underestimation at the beginning of the snowmelt season at the subbasin scale is fairly large.

In the Duerrboden catchment, a more realistic snowpack significantly improves the hydrological simulation (NSE of 0.86 and 0.85 compared to 0.72 and 0.74, Table 2.3) mainly by correctly simulating the snowmelt season, which is longer by more than a month (see the change of the centroid in time [CT], a seasonality indicator (Stewart et al. [2005]), in Table 2.3 and Figure 2.10b). In the reference configuration, the basin becomes snow free too early in the season, which results in a strong underestimation of the observed discharge from early July to October explaining the bad performance in terms of log NSE (Table 2.3). As already discussed for the soil runoff, differences between the two liquid water transport schemes are very small. Finally,

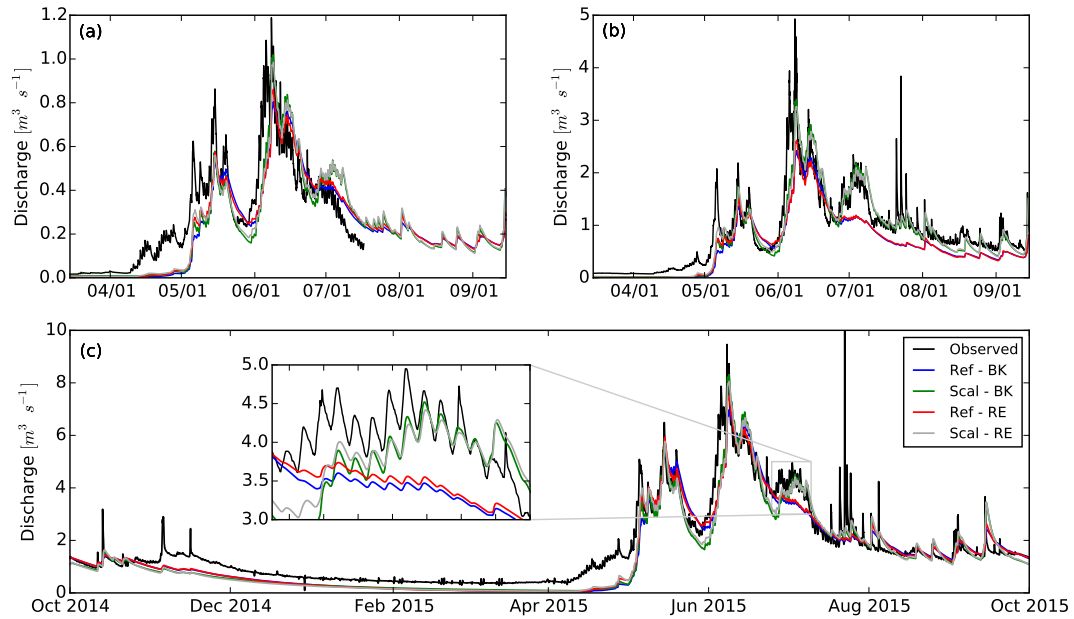


Figure 2.10 – Observed and modeled discharge for (a) the Rinertaelli subbasin, (b) the Duerrboden subbasin, and (c) the entire Dischma basin. Note the different discharge scales between the three panels.

the discharge underestimation in late April and May is visible in all simulations. This appears to be a model error possibly from the meteorological interpolation or from misrepresentation of subgrid processes, which is further addressed below in section 2.6.

Table 2.3 – Performances of the Hydrological Model for the Three Monitored Basins in Terms of Nash-Sutcliffe Efficiency (NSE), log NSE Based on the Logarithmic Discharge Values and the Centroid in Time (CT) of the Daily Discharge (in Days Since 1 October).

		NSE	log NSE	CT (days)
Rinertaelli basin	Ref-BK	0.78	0.32	239.1
	Scal-BK	0.79	0.61	241.4
	Ref-RE	0.81	0.44	239.4
	Scal-RE	0.79	0.61	243.1
Duerrboden basin	Ref-BK	0.72	-0.97	244.4
	Scal-BK	0.86	0.27	248.0
	Ref-RE	0.74	-0.75	244.1
	Scal-RE	0.85	0.02	249.6
Dischma basin	Ref-BK	0.85	-0.38	235.2
	Scal-BK	0.86	0.05	237.8
	Ref-RE	0.87	-0.28	235.1
	Scal-RE	0.86	-0.13	239.2

At the Dischma outlet, model performance is high for all configurations with NSE coefficients between 0.85 and 0.87 (Table 2.3). Even though the basin size causes a noticeable smoothing of the discharge signal (Figure 2.10c), interesting lessons can be learned. An initial snowpack

Chapter 2. Influence of Slope-Scale Snowmelt on Catchment Response Simulated With the *Alpine3D* Model

closer to observations improves the simulated discharge evolution, notably during the second half of the melt season when large snow accumulations sustain the discharge (see inset in Figure 2.10c and change in CT in Table 2.3). With the reference interpolation, the hydrological model compensates the lack of snow (in July and August) by an increase of the maximum recharge rate R_{max} . This leads to an intensive use of the lower reservoir, which has a longer residence time than the upper one and thus, the large bias observed in the headwater catchment is not visible anymore. This is one of the main drawbacks of model calibration: it will hide model underperformance by compensating through other mechanisms.

2.6 Discussion

The present study highlights the importance of having different types of observational data when trying to understand snowmelt variability in a small alpine catchment. These data allow for a detailed and independent validation of different components in physically based and spatially distributed snow models such as *Alpine3D*, highlighting strengths and weaknesses of such type of models. At the same time, it is essential that observations also cover various spatial scales. Our results show how discharge data at subbasin scales highlight features that would have been missed with only one streamflow time series at the basin outlet (i.e., snowmelt sustaining the discharge in summer). This is because the discharge signals of the various subbasins are averaged out over aggregated scales. Finally, novel snow surveying techniques allow for improvements in snow modeling that were previously unavailable. Here we show how the assimilation of a distributed snow depth data set at resolutions of the order of 100 m for precipitation interpolation and validation of model results allows a better understanding of the hydrological system itself. Such assimilation also allows the identification of model deficiencies that are difficult to assess with traditional snow surveying techniques (e.g., manual snow depth surveys).

SNOWPACK was originally developed to model the one-dimensional snowpack evolution at the location of an *IMIS* weather station (Lehning et al. [1999]). Consequently, good model performance at the site scale is not a surprise. However, the spatial interpolation of meteorological variables in complex terrain remains challenging and spatially distributed simulations are thus not trivial. The method of Vögeli et al. [2016] partially reduces the precipitation interpolation error. This change of the local mass balance translates in a change of the energy balance by reducing or increasing the thermal inertia of the snowpack (proportional to its mass). Moreover, the insulating effect of the snow and the presence (or absence) of a high albedo surface significantly modify the local energy budget. The combination of mass redistribution with the correct local components of the energy balance improves the results considerably (for example $NSE = 0.23$ versus $NSE = -1.36$ in Rinertaelli). As for the liquid water transport, the gains in term of performance are less significant between the two schemes, i.e., the bucket and Richards equation methods. However, the Richards equation approach leads to improvements in the representation of the snowmelt output dynamics at the base of the snowpack when compared to hourly observations at the point scale, confirming earlier studies at extensively instrumented sites (Wever et al. [2015, 2014]). The present study had

to rely on interpolated meteorological data only. At the Rinertaelli site, the beginning of the melt period and its diurnal cycle are well captured. Modeled liquid output intensities are nevertheless lower than observed. Given that the second lysimeter (located close to a AWS) is very well simulated ($NSE = 0.59$), we would suspect an error of shortwave and/or longwave radiation interpolation or that the interpolation scheme misses local temperature and wind maxima induced by micrometeorological phenomenon. Even if we cannot completely exclude a measurement error of the lysimeter, the large discharge underestimation observed in the Rinertaelli subbasin is therefore not fully explained. Unfortunately, we have no meteorological observation to validate our hypothesis.

As shown by Anderton et al. [2004], seasonal snowmelt dynamics at subcatchment scales are mainly driven by the snowpack distribution at the peak of accumulation. Then the challenge is to get a realistic snowpack distribution as an initial stage variable for snowmelt modeling, even in a well-instrumented area. As observed here and in several previous studies (Jonas et al. [2009], Sevruk [1997], Grünwald et al. [2014], Grünwald and Lehning [2011]), precipitation and SWE exhibit a positive trend with elevation. However, considering only a linear altitudinal gradient leads to a too simplistic snow distribution. In reality, several processes such as preferential deposition, snow transport by winds, and avalanching lead to larger heterogeneity (Clark et al. [2011]). In this study, we applied the approach by Vögeli et al. [2016] for precipitation interpolation and mass accumulation. It has the merit of being computationally efficient and provides an initial snowpack distribution closer to the observations. The methodology also implicitly corrects for some of the processes mentioned above that are difficult to model explicitly, e.g., precipitation preferential deposition, snow transport, and avalanching. However, this approach requires a meticulous analysis of the ADS snow distribution to identify potential biases (e.g., heterogeneous snowmelt before date of flight) that could be introduced directly into the model results. In our case, due to the relatively large elevation gradient in the basin, the data set has a small negative bias for shallow snow and low elevations due to limited melt. This could be a second partial explanation of the underestimation observed in the discharge time series at the beginning of the melt season. Finally, the scaling method implicitly assumes that peak snow accumulation occurs simultaneously over the entire basin. Even if this classic categorization into an accumulation and an ablation season is convenient, this assumption is mainly but not fully fulfilled in our high-alpine case study. This condition is certainly not valid in regions with larger elevation and climatic gradients and, in general, will be less and less the case due to climate change in higher elevations. Thus, the scaling method must be applied cautiously. In a warmer climate, the significance of spatial snow variability for mountain hydrology will be fundamental, notably in terms of timing. As shown in our results, large snow accumulations are strongly underestimated by a traditional interpolation scheme. This snow storage is essential to extend the duration of the melt season and sustain the observed discharge in summer. These considerations tend toward the development of more physical/dynamic methods to model the spatial variability of snow.

We intentionally chose the StreamFlow model because of its limited number of parameters, as the objective was to study the influence of snowpack differences rather than the calibration

Chapter 2. Influence of Slope-Scale Snowmelt on Catchment Response Simulated With the *Alpine3D* Model

capacity of the model. Unfortunately, the calibrated hydrological model acts as a low-pass filter on input signals and smoothens a large portion of the differences. However, we showed that the vertical snowpack liquid water transport scheme has a limited impact on the hydrological response at the catchment scale. Conversely, the snow distribution has a significant influence on the discharge at the subbasin scale (Table 2.3) and for the whole catchment (*getting the right answer for the right reasons*). With a more realistic snowpack distribution, the melt season starts earlier and lasts longer, more coherent with observations. These results are also in agreement with previous studies (Luce et al. [1998], Warscher et al. [2013], Winstral et al. [2013]) for which snow transport was considered. If we focus our attention on model performance (Table 2.3), differences are relatively small, which raises the question whether the increasing complexity is worth the small added value. In our opinion, simpler models can still be a good choice for many (operational) applications while physically based models would be more appropriate when trying to understand detailed snow and hydrological processes.

One of the results from our study is that the beginning of the melt season is not captured accurately whatever configuration of *Alpine3D* is chosen. The significance of the discrepancy indicates a misrepresentation or a missing process in the model. In reality, snow processes are taking place at varying spatial and temporal scales (Blöschl [1999]). In our case, the spatial resolution seems adequate to reproduce the large-scale features (regional and watershed scales). Nevertheless, we certainly miss some subgrid processes that take place at hillslope and local scales. For example, at the beginning of the melt season, the snowpack can be patchy due to the presence of boulders or rock faces exposed to the sun. Such situation can lead to an albedo feedback or modify the surrounding radiative budget enhancing melt. Recent work in the same region has also pointed out a strong feedback of the snow patch distribution on the local (katabatic/anabatic) wind and temperature fields (Mott et al. [2015]). At the beginning of the melt season (high SCA), these circulation processes lead to an increase of the sensible heat flux toward the snowpack and then an intensification of ablation processes. As diurnal mountain winds are thermally driven, they particularly take place on south-facing slopes, but cannot be modeled in the present version of *Alpine3D* as no lateral exchange between grid elements is considered or would require the coupling of an atmospheric model (e.g., *ARPS* or *WRF*). Once the ablation season started, the lateral meltwater transport at the snow/soil interface (Eiriksson et al. [2013]) and more generally the overland flow could also accelerate the hydrological response by bypassing the soil compartment. When the meltwater infiltrates into the soil, it displaces old water (known as translatory flow; DeWalle and Rango [2008]) and can rapidly generate runoff in the stream. All these elements support a proper integration of subgrid variability in snow models.

2.7 Conclusions

In this study, we analyze the effects of snow accumulation patterns and liquid water transport within the snowpack on snowmelt dynamics and on the hydrological response of an alpine catchment in the Swiss Alps. Our analyses combine in situ measurements of subhourly snowmelt output on north-facing and south-facing slopes, streamflow at the outlet of two

small tributaries and at the outlet of the entire catchment, distributed snow depths from airborne photogrammetry, and output from the *Alpine3D* spatially distributed snow model for the water year 2014-2015.

During the accumulation period, we show how a novel precipitation scaling approach for spatial interpolation leads to an improvement in the estimation of snow distribution at peak accumulation when compared to a more traditional interpolation method ($R^2 = 0.96$ versus $R^2 = 0.34$). The simulated spatial pattern of peak accumulation differs by only 0.27 m in terms of RMSE when compared to measured snow depths at the 100 m scale. These results highlight the relevance of precipitation interpolation schemes for accurate representation of peak snow accumulation and distribution even in a well-instrumented area. Furthermore, we show how accurate representation of snow distribution at peak accumulation is key for accurate representation of snowmelt processes and differential melt. Simulated results demonstrate that the increased heterogeneity of snow accumulation obtained using the scaling interpolation approach produces differential melt patterns with rapid melt from shallower snow accumulation areas, due to reduced thermal inertia and melt water travel time in the snowpack, compared to slower melt from areas of deeper snow located at high elevation. These differential patterns translate in faster runoff generation at the onset of the melting season from shallower snow packs and a prolonged snowmelt season duration because of the delayed melt from the deeper snow accumulation areas. Such differential melt patterns and runoff responses are severely muted when the more traditional precipitation interpolation method is used. Finally, we show that improvements in the representation of the spatial variability of snow lead to an improvement of the NSE by up to 0.12 for the simulated streamflow when compared to measurements at two different locations, within the basin and at the outlet.

Simulations using a Richards equation scheme allow for faster drainage of liquid water toward the base of the snowpack when compared to the standard bucket approach that was originally implemented in the SNOWPACK model. The effect of these improvements is reflected in a more realistic liquid water output from the snowpack in terms of timing and daily cycle at the site scale. At larger scales, the impact of the liquid water transport scheme is rather limited.

2.8 Acknowledgments

We thank Aurélien Gallice for his help in the field. ADS flights have been sponsored by Leica Geosystems. ADS flight processing has been done with the help of Yves Bühler and Mauro Marty. Part of the work and measurement infrastructure has been supported by the Swiss National Science Foundation project "Snow-atmosphere interactions driving snow accumulation and ablation in an Alpine catchment" (200021_150146). The models used here are available at <http://models.slf.ch/>. All results are available on the Envidat platform (www.envidat.ch) under <https://doi.org/10.16904/envidat.24>. Data from Meteoswiss (meteoswiss.admin.ch), IMIS network (www.slf.ch), swisstopo (swisstopo.admin.ch), and FOEN (hydrodaten.admin.ch) can be directly requested via the respective websites and are acknowledged.

3 Energy partitioning during the snowmelt season in a high Alpine catchment

3.1 Introduction

Snow cover modeling is important in different fields of research such as avalanche forecasting, cryospheric and climate sciences, snow hydrology or glaciology among others. This led to the development of numerous numerical models of different levels of complexity from very simple ones to much more detailed models (Etchevers et al. [2004], Essery et al. [2009]). Depending on the application, the variables of interest will also change: for example, snow metamorphism will be of great interest for avalanche prediction, whereas for snow hydrology, snow water equivalent or snowpack liquid runoff are more important. For snowmelt models, two main approaches exist: either a simple temperature-index model relying on the empirical relationship between snow ablation and air temperature (Hock [2003]). This method needs only few inputs (mainly air temperature), but requires a parameter calibration which limits its application in ungauged regions or under different conditions (i.e. climate change) and is not directly transferable from one region to another. On the other hand, physically based models apply the energy balance equation to obtain the potential snowmelt as a residual. This type of model requires more input data but no calibration. Their main drawback remains their large computational time, but this limitation becomes less and less important with the increase of available computational resources. Through continuous development during the last decades, physically based snow models have reached a high level of maturity for snow hydrology applications. Kumar et al. [2013] showed that they can even outperform calibrated temperature-index models for simulating river discharge.

Chapter 3. Energy partitioning during the snowmelt season in a high Alpine catchment

During the snowmelt season, the snow energy balance and its partitioning between the different components vary significantly depending on the climatic conditions. The net solar radiation and the sensible heat flux are the main energy sources for the melt whereas the net longwave radiation is a sink most of the time. Latent heat flux can become significant during specific events (i.e. rain on snow). However, their relative contribution is changing drastically from site to site (Ohmura [2001] and references therein). The different energy components can be measured at the point scale but are more difficult to apprehend at the catchment scale. In this case, physically based models are able to depict in a realistic way (despite not entirely exact) the processes taking place in mountainous basins. For example, the energy balance of mountain ranges situated in the rain-snow transition zone has been investigated (Mazurkiewicz et al. [2008], Kormos et al. [2014]) thanks to such models.

The present study focuses on the energy balance during the snowmelt season in a high Alpine catchment, the Dischma river basin. With the help of a spatially distributed and physically based model, *Alpine3D* (Lehning et al. [2006]), the goal is to identify the driving components of the ablation along with their relative significance over the entire basin. Moreover, the aim is to see how these components evolve at seasonal and inter-annual timescales. A secondary goal is to assess the robustness of the model chain *Alpine3D-StreamFlow* (Gallice et al. [2016]) over a relatively long time period (15 years) and see how the model is performing during the validation period.

3.2 Methods

3.2.1 Snow energy balance

The energy balance of the snowpack is determined by the different heat exchanges taking place at the snow surface and at the snow-ground interface. Mathematically, it can be expressed as:

$$\frac{\Delta Q}{dt} = SW_{net} + LW_{net} + SH + LH + G + M \quad (3.1)$$

where ΔQ is the total change in energy of the snowpack per unit area. The net shortwave radiation SW_{net} is the fraction of the solar radiation absorbed by the snow. The net longwave radiation LW_{net} is the difference between the thermal radiation emitted by the snowpack and the incoming longwave radiation from the surroundings (atmosphere, terrain). The atmospheric turbulent heat fluxes are partitioned between the sensible heat flux SH (representing the convective heat transfer) and the latent heat flux LH (energy linked to phase changes: evaporation, condensation or sublimation). G is the ground heat flux at the base of the snowpack and M is the heat advected through precipitation. When ΔQ is negative (net energy loss), the snowpack will cool down and if some liquid water is available, it will freeze. When the snowpack has a positive energy balance ($\Delta Q > 0$), it will first reach an isothermal state at 0°C over its entire thickness (partly through percolating melt water). Then, the excess energy will be used to produce snowpack runoff.

3.2.2 Model setup

The model setup used in the present study is very similar to the one described in the previous chapter (see Section 2.4 for a detailed description). We combine the physically based and spatially distributed snow model *Alpine3D* (Lehning et al. [2006]) with the spatially explicit hydrological model *StreamFlow* (Gallice et al. [2016]). We run the model on a regular grid covering the Dischma basin and its surroundings at a resolution of 100 m. To keep the computation time reasonable, we run *Alpine3D* with the bucket scheme for the snow and soil modules. As shown in the previous chapter, this choice influences only marginally, the hydrological response at the basin scale. The meteorological stations used as input are presented in Table 3.1. The *IMIS* network is operational since 1996 (Lehning et al. [1999]) but not all stations were installed from the beginning. Thus, we indicate, for each station, the data availability period in Table 3.1. For the precipitation, we use data from the *MeteoSwiss* station in Davos (corrected for precipitation undercatch, Goodison et al. [1997]) and apply an altitudinal gradient of 2% per 100 m based on regional analysis (see Section 2.2). Finally, we apply the precipitation correction method proposed by Vögeli et al. [2016] to get a more realistic spatial snow distribution. Snow depth data sets at peak accumulation were only available in 2010 and for the period between 2012 and 2016 (Bühler et al. [2015]). Consequently, we choose the snow depth map from 2012 and use it when no other data were available (2002-2009, 2011). As shown by Vögeli et al. [2016], such a procedure improves significantly the spatial distribution of the snowpack. It must be noted that the correction method only influences the spatial variability of the precipitation but not the mass balance (determined by the precipitation gauge measurement).

Table 3.1 – Automatic weather stations (AWS) used in the present study with their position (Easting/Northing in the Swiss Geodetic Datum CH1903), part of the *MeteoSwiss* (MCH) and *IMIS* networks. The time span during which the stations are available is indicated in the last column (water years).

Station name	Type	Position [m]	Altitude [m]	Availability period
Weissfluhjoch	MCH + IMIS	780'853 / 189'229	2540	2002-2016
Davos	MCH	783'514 / 187'457	1594	2002-2016
Davos - SLF	IMIS	783'800 / 187'400	1560	2002-2016
Stillberg	IMIS	785'455 / 183'136	2085	2002-2016
Puelschezza	IMIS	797'300 / 175'080	2680	2003-2016
Fluelapass	IMIS	791'600 / 180'975	2390	2004-2016
Baerentaelli	IMIS	782'100 / 174'760	2560	2002-2016

The *StreamFlow* model requires a three-parameter calibration. We use the discharge measured at the Dischma outlet by the Federal Office for the Environment (FOEN [2017]) as a benchmark. We arbitrarily choose a period of 5 years (water years: 2007-2011) and define it as the calibration timespan. We run a Monte-Carlo simulation with 10'000 realizations and choose the best parameter set based on the Nash-Sutcliffe model efficiency coefficient (NSE, Nash and Sutcliffe [1970]). The other water years are used for validating the model.

3.3 Results

3.3.1 Snow depth

Figure 3.1 compares the long-term snow depth measurement available in the Dischma valley with the output from *Alpine3D* at the specific grid cell. Overall, the agreement is good: the accumulation phase is well captured; the peak accumulation is very close to the maximum measured snow depth and the ablation phase follows the same dynamics as the observations. For the 2012 water year, the model is slightly overestimating the observed snow depth, but this is partly explained by the unusual snowy and windy conditions that led to an overestimation of the measured precipitation (see Wever et al. [2017] for more details). During the water years 2002 to 2010, the precipitation correction seems to work properly even if no specific snow data set was available for these years.

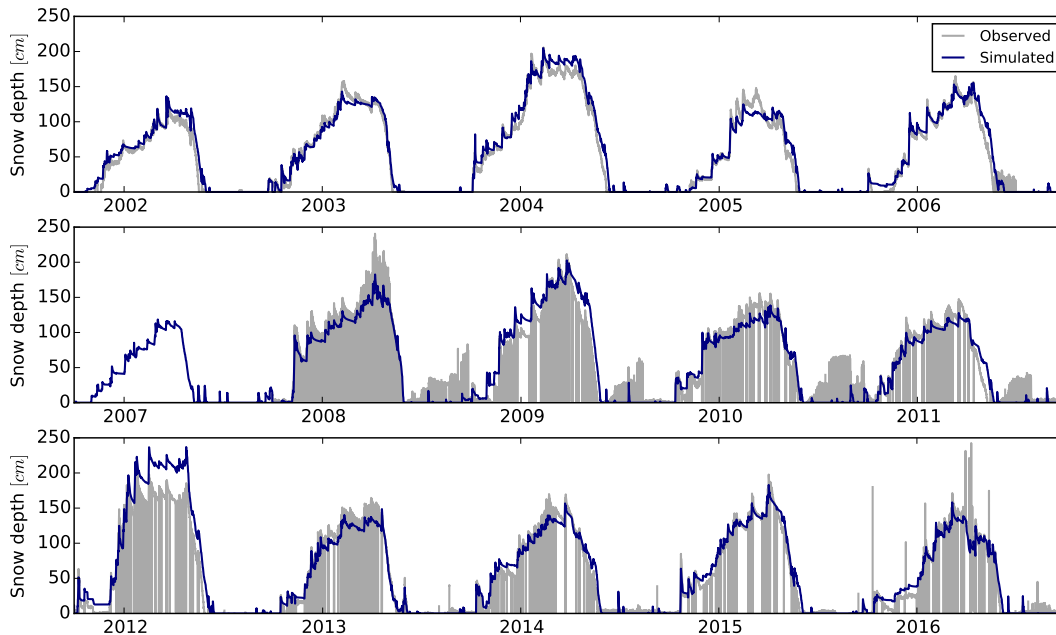


Figure 3.1 – Simulated and observed snow depth (vertical) at the Stillberg weather station over the period 2002-2016. Note that there is no observation during the winter 2006-2007. The outliers during the summer are mainly due to vegetation growing below the sensor.

The scatter plots comparing the measured and modeled snow depths are presented in Figure B.1 in the Appendix. Having a realistic snowpack at peak accumulation is essential to evaluate the energy balance during the snowmelt season. As shown in the previous chapter, the evolution of the snow cover is strongly dependent on the initial spatial snow distribution. The results for period 2012-2016 are very good: the point clouds are close to the 1:1 line and their spread is relatively small ($RMSE$: 0.22-0.36 m). In 2010, the snow depth map was of poor quality (personal communication, Y. Bühler, SLF), which can explain the lower agreement in Figure B.1a. For the years prior to 2010, we cannot assess the impact of the precipitation correction scheme on the spatial snow variability as no observations are available. However,

the principal goal is not to reproduce the "true" snowpack, but rather get a realistic snow depth distribution, which is the case when applying the method of Vögeli et al. [2016].

3.3.2 Hydrologic response

The discharge at the outlet of the Dischma basin is presented in Figure 3.2. The hydrological regime is typical of a high Alpine catchment with very low flows during the entire winter season because precipitation is stored as snow and ice. In March or April, the snow starts melting and generates high flow until the end of the summer. The model is capturing well this dynamics as well as the diurnal cycles. Conversely, the beginning of the melt season is almost systematically delayed and underestimated. This feature was already observed in the previous chapter and could be due to local processes (slope wind, surface albedo feedback) taking place at the sub-grid scale that are not included in *Alpine3D* (see Section 2.6).

The performance of the model in terms of hydrological response is satisfactory with a mean NSE coefficient of 0.78 (Figure 3.3a). The results are relatively homogenous in time and no significant difference is visible between the calibration and validation periods. The water year 2002 can be seen as outlier, however, runoff measurement errors were suspected for this specific year (Schaepli et al. [2016]). The comparison of the simulated and observed mean annual discharge (Figure 3.3b) indicates a slight underestimation (bias = $-0.12 \text{ m}^3 \text{ s}^{-1}$) of the discharge. This bias seems more pronounced for the wet years (2004, 2008, 2013), but it is difficult to find a convincing explanation for it (precipitation undercatch, wrong elevational gradient) without additional observations. Overall, these comparisons show the robustness of the model chain *Alpine3D-StreamFlow*. It must be emphasized that the model has only 3 calibrated parameters which is very parsimonious.

3.3.3 Melt energy

Figure 3.4 presents the surface energy flux available for melting/freezing the snowpack (in red) averaged over the fifteen years. This flux is computed for the entire basin, while taking into account only the snow-covered pixels. As expected, the flux is negligible during the winter period: the solar radiation is very limited and the snowpack loses energy through radiative cooling. The net change in energy is negative and thus, the snowpack is in a sub-freezing state (not shown). In March, the energy flux available for melting the snowpack becomes positive (even though it is very small), implying that part of the snow-covered area becomes isothermal (at 0° C). The onset of the melt season happens in April, but the energy flux shows a strong inter-annual variability (indicated by the standard deviation in black). Following the commencement of the melt season, the energy available for snowmelt increases significantly and reaches a maximum in July. In August, the available energy flux remains quite substantial and is followed by a rapid decrease in September.

On the right axis of Figure 3.4 (in blue), the energy flux available for melting the snow is multiplied by the snow-covered area of the basin. This combination shows the excess energy in the snowpack and also relates it with the snow availability in the basin. The dynamics are

Chapter 3. Energy partitioning during the snowmelt season in a high Alpine catchment

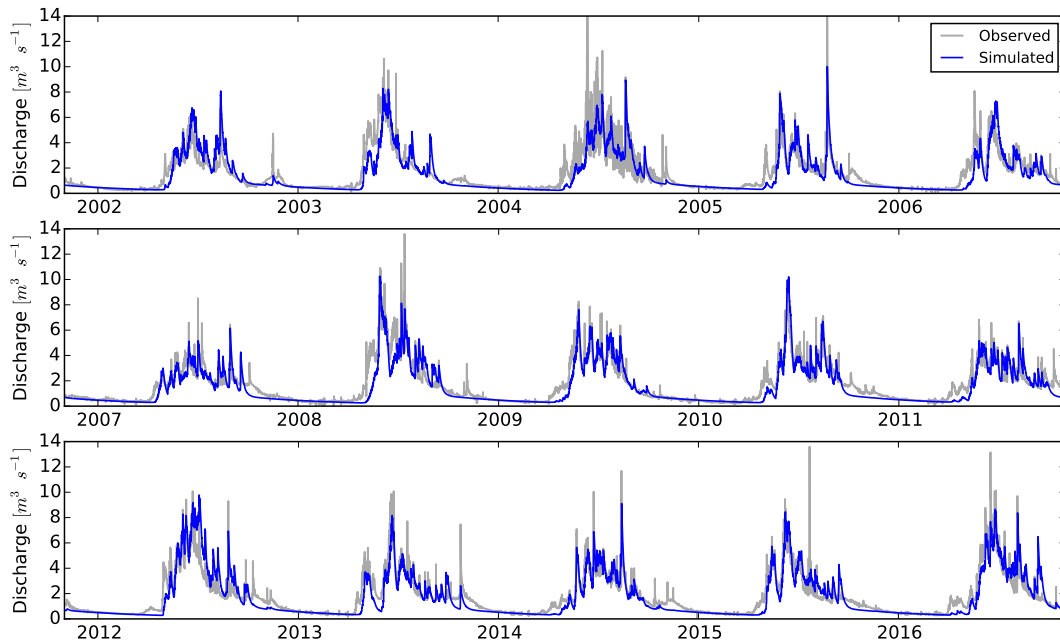


Figure 3.2 – Simulated and observed discharge at the Dischma basin outlet over the water years 2002-2016 using the *Alpine3D-StreamFlow* model chain.

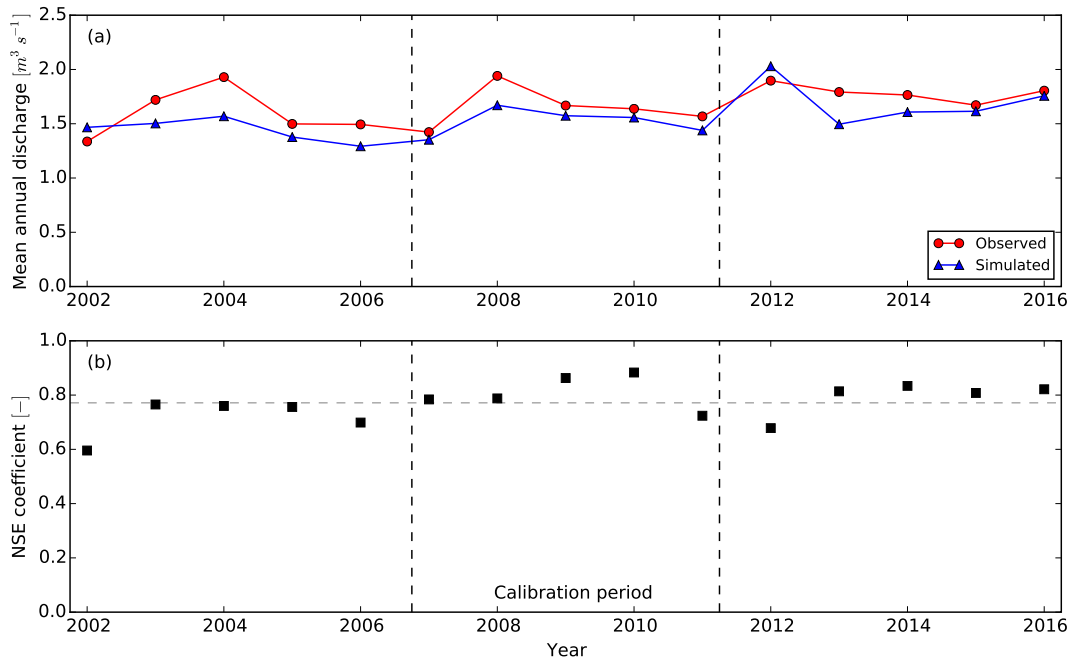


Figure 3.3 – (a) Mean annual discharge at the Dischma river outlet: observations are in red and simulated values in blue. (b) Performance of the model in term of Nash–Sutcliffe model efficiency coefficient over the period 2002-2016. The calibration period (2007-2011) is also indicated.

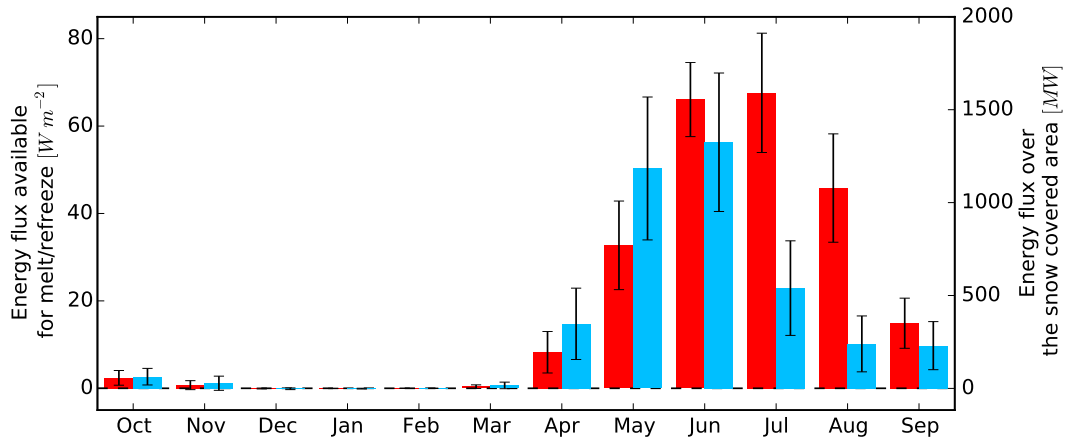


Figure 3.4 – Left axis: Energy flux available for melt/refreeze computed over the snow-covered area of the Dischma basin aggregated over the period 2002-2016 (red). Right axis: same as before but multiplied by the snow-covered area (blue). The black bars indicate the standard deviation over the 15 years.

fairly different from the energy flux (shown in red) with a maximum shifted from July to June. Additionally, we can see a transition from energy-limited snowmelt (in April and May) to a snow-limited ablation later in the season as the watershed is becoming snow-free.

3.3.4 Melt energy partitioning

The partitioning of the energy balance components at the snow surface is presented in Figure 3.5. As expected, the net shortwave radiation is the dominant energy input and follows a seasonal cycle with the maximum reached in June-July around the solstice. The net longwave radiation is always negative (i.e. net energy loss) and also shows a seasonal pattern. Due to the rise of the ambient air temperature, the incoming longwave radiation is increasing while the outgoing one is limited by the snow surface temperature close to $0^{\circ}C$. Surprisingly, the sensible heat flux is almost constant during the entire period (see also statistics in Table 3.2) while expecting a periodic signal due to rising air temperature. During the course of the ablation season, the snow covered area will decrease and retreat to higher elevation only where the air temperature is on average lower. This can partly explain a more or less constant sensible heat flux. Finally, the latent heat flux is negative at the beginning of the melt and becomes positive later, but remains relatively small compared to the other components throughout.

Chapter 3. Energy partitioning during the snowmelt season in a high Alpine catchment

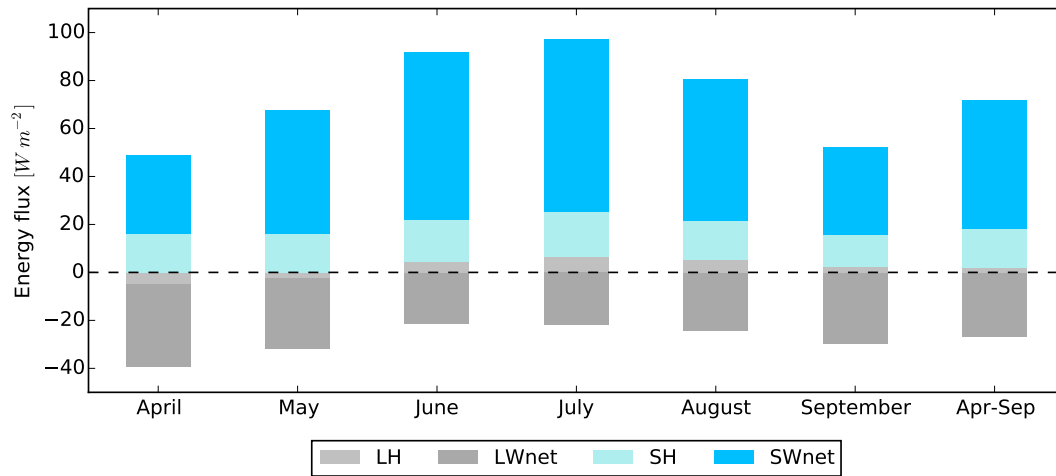


Figure 3.5 – Partitioning of the energy balance into its different terms over snow during the melt season. *LH* is the latent heat flux. *SH* is the sensible heat flux. *LWnet* and *SWnet* are the net longwave and shortwave radiation, respectively.

Table 3.2 – Statistics over 15 years of the net shortwave radiation (*SWnet*), net longwave radiation (*LWnet*) and sensible heat flux (*SH*) during the ablation season.

	Mean <i>SWnet</i> [$W m^{-2}$]	StD <i>SWnet</i> [$W m^{-2}$]	Mean <i>LWnet</i> [$W m^{-2}$]	StD <i>LWnet</i> [$W m^{-2}$]	Mean <i>SH</i> [$W m^{-2}$]	StD <i>SH</i> [$W m^{-2}$]
April	32.6	8.3	-34.3	6.3	16.3	4.5
May	51.5	8.1	-29.2	4.5	16.0	4.6
June	69.8	6.6	-21.5	4.8	17.6	3.1
July	71.8	10.6	-22.0	4.8	18.5	3.1
August	59.1	8.6	-24.3	3.8	16.1	4.6
September	36.4	5.4	-29.6	4.0	13.6	5.1
Apr-Sep	53.5	17.1	-26.8	6.6	16.4	4.5

3.4 Discussion

Aggregated over the entire basin, the ablation is therefore found to be mainly driven by three components: the net shortwave and longwave radiation together with the sensible heat flux. While early in the melt season, their magnitudes are roughly comparable, the shortwave radiation rapidly becomes the dominant component (Table 3.2). Consequently, its inter-annual variability has a strong signature on the ablation dynamics from one year to the other. The two other terms also show some inter-annual variability, most significantly at the beginning of the snowmelt season. While the predominance of the shortwave radiation and its seasonal cycle in the ablation process is not a surprise, one would expect a more pronounced seasonal cycle of the net longwave radiation and the sensible heat flux induced by the change of climatic conditions from spring to summer.

Alpine3D is one of the most detailed and advanced snow cover models in the scientific community. However, its current version at the given spatial resolution (100 m) is not able to

reproduce the complex interactions between the land surface and the atmosphere. The input data, interpolated from meteorological stations, does not capture local effects at the slope scale. Moreover, there will be no feedback, in the model, from the surface (snow or ground) on the local atmospheric conditions that could generate thermal winds or stable conditions. Due to the heterogeneity of the surface, the estimation of the turbulent fluxes between the land and the atmosphere can be very complex. Several studies have shown this complexity experimentally (Mott et al. [2017]) and numerically (Mott et al. [2011]) in the surroundings of the Dischma valley. The spatial resolution of the model and its coupling with an atmospheric model are notably critical factors. The estimation of the turbulent fluxes given by *Alpine3D* in the current study must be therefore interpreted cautiously.

From a hydrological point of view, this study shows some interesting outcomes: the coupling of a very detailed snow cover model and a relatively simple subsurface routine in the hydrological model gives good results over a long period (here 15 years). An important question often discussed in hydrological studies is the significance of the surface processes (precipitation distribution, snow processes) versus subsurface ones (water movement in the subsoil). In a high Alpine catchment such as the Dischma, the runoff generation is strongly dominated by snowmelt and the results presented above tend to show the importance of properly representing surface processes. The subsurface processes are also important but a more conceptual approach seems sufficient. Regarding the snow modeling, a very detailed model brings a non-negligible added value in terms of hydrological response.

3.5 Conclusions

The goal of this study is to identify the primary components of the energy balance during the ablation season. As expected, the melt energy shows a significant seasonal cycle from April to September. The ablation dynamics present two distinct periods: from energy-limited at the beginning to snow-limited later on when part of the basin is becoming snow-free. The ablation is principally driven by the net solar radiation and its inter-annual variability. Interestingly, the sensible heat flux remains almost constant during the entire melt season. This is partly explained by the snow retreat to higher elevation during the ablation season preserving it from high air temperature even during the summer months.

This study also enables us to assess the robustness of the *Alpine3D-StreamFlow* model chain. Over the water years 2002-2016, the physically based model accurately reproduces the snow accumulation and its melt when compared to observations (at the point scale and over the entire basin). The resulting hydrological simulation is also satisfactory and most importantly, the performance is relatively stable in time indicating a certain robustness of the calibrated parameter set. With the chosen configuration, the model chain seems reliable for hydrological modeling.

4 Spatio-temporal variability of snowmelt observed with an ultra-long range Terrestrial Laser Scanner

4.1 Introduction

During the last decades, significant advances have been made in remote sensing techniques, in particular for applications in cryospheric sciences (Rees [2006]). Snow and ice are challenging materials for remote sensing instruments mainly because of their radiative properties (high albedo and high emissivity) and have been, for a long time, difficult to measure accurately. Different techniques, mainly based on satellite sensors, have been developed to monitor snow covered areas, snow albedo or snow water equivalent (Nolin [2010]). Most of these techniques are based on passive sensors, measuring the energy naturally emitted or reflected by the snow surface. More recently, significant progress has been made with active systems, i.e. sending an energy pulse and recording the reflected signal.

In cryospheric science, one of the most significant developments consists of LiDAR (Light Detection And Ranging) systems suitable for snow and ice (Hopkinson et al. [2004], Deems and Painter [2006], Deems et al. [2013]). These systems can be launched on airborne platforms (Schöber et al. [2014], Grünwald and Lehning [2015], Painter et al. [2016]) but this technology remains expensive. An alternative is to operate it from a fixed vantage point on the ground (Schaffhauser et al. [2008], Egli et al. [2012]). In this latter configuration, the system is called a Terrestrial Laser Scanner (TLS). It has the advantage of being cheaper compared to airborne systems, which allows repeated scans during the winter. The reliability of TLS has been assessed against traditional methods (Prokop et al. [2008], Prokop [2008]) and such instruments

Chapter 4. Spatio-temporal variability of snowmelt observed with an ultra-long range Terrestrial Laser Scanner

have proven to provide high accuracy measurements. Moreover, this system enables very high-resolution spatial surveying of the snow surface unfeasible with traditional surveying techniques (due to cost reasons, accessibility and avalanche danger among others). During the last decade, LiDARs have been used intensively for studying spatial snow distribution and snowmelt (Egli et al. [2012], Revuelto et al. [2014]), elevation dependency of snow depth (Grünewald and Lehning [2011], Grünewald et al. [2014]), snow distribution over glaciers (Schöber et al. [2014]) and glacier mass balance (Fischer et al. [2016]). Finally, it has also been widely used for studying avalanche terrain (Deems et al. [2015], Prokop et al. [2015]). In spite of its great promise, TLS has two main disadvantages: it is limited by the line-of-sight and the range is often limited to a few hundreds of meters. The new generation of these instruments allows to overcome this latter limitation with ranges reaching several kilometers.

Taking advantage of this new generation of TLS, the goal of the present study is twofold: (1) investigate the spatial snow distribution at peak accumulation and (2) study how snowmelt is varying at high spatial resolution and in time over the entire ablation season in a high Alpine catchment. Using an ultra-long range TLS, we were able to scan a significant part of surrounding slopes (Figure 4.1). In addition, the surveyed area covers large aspect and elevation ranges. In order to capture the ablation dynamics in time, weekly surveys were performed from mid-April (at peak accumulation) to mid-June. By subtracting the raw snow surface data, we get high-resolution (0.5 m) snow depth maps along with ablation estimates. In a first step, we address the change in snow depth only. The estimation of the snow water equivalent (SWE), which is ultimately the variable of interest, will be addressed in a second step. In fact, when computing the snow water equivalent (SWE), the snow density has to be estimated (e.g. using the method of Jonas et al. [2009]). As we can expect, this step adds a significant uncertainty to the SWE estimation (Raleigh and Small [2017]).

4.2 Methods and data

4.2.1 Study site

The Dischma valley near the town of Davos in the Swiss Alps has been chosen for this study. The geomorphology of the valley, with two large gradual hillslopes (facing northeast and southwest) and a cirque at the southern edge, is particularly suitable for carrying out TLS surveys and studying differential snowmelt. The given topography allows to scan large areas with different aspects from a single site and, at the same time, to stay in safe terrain regarding avalanches. Moreover, the valley is close to its original state (i.e. no ski resort or large infrastructure) and relatively uncrowded during the winter/spring season (the TLS laser is not eye-safe at short distances).

In the present study, we focus on the upper part of the Dischma river basin (Figure 4.1). It has the advantage of having no forested area and only short vegetation (around 40 cm tall) and a few isolated trees, which makes data post-processing easier. To capture slopes with a wide range of elevation and aspect, we identified two suitable sites from where the surroundings were scanned. The first one, called "Wisenalp" (1912 m), is located at the intersection of the

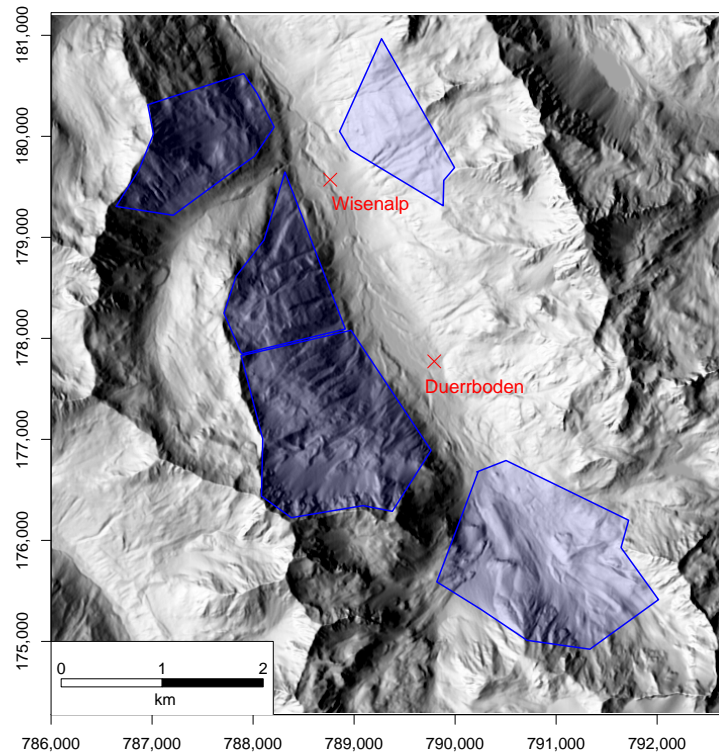


Figure 4.1 – The upper Dischma river basin with the two scanning sites: Wisenalp and Duerrboden, indicated with a red cross. The approximate scanned areas are indicated in blue. Easting/Northing are in the Swiss Geodetic Datum CH1903. Reproduced with permission from *swisstopo* (JA110138).

"Rinertalli" side valley with the main valley. From this site, we were able to scan both sides of the main valley, facing northeast and southwest, plus part of the lateral valley that has south-facing slopes (Figure 4.1). The scanning distance was approximately 2 km. The second site, "Duerrboden" (1995 m), is near the upper end of the Dischma valley. From this vantage point, we were able to scan the adjacent part of the northeast facing slope and part of the large bowl facing north. In this last configuration, the scanning distance reached up to 3 km, which is still far below the maximum range of the scanner in use (see Table 4.1).

Both scanning sites in the Dischma valley are surrounded by reflectors that have been installed on fixed structures such as electric poles, boulders or a cabin. Their exact positions, listed in Table 4.2, have been measured by combining a tacheometer and a GNSS receiver. From the scanning site, they are at distances of 75 to 350 m, which is much closer than the terrain in the field of view of the scanner. This configuration is not ideal to determine the absolute position of the scanner. However, their spatial distribution is very suitable to orient the scans relative to the geographic North.

Chapter 4. Spatio-temporal variability of snowmelt observed with an ultra-long range Terrestrial Laser Scanner

4.2.2 Instruments

Terrestrial Laser Scanner

A Terrestrial Laser Scanner (TLS) uses the same principle as a Radar or a Sodar but operates in the near-infrared domain of the electromagnetic spectrum. Its exact name is Light Detection and Ranging or LiDAR: the instrument emits a pulse of light and records the signal reflected by the terrain. In particular, the TLS must measure very accurately the Time-of-Flight (TOF) defined as the elapsed time between the pulse emission and its return. This TOF is then divided by two (to take into account the two-way trip) and multiplied by the speed of light in order to obtain the distance between the scanner and the terrain. A TLS provides data in its own cartesian coordinate system with the origin defined by its own position (Figure 4.2). This can be seen as a relative positioning and TLS data must then be georeferenced. This operation is carried out in combination with a GNSS receiver and is explained below.

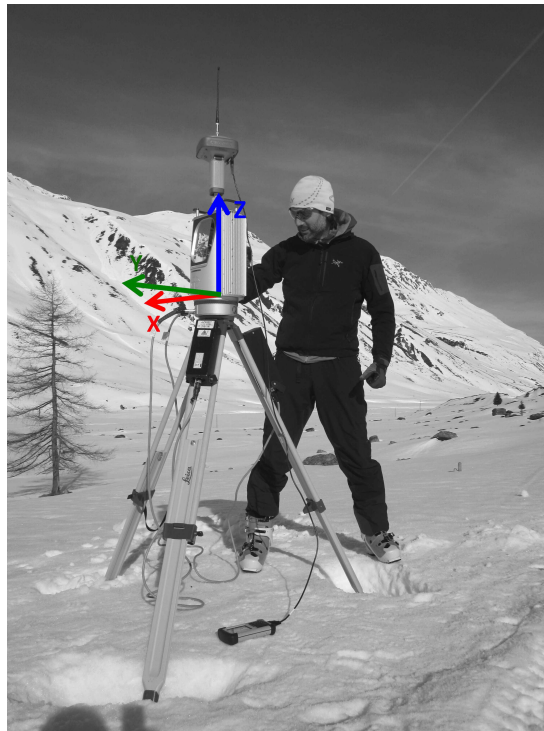


Figure 4.2 – Setup of the VZ-6000 TLS instrument in the Dischma valley with the GNSS receiver mounted on top. The scanner's own coordinate system is illustrated in color on the picture.

In the current study, we use the Riegl VZ-6000 TLS instrument (see Table 4.1 for its main characteristics). This TLS has an ultra-long range and can scan objects up to 6 km. The laser wavelength in the near-infrared band (1064 nm) is especially suited for ice and snow, which used to be a challenging material for LiDAR until recently. The drawback of this wavelength is that the laser is not eye-safe: it is harmful in case of direct exposition (diffuse reflections are safe) under a certain distance. In practice, we setup the instrument on small hills and choose

the scanning areas in order to avoid potential skiers or hikers.

Table 4.1 – Characteristics of the Riegl VZ-6000 terrestrial laser scanner.

Parameter	Value
Laser Wavelength	1064 nm (near-infrared)
Laser safety	Class 3B Laser
Max Range	up to 6000 m
Accuracy	15 mm
Precision	10 mm
Laser Beam Divergence	0.12 mrad
Used operating frequency	30-150 kHz

The operating frequency of the scanner determines the maximum range of the instrument. Depending on the distance to the slope, we operated it at a frequency varying between 30 kHz for very remote targets to 150 kHz for more close ones. We started surveying the snowpack at peak accumulation (April 15) and performed weekly scans with few exceptions due to bad weather conditions until mid-June. The scanning dates are presented in Table 4.3 for each site.

GNSS receiver

Raw TLS data are recorded in a local coordinate system and have to be related to a geodetic datum. For instance, one can measure the reflectors' position in the local reference frame and compute the scanner position in the global coordinate system by triangulation or triangulation. In our case, the main drawback of this method is the short distance between the scanner and the reflectors compared to the scanning distance. We opted for a more robust solution and mounted a GR5 Topcon GNSS receiver on top of the TLS (Figure 4.2). In most cases, the positioning survey was limited in time to the scan duration due to avalanche danger. To reach a satisfactory accuracy, the GNSS data were post-processed with the open-source RTKLIB software (Takasu and Yasuda [2009]). Through the Automated GNSS Network for Switzerland (AGNES, Ineichen et al. [2007]), *swisstopo* is providing corrections that can be applied to our GNSS measurements. The closest station from our field site is located in Davos, at a distance of about 10 km, which is very close for such a network ensuring small interpolation errors.

4.2.3 Point cloud post-processing

The TLS instrument is operating at high-frequency (see Table 4.1) while it can reach long ranges. This combination leads to range ambiguities that can be identified thanks to the multiple-time-around (MTA) capability of the scanner. The first step of the post-processing consists in determining the correct range of the target. This can be achieved by applying the manufacturer's software tool RiMTA TLS. Secondly, before georeferencing the data set, inclination errors of the TLS, induced by potential settling of the snowpack, small movements of the tripod or wind gusts during the acquisition time, have to be corrected. Finally, we have to georeference the data set to match the Swiss coordinate system.

Chapter 4. Spatio-temporal variability of snowmelt observed with an ultra-long range Terrestrial Laser Scanner

Table 4.2 – Position of the reflectors in the Swiss Geodetic CH1903 datum used to orientate the TLS data sets.

		Easting [m]	Northing [m]	Elevation [m]
Wisenalp site	Reflector 1	788'768.52	179'499.30	1'916.74
	Reflector 2	788'843.99	179'328.86	1'929.83
	Reflector 3	788'431.98	179'555.63	1'923.82
	Reflector 4	788'683.61	179'690.14	1'894.69
	Reflector 5	788'637.32	179'794.42	1'887.17
Duerrboden site	Reflector 1	789'853.73	177'885.20	2'016.54
	Reflector 2	789'616.03	177'957.80	1'981.83
	Reflector 3	789'491.57	177'945.48	1'971.68
	Reflector 4	789'521.71	177'766.89	1'975.49
	Reflector 5	789'614.85	177'727.66	1'978.16
	Reflector 6	789'711.47	177'556.13	1'990.77

Table 4.3 – Position of the scanner in the Swiss Geodetic CH1903 datum for each scan measured with a GPS and azimuth angle α relative to the North computed.

	Date	Easting [m]	Northing [m]	Elevation [m]	Azimuth [°]
Wisenalp site	14.04.2015	788'764.573	179'568.409	1'912.448	313.03
	24.04.2015	788'764.261	179'572.689	1'912.690	256.60
	29.04.2015	788'768.704	179'572.798	1'913.252	310.26
	07.05.2015	788'768.719	179'572.783	1'913.245	252.39
	13.05.2015	788'768.702	179'572.800	1'913.323	218.82
	29.05.2015	788'768.674	179'572.772	1'913.279	353.67
	05.06.2015	788'768.685	179'572.772	1'913.257	169.48
	11.06.2015	788'769.513	179'569.648	1'913.351	258.31
Duerrboden site	15.04.2015	789'757.009	177'802.921	1'991.657	213.56
	29.04.2015	789'794.544	177'835.091	1'998.507	340.16
	07.05.2015	789'801.700	177'827.961	1'999.455	196.52
	13.05.2015	789'787.022	177'773.378	1'994.860	252.17
	29.05.2015	789'802.891	177'829.495	1'999.614	252.99
	05.06.2015	789'793.586	177'771.165	1'995.297	159.07
	11.06.2015	789'793.635	177'771.899	1'995.163	37.29

Tilt correction

Before starting a scan, the TLS has to be carefully leveled. This operation is done in two steps: the rough adjustment is done with a spirit level while the fine tuning is performed electronically by the scanner itself. The TLS is mounted on a tripod which stands on a more or less soft surface (snow, soil) and can be influenced by the wind. In spite of a meticulous setup, the instrument is subject to small movements during a scan. Even if these changes are very small in absolute value, they can induce large errors for long distance scans. For example, at 3 km, a tilt of 0.01° results in an error of 0.5 m in the vertical coordinate. Note that the VZ-6000

scanner has a measurement range up to 6 km. To monitor these inclination changes, the TLS has two built-in inclinometers that measure the roll and pitch angles, respectively. Thus, we can use these data to correct the point cloud by applying a double rotation to each point. The detailed procedure for this step is presented in Appendix C.1.

Registration

Once the point cloud has been corrected for inclination errors, we can proceed to the registration of the data set. This operation consists of a translation (in the three dimensions) to the scanner position in the Swiss coordinates system, followed by a rotation around the vertical axis to orientate the point cloud relative to the North. The first operation is easy as we determine the position of the scanner with the GNSS receiver. The second is slightly more complicated: the azimuth of the scanner is computed using geodetic methods and measurements of the relative position of the reflectors located around the TLS. This procedure is explained in Appendix C.1. The last step of the post-processing procedure consists of generating a regular raster grid. For the data presented below, we choose a grid cell size of 50 cm.

4.3 Results

4.3.1 Snow depth change

The TLS derived change in snow depth from the beginning of the ablation season (14/15.04) until mid-June is illustrated for three different areas of the upper Dischma valley in Figures 4.3, 4.4 and 4.5, respectively. In June, most of the scanned hillslopes were snow-free and thus, the measurements in April represent the snow depth at peak accumulation. At first glance, a very high spatial variability of the snowpack can be noticed. At the watershed scale, the terrain aspect and the elevation seem to be the major factors explaining this variability. This is well illustrated by the differences between the two main valley flanks in Figure 4.5. The southwest-facing slopes accumulate less snow than the northeast-facing ones. Additionally, a positive altitudinal gradient can be noticed with higher terrain showing deeper snowpack. When looking at smaller areas at the hillslope scale, snow patterns follow the local topography featuring large accumulations at the foot of cliffs and long ribbons of snow in gullies and along certain ridges (Figure 4.3 and 4.4). Two processes explain these features: snow transport by wind and gravity-driven avalanches and sloughing (Sommer et al. [2015]). These observations are in good agreement with spatial scales described in respective literature (e.g. Brown and Goodison [2006]).

The scan-derived statistical distributions of the observed snow depths are presented in Figure 4.6 for the two scanning sites. The first distribution, in Wisenalp, is very well defined with a maximum of occurrences close to 0.5 m and a long skewed tail towards larger snow depths. The maximum snow depth is close to 5 m. The winter 2014-2015 was slightly below average in terms of snow accumulation in the region of Davos. It is interesting that even with a relatively shallow snowpack, the range of observed snow depths is large. This is explained by the different processes shaping the snow cover outlined in the previous paragraph. Note that

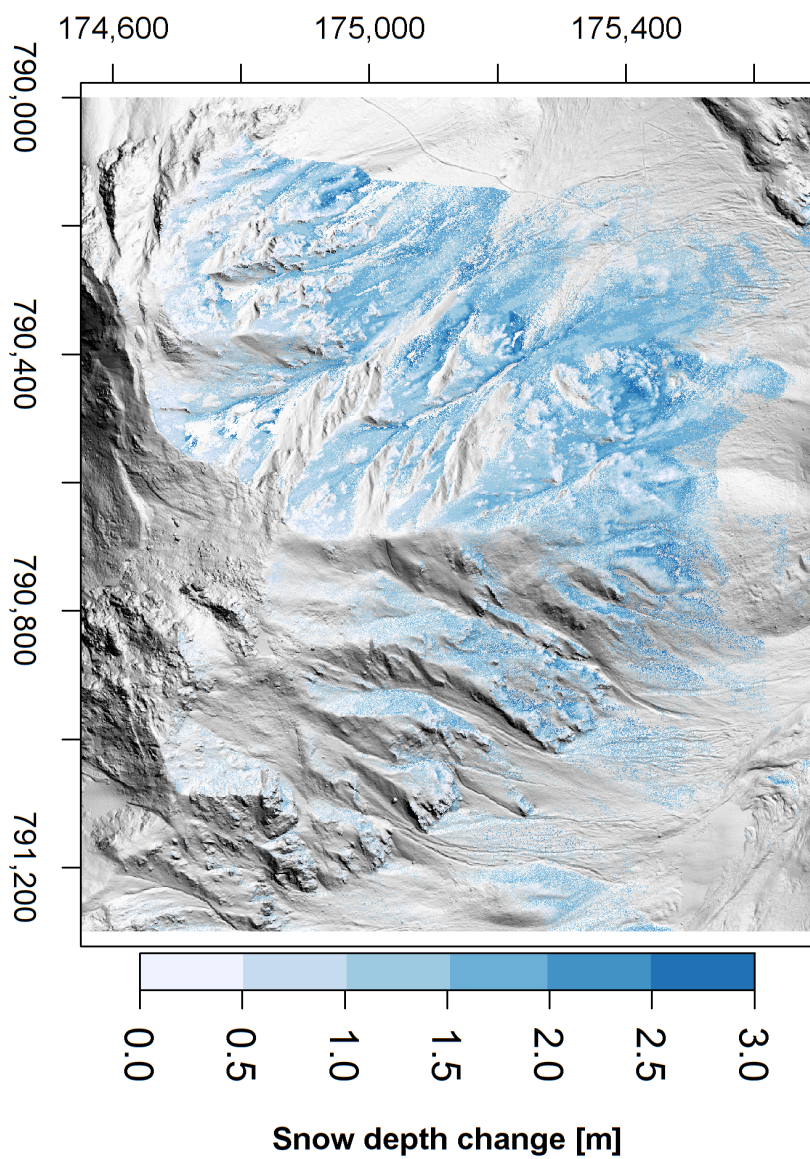


Figure 4.3 – Change in snow depth over the entire ablation season (15.04-11.06) in the headwaters of the Dischma valley (captured from Duerrboden).

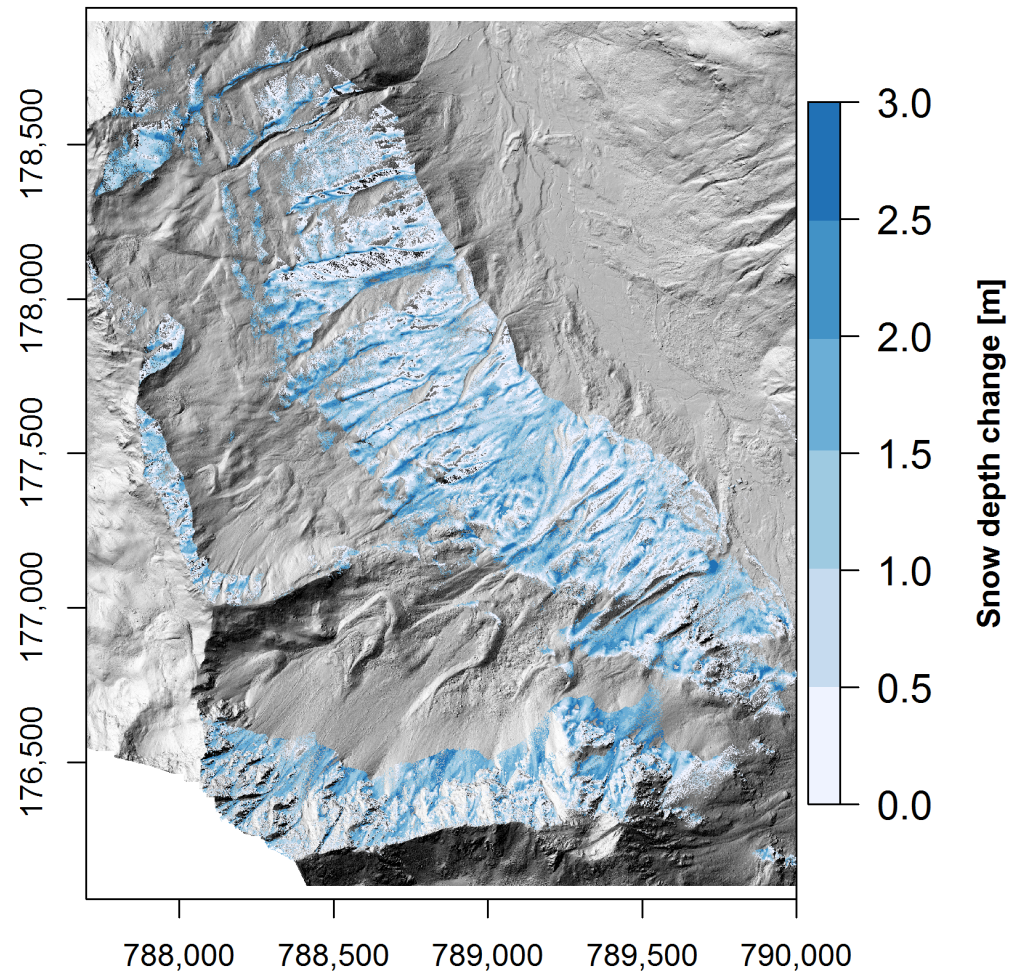


Figure 4.4 – Change in snow depth over the entire ablation season (15.04-11.06) on the left flank of the upper Dischma valley (captured from Duerrboden).

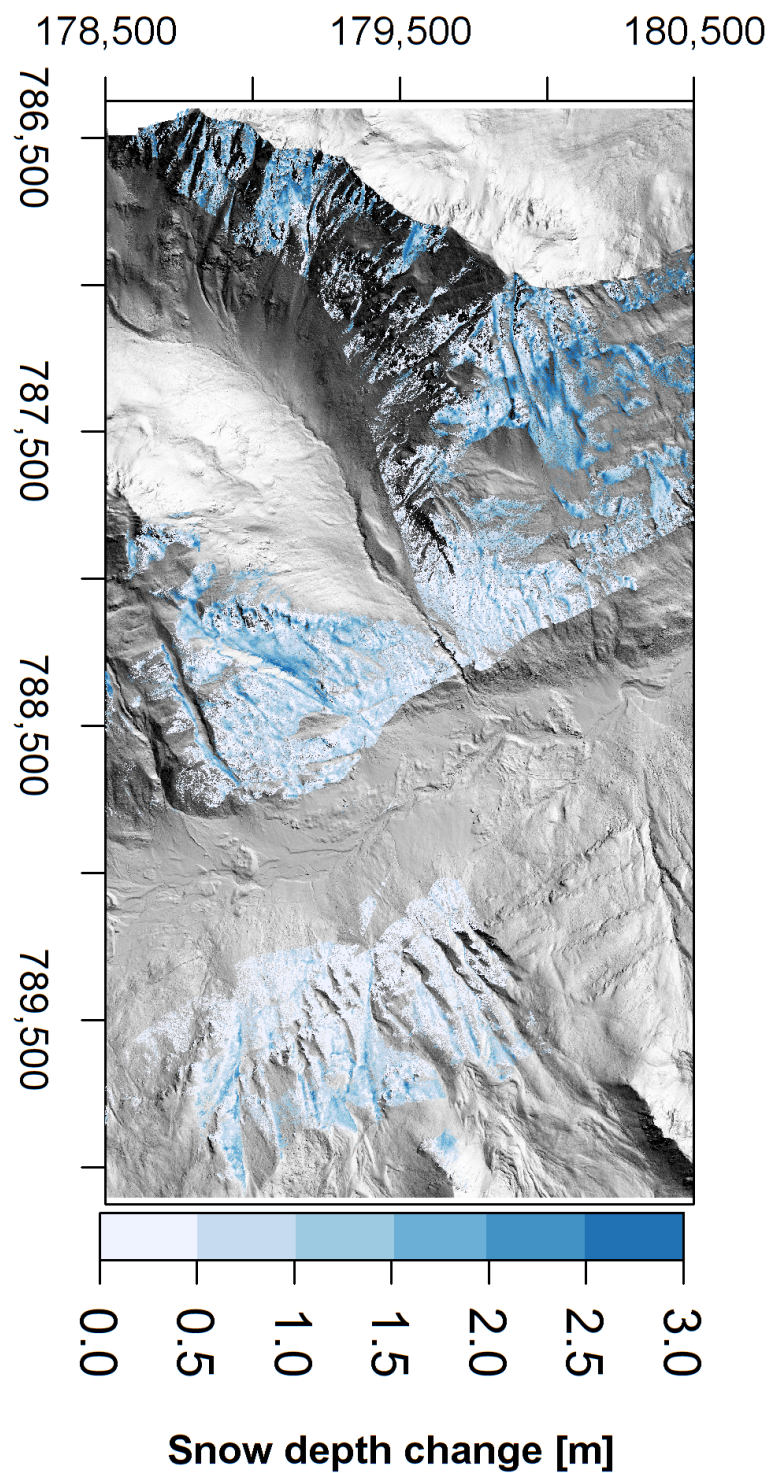


Figure 4.5 – Change in snow depth over the entire ablation (14.04-11.06) season both flanks of the main valley and the small Rinertaelli side-valley (captured from Wisenalp).

the peaks close to zero are due to limits of accuracy of the current setup and are not significant. At the Duerrboden site, the empirical distribution looks like a superposition of two distinct distributions with maxima at 1 m and 1.5 m, respectively. The kink in the tail close to 3 m supports this hypothesis. As the scanned terrain displays two principal aspects, north- and northeast-facing, it is assumed to be the combination of the respective snow distributions for each aspect. The two experimental distributions for the different aspects (N and NE), presented in Figure 4.7, confirm this assumption. It is worth noting that even a small change in aspect influences significantly the snow depth distribution. On average, Duerrboden site presents higher snow accumulation compared to the Wisenalp site due to the differences in aspect and elevation which is expected to result in different ablation dynamics.

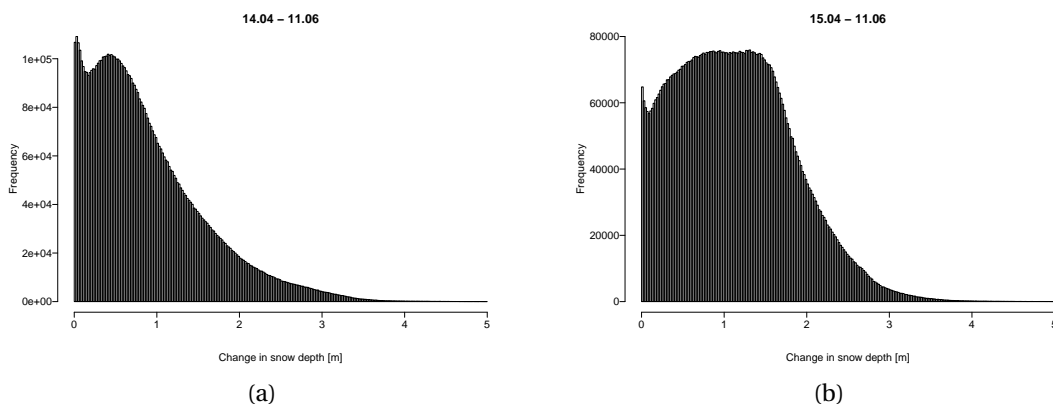


Figure 4.6 – Empirical statistical distributions of the observed snow depth from (a) Wisenalp and (b) Duerrboden.

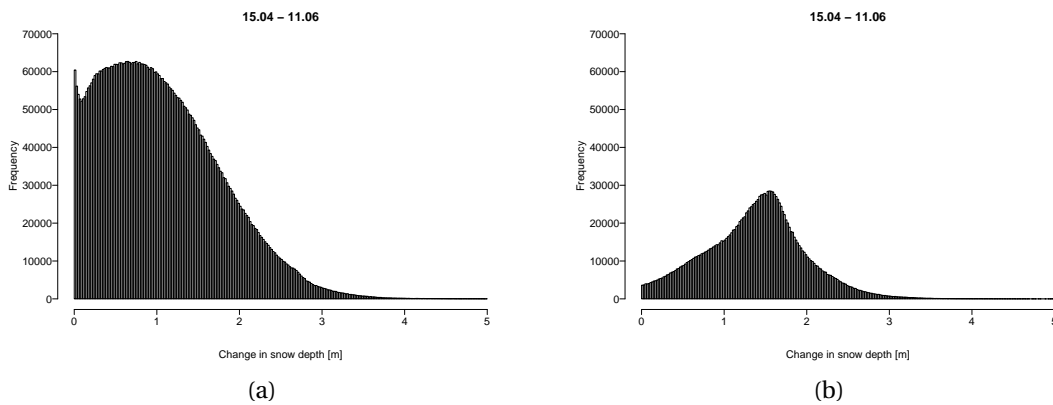


Figure 4.7 – Empirical statistical distributions of the observed snow depth from Duerrboden (a) on the northeast-facing slopes and (b) north-facing slopes.

4.3.2 Ablation rate

By subtracting successive scans, we obtain for each time period (between two scans) a change in snow depth. We convert this into an ablation rate per day and present the results as histograms in Figure 4.8 and 4.9 for the two vantage points.

The snowmelt dynamics computed for this area over the entire ablation season unveil a few surprising features. In Wisenalp, one can observe a bi-modal distribution in the ablation rate with two maxima almost superimposed at the very beginning (14-24 April) (Figure 4.8a), which then proceed to separate as the season progresses (Figures 4.8b to d). The first peak is decreasing toward zero ablation rate. Whereas, the second distribution shows a shift toward larger ablation rates. From mid-May on (Figure 4.8e), most of the slopes are becoming snow-free in this part of the catchment and the bi-modal feature has disappeared. The ablation rates are then slowly decreasing reaching small values in June (Figure 4.8f and g). At that time of the year, only snow patches are remaining around Wisenalp.

At Duerrboden, a similar bi-modal pattern is observable, even though the timing is delayed compared to the Wisenalp site. At the very beginning, the ablation rates are relatively small and rather homogeneous (<5 cm per day) (Figure 4.9a and b). In early May (29 April - 07 May), the two modes are already visible (Figure 4.9b). Their split happens around mid-May (Figure 4.9c) and persists until mid-June (Figures 4.9d to f). Note that a bad weather event happened between 13 and 29 May explaining the change in the ablation dynamics during that period (also visible to some extent at Wisenalp).

It is proposed that the bi-modal distribution in the observed ablation rate is linked to the driving processes of the snowmelt. At the slope scale, when the initial snowpack is relatively shallow, the snow cover rapidly becomes patchy and the snow covered area (SCA) decreases. In this case, the limiting factor is not the energy input but the confined area covered by snow. As the SCA decreases, the ablation rate distribution tends toward lower values (averaged over a period of time). Conversely, for a thicker snowpack, the limiting factor is the energy input as the SCA remains more or less constant. During the course of the melt season, ablation rates increase together with the energy input. In summary, slopes with shallow snowpacks experience a snow-limited ablation while slopes with deeper snow accumulations are energy-limited. This finding is preliminary and requires further investigation to be corroborated but is already supported by many elements and results from the present study. To the best of our knowledge, this is the first time these process dynamics have been captured and described from detailed spatially distributed and time resolved observational field data.

4.4 Conclusions

In the present study, we investigated the spatial and temporal variability of the snow depth and snowmelt in an Alpine valley above the treeline, the Dischma valley near Davos, Switzerland. Using an ultra-long range Terrestrial Laser Scanner (TLS), we performed repeated scans of snow covered hillslopes with different aspects and elevation ranges from the seasonal peak accumulation in April to the end of the melt season in June. The spatial variability of snow

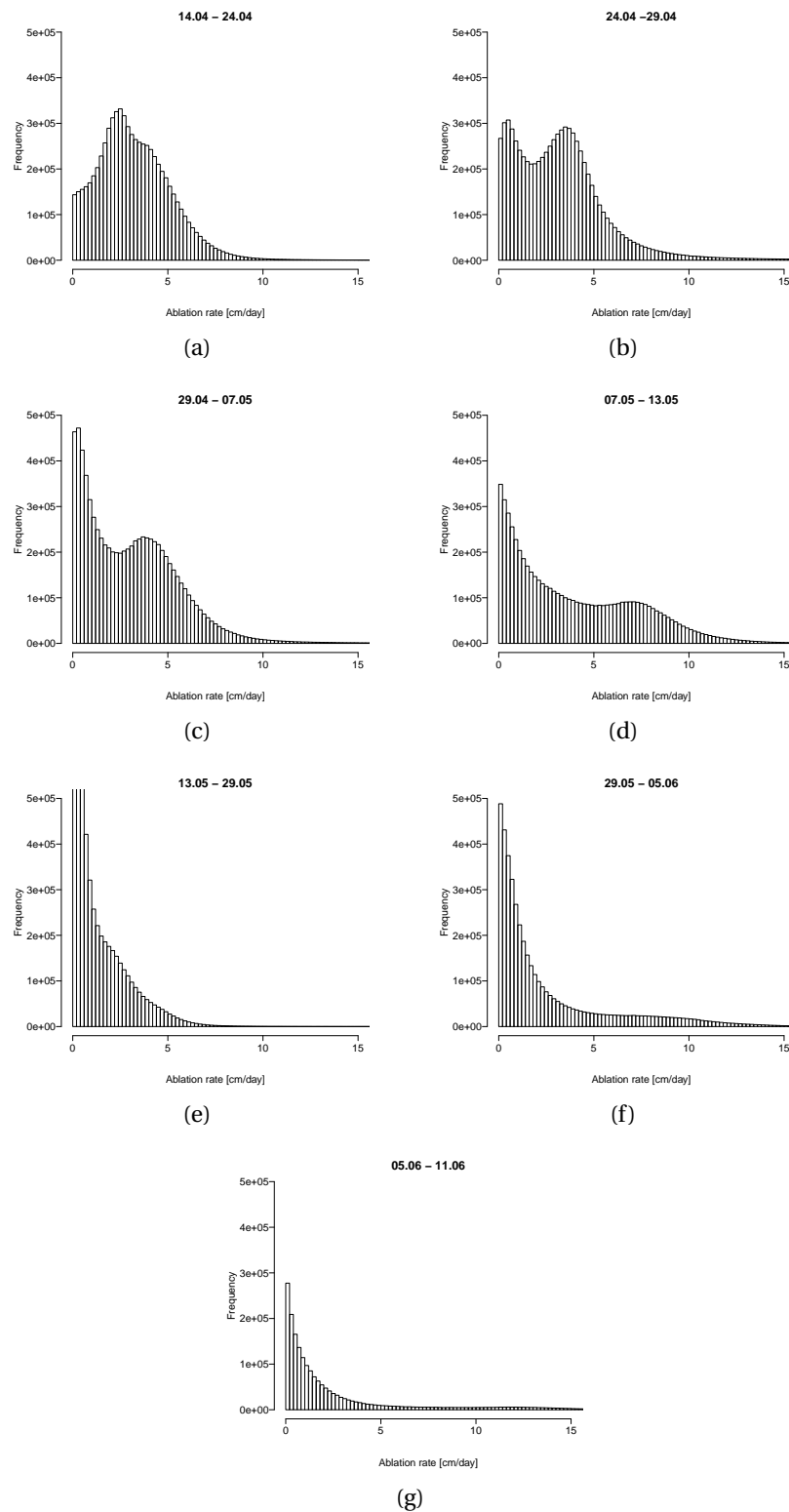


Figure 4.8 – Histograms of snow ablation rate (in centimeter per day) in between scans (dates are indicated on each sub-figure) for the Wisenalp scanning area.

Chapter 4. Spatio-temporal variability of snowmelt observed with an ultra-long range Terrestrial Laser Scanner

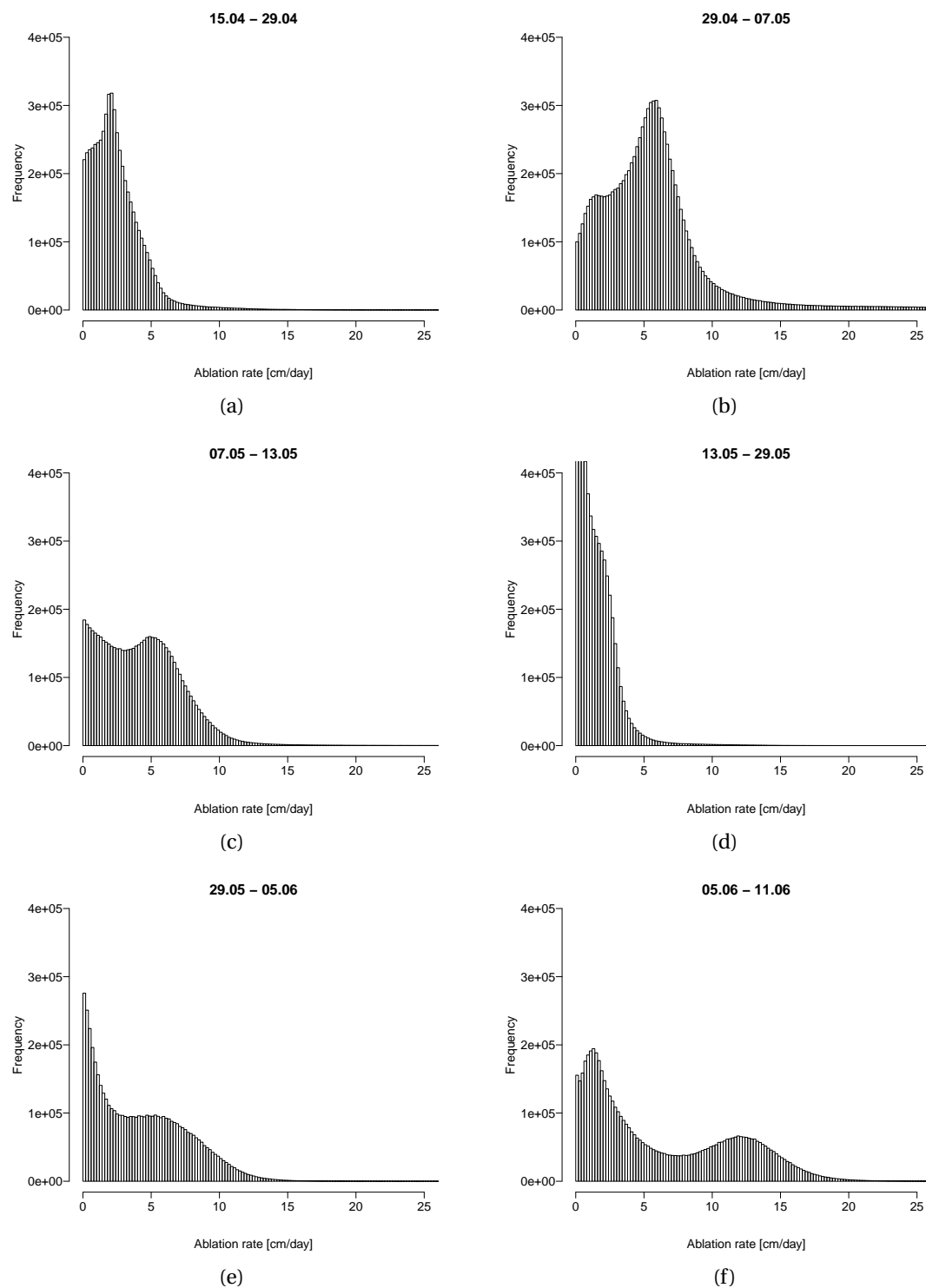


Figure 4.9 – Histograms of snow ablation rate (in centimeter per day) in between scans (dates are indicated on each sub-figure) for the Duerrboden scanning area.

depth was found to be very high at peak accumulation. This heterogeneity is explained by the altitudinal gradient of precipitation and slope aspect processes significantly shaping the snow cover at the watershed scale, and wind induced snow (re-)distribution and avalanches, dominant processes at the hillslope scale. The ablation dynamics show a bi-modal distribution with a separation between lower ablation rates and higher ones as a result of prevailing processes and conditions. This feature remains visible during most of the melt season. It is assumed that the two modes are linked to the driving processes of the snow ablation: (1) over shallow snowpack areas, the snow covered area (SCA) is the limiting factor while the energy input is the major constraint over areas with an initially deeper snow cover.

5 A low-cost Sensible Heat Flux sensor for Wireless Sensor Networks

This chapter will be submitted for potential publication in the MDPI open-access journal *Sensors*.

5.1 Introduction

In geoscience, determining the Earth's energy balance and its partitioning between the different components are usually a prerequisite to any further analysis. For example, in boundary layer meteorology, the system dynamics and water balance are driven by the net energy budget of the system. In the more applied domain of agronomics, plant growth and its needs in terms of water are partly determined by the energy balance at the Earth's surface. This latter is also influencing the soil moisture evolution and then, the potential necessity for irrigation in order to ensure crop security. Figure 5.1 depicts the main components of this budget (see for example Foken and Nappo [2008] for a complete introduction): the shortwave radiation, originating from the sun, is partly reflected by the surface and represents the major energy

source. This flux is partially counterbalanced by the infrared or longwave radiation emitted from the Earth's surface but also from the atmosphere and clouds. Despite being relatively small, ground heat flux transfers energy to the soil layer during daytime and releases it during the night dampening the soil temperature changes (Hatfield et al. [2005]). Besides radiative and conductive heat fluxes, the sensible heat flux is a crucial component of the Earth's surface energy balance and constitutes the process of turbulent convective heat exchange between the atmosphere and the land surface. It is of importance for agriculture, urban heat budgets, and for understanding consequences of climate change. It is also directly related to and drives the turbulent latent heat transport, which is the flux of moisture between the surface and the atmosphere, also known as evapo(-transpi)ration. The latter is a major component in the hydrological cycle and balances together with runoff the precipitation inputs.

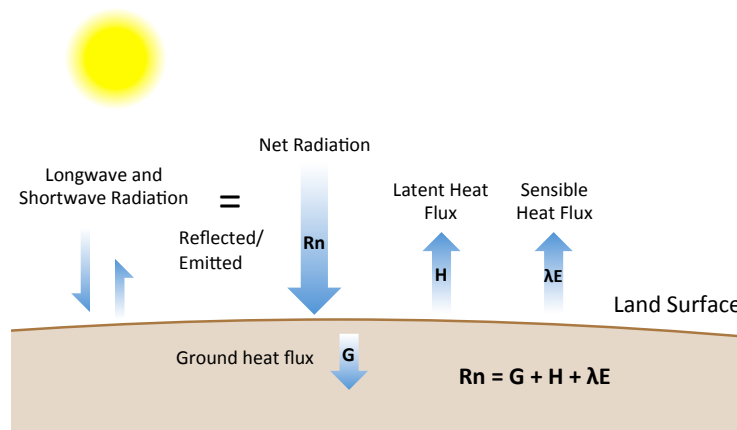


Figure 5.1 – Illustration of the surface energy balance. The net radiation (R_n) is the difference of the incoming and the reflected shortwave radiation, plus the difference between incoming and outgoing longwave radiation. The ground heat flux (G) is the conductive flux in the soil. The turbulent heat fluxes include the sensible heat (H) and the latent heat (λE).

In spite of their importance, notably in the context of climate change, turbulent heat fluxes of the energy balance are complicated and/or expensive to measure accurately. Therefore, independent measurements of all energy balance components are often sparse and limited to a few sites with complete energy balance instrumentation. In the present study, we try to overcome this limitation by presenting a new low-cost sensible heat flux sensor as a possible solution. In the framework of the EU FP7 project *WeSenseIt*¹ (Lanfranchi et al. [2014], Wehn et al. [2015], Ciravegna et al. [2013], Mazzoleni et al. [2018]), a Citizen Observatory of water has been developed and implemented. One of the objectives was to go beyond the observation of classical water-related variables by also measuring sensible heat flux. Even though this component is less accessible and important for citizens compared to other quantities (e.g. water level in a stream, rain intensity or snow depth), sensible heat flux provides essential information. Indeed, combined with a net radiometer and soil heat flux sensor, it is possible to

¹www.wesenseit.eu

close the local surface energy budget and estimate the latent heat flux which is rarely measured as a residual:

$$\lambda E = R_n - G - H \quad (5.1)$$

Even though several methods exist to measure sensible heat flux (e.g. bulk aerodynamic method, gradient method, surface renewal, Huwald et al. [2018]), the most common and direct one is based on eddy covariance (EC) requiring high frequency wind and temperature measurements (Swinbank [1951], Baldocchi [2014]). Unfortunately, such a sensor is expensive (~10k €) not considering the data logging system. Based on a different theoretical approach, which builds on flux variance (Tillman [1972], Albertson et al. [1995]), the goal here is to develop and test a low-cost sensible heat flux sensor (<100 €). The flux computation requires high-frequency air temperature fluctuation data only. Compared to benchmark instruments, the expected accuracy will be lower but may be compensated by the availability of multiple sensors. This enables new applications otherwise difficult to achieve due to cost limitations such as spatial variability of the sensible heat flux by installing several sensors, for example, in a wireless sensor network (WSN). Sensors may also be used by farmers to manage their crop at the field scale.

The chapter is organized as follows: first the development of the new sensible heat flux sensor is presented (Section 5.2.1), notably the theory on which it relies, the choice of the temperature sensor and the sensor interfacing. Then the eddy covariance method (Section 5.2.4) that will be used as a reference for the new sensor is briefly introduced. Section 5.2.5 presents the setup of the validation experiment carried out during summer 2015. The experimental results and the sensible heat flux sensor validation are presented in Section 5.3, followed by a general discussion and suggestion of some potential improvements.

5.2 Materials and Methods

5.2.1 Flux Variance Method

In the atmospheric boundary layer (ABL), turbulences can be generated either by mechanical forces (wind shear) or buoyancy (thermal updrafts). When vertical motions driven by buoyant forces are dominant (compared to horizontal ones), the system is in a free convection state (Stull [1988]). For these specific conditions, Albertson et al. [1995] derived a method to estimate the sensible heat flux based on Monin-Obukhov similarity theory (MOST) (Monin and Obukhov [1954]) and the approach developed by Tillman [1972]. This method is called flux variance (FV), relies on the second moment of air temperature and only requires a high-frequency temperature measurement, which is a significant advantage compared to other methods (e.g. the eddy covariance method presented in Section 5.2.4). With reference to the second moment of the temperature measurements, the method is also referred to as the σ_T method. Following Albertson et al. [1995] the sensible heat flux H [W m^{-2}] can be computed

as follows:

$$H = \sigma_T^{3/2} \bar{T}^{-1/2} \rho c_p C_1^{-3/2} (k g z)^{1/2} \quad (5.2)$$

where: σ_T = air temperature standard deviation [K]

\bar{T} = mean air temperature [K]

ρ = density of air [kg m^{-3}]

c_p = specific heat capacity of air [$\text{J kg}^{-1} \text{K}^{-1}$]

C_1 = constant from the literature (= 0.97, see Albertson et al. [1995] for details)

k = von Karman constant (= 0.4 [-])

g = gravitational acceleration (= 9.81 m s^{-2})

z = measurement height above land surface [m]

The theoretical foundation of the FV method requires that three main hypotheses are fulfilled:

1. Convective conditions: buoyancy must be the driving force of vertical movement in the ABL. In practice, the dimensionless stability parameter ζ must be smaller than -0.15:

$$\zeta = \frac{z}{L} = \frac{-k z g \overline{w' T'}}{u_*^3 \bar{T}} \quad (5.3)$$

where: $\overline{w' T'}$ = covariance in time of vertical wind velocity and air temperature [$\text{m s}^{-1} \text{K}$]

\bar{T} = mean air temperature [K]

u_* = friction velocity [m s^{-1}]

ρ = density of air [kg m^{-3}]

c_p = specific heat capacity of air [$\text{J kg}^{-1} \text{K}^{-1}$]

k = von Karman constant (= 0.4 [-])

g = gravitational acceleration (= 9.81 m s^{-2})

z = measurement height above land surface [m]

2. Stationarity in time: this condition is met if all statistical moments of a random process are time-independent. In practice, the stationarity is insured by choosing a short enough averaging interval.
3. Surface homogeneity: the process should be constant in space. In practice, the station is setup with a sufficient fetch length around it.

5.2.2 Choice of the temperature sensor

A first challenge in the developing process was to select suitable temperature sensors, with sufficiently fast response time to ambient air temperature fluctuations. Several other criteria had to be matched, such as feasibility and flexibility for interfacing, cost (<100 €) and resistance to the elements (rain, wind, hail), but also bugs, insects or birds. Especially the latter constraint is difficult to fulfill, as the sensing element has to be fully exposed to the air and should be as small as possible to minimize thermal inertia and flow disturbance by the sensor itself. In this case, air temperature fluctuations should be measured and resolved at a frequency of minimally 1-2 Hz (Huwald et al. [2018]). Another issue is that the sensor should have the smallest possible self-heating to avoid creating artificial convection and turbulence around the sensing element and thus perturbing the natural airflow. Finally, the energy consumption must be low (mW) to make the sensor suitable for autonomous stations, nodes in WSNs or to use it combined with low-cost data logging systems (e.g. Arduino board (Mellis et al. [2007], Banzi and Shiloh [2014]) or Raspberry Pi board (Richardson and Wallace [2012]), etc.). Three sensors presented in Table 5.1 were selected as candidates satisfying a priori most of the requirements listed above.

Table 5.1 – Commercial temperature sensors selected as candidates for the development of the sensible heat flux sensor and their technical specifications.

Sensor type	Manufacturer	Sensor model	Time constant in still air	Price
Glass-beaded NTC thermistor	General Electric	FP07	0.1 s	100€
Small NTC thermistor	Honeywell	111 series	0.5 s	<10€
Fine wire thermocouple	OMEGA	Type E, 0.08 mm	0.1 s	10 €

The different sensors were tested extensively in laboratory and real outdoor conditions and compared to a 3D sonic anemometer (Campbell Scientific, Inc. [2017]) which is a reference for high frequency air temperature measurements. Several experiments were carried out in order to analyze and characterize the sensor reactivity. Despite the promising manufacturer specifications, the glass-beaded negative temperature coefficient (NTC) thermistor was not able to resolve the temperature fluctuations seen by the reference and the alternative sensors (Figure 5.2). Detailed investigations lead us to the conclusion that solar radiation was heating the small glass bead and its thermal inertia was perturbing air temperature measurements. This hypothesis was confirmed by a heat dissipation experiment (not shown) consisting in warming the sensors and measuring the relaxation time needed to reach the ambient temperature. Consequently, the glass-beaded NTC thermistor was an unsatisfactory choice for this application and was no longer considered.

The frequency spectra presented in Figure 5.3 pinpoint that no candidate sensor is as sensitive as the reference. This is also not necessary to still make use of the selected approach. Nevertheless, the fine wire thermocouple and the small NTC thermistor show good, almost

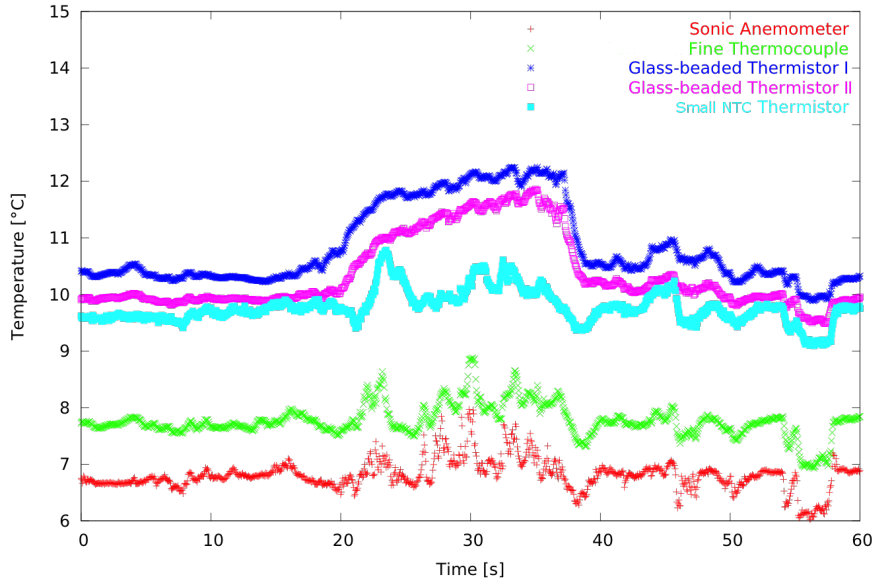


Figure 5.2 – Air temperature measured with different sensors. The temperature increase observed after 20 seconds results from increased solar radiation due to decreasing cloudiness during that period. The two glass-beaded NTC thermistors are susceptible to solar radiation absorption and thermal inertia by not responding to high-frequency air temperature variations.

comparable performance to the reference at low frequency ($< 1\text{ Hz}$). Consequently, the choice between these two sensors can be made on other criteria such as robustness and price. The thermistor is cheaper but also more fragile due to its design. We finally selected the fine wire thermocouple (TC) because of its relative robustness given its small diameter and high sensitivity.

5.2.3 Sensor interfacing

A thermocouple (TC) is a type of temperature sensor based on the Seebeck effect at the junction of two different metals (alloys). It relates a temperature difference between two points to an electrical voltage. If the temperature at one junction of the two wires (hot junction at a reference temperature) changes slowly, we can measure the changes at the other (cold) junction, i.e. the sensor tip. This type of sensor is not very accurate in absolute value but allows measuring fast and small temperature changes such as those caused by turbulent air convection. Several types of TC are available, depending on the material used. In the present study, we used a Type E TC made of chromel (90 % Ni, 10 % Cr) and constantan (45 % Ni, 55 % Cu). This TC type was chosen because of its wide availability, ability to operate at ambient temperature, low cost and high sensitivity ($68\text{ }\mu\text{V K}^{-1}$).

Before being converted to digital values, the TC signal is subject to analog pre-processing. As presented in Figure 5.4, the resistors R_{B1} and R_{B2} are used to bias the TC into a voltage range accepted by the Analog to Digital Converter (ADC). The resistors R_{F1} and R_{F2} together with

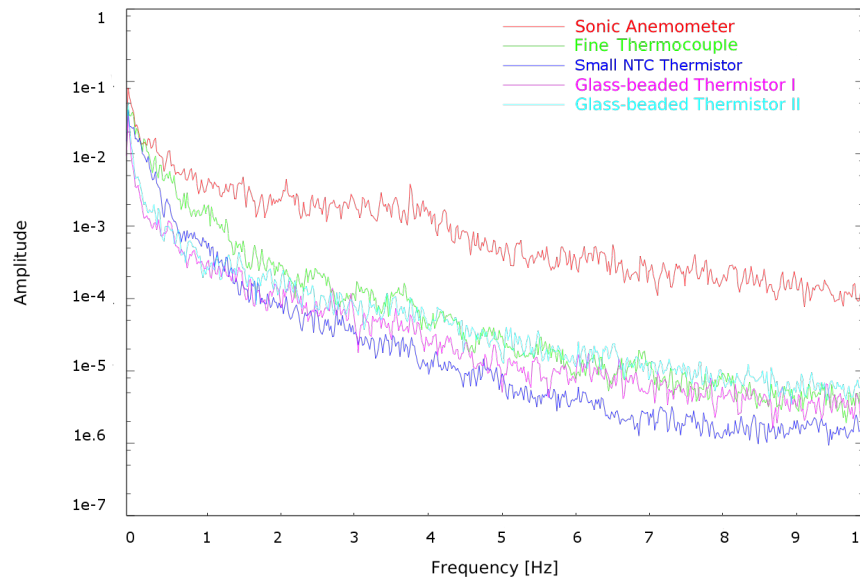


Figure 5.3 – Power spectra of the different temperature sensors.

capacitors form a low pass filter used to avoid aliasing. The capacitor C_{DIF} suppresses the differential noise while C_{CM1} and C_{CM2} take care of the common mode noise. The signal goes to the differential ADC for processing by the embedded micro-controller. Its high resolution (20 bits) allows measurements up to $46 \mu^{\circ} \text{C}$. The converter also provides a built-in temperature sensor, which gives the temperature at the hot junction of the TC.

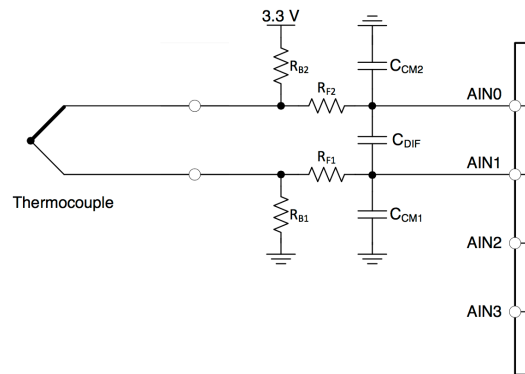


Figure 5.4 – Electronic schematics of the thermocouple signal conditioning.

The device stays in low power mode until it receives a command from the data logger to start acquisition. The internal temperature of the device is then measured using the ADC built-in temperature sensor. This value is kept as a reference for the internal TC junction. The device then takes a configurable number of measurements and computes mean and variance over the specified time period. As these quantities are computed using an incremental algorithm, there

Chapter 5. A low-cost Sensible Heat Flux sensor for Wireless Sensor Networks

is no memory restriction on the number of samples. Once the measurement is completed, the data logger pulls the data from the sensor, which goes back to sleep. This procedure ensures minimal power consumption.

The current sensor setup with its enclosure is presented in Figure 5.5. The TC is protected by a 2.5 mm diameter and 250 mm long stainless steel tube from which the sensor tip sticks out by approximately 5 mm. This way the TC is protected from environmental conditions with, at the same time, a minimum disturbance of the flow field. The TC is connected to a printed circuit board (PCB) that reads the analogue signal and processes it into digital values according to the procedure described above. Finally, the sensible heat flux sensor can be connected to any standard data logger using the SDI-12 protocol (SDI-12 Support Group (Technical Committee) [2017]). This allows the users to choose their preferred experimental platform and to integrate the sensible heat flux sensor in existing setups. Other supported communication protocols are available on the PCB (CAN, UART, I2C and USB) but require additional software development.

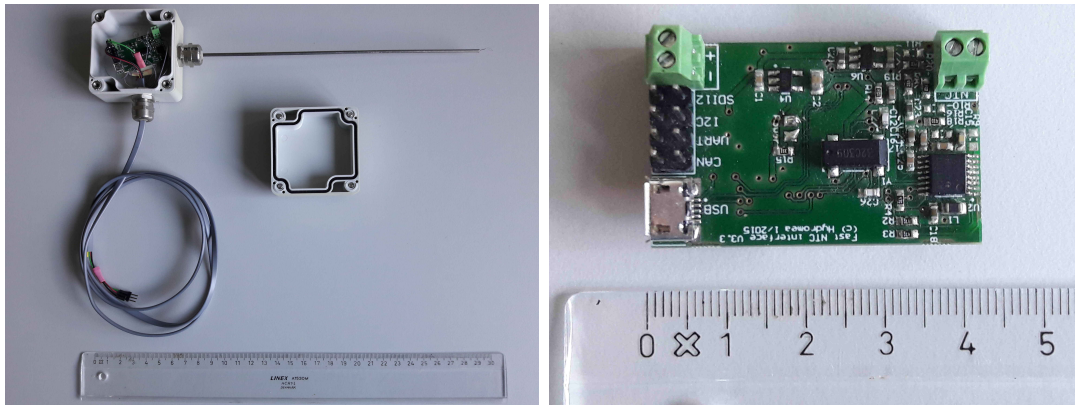


Figure 5.5 – Sensible heat flux sensor setup. Left: the TC is located at the end of the tube and connected to the PCB enclosed in a IP66 box. The cable connects the sensible heat flux sensor to any data logger. Right: detailed view of the custom-made PCB.

Cost reduction with respect to standard sensible heat flux sensors has been one of the main objectives for developing this sensor. The price of the different components are presented in Table 5.2: the total cost is currently below 100 € which is in itself an achievement. Naturally, the custom-made PCB remains the most expensive part of the sensor but will get cheaper if larger numbers get produced. The thermocouple itself is inexpensive, and can be changed easily in case it gets damaged.

In view of using this sensor in WSN and potentially as a component on sensing stations of a Citizen Observatory (e.g. Ciravegna et al. [2013]), the SHF sensors have been tested and used by a group of students in the context of a laboratory course on measurement methods in atmospheric physics. For this purpose, the sensor was interfaced with an Arduino UNO board (Banzi and Shiloh [2014]). This cheap data logger (~50 €) including a SD card logging shield and real time clock is an ideal solution for students and shows a great potential for a Citizen Observatory. Indeed, this allows having several sensors available and measuring

simultaneously the spatial variability of sensible heat flux over spatially heterogeneous terrain.

Table 5.2 – Cost breakdown of the sensible heat flux sensor.

Parts	Price
OMEGA fine wire TC, type E, diam. 0.08 mm	10 €
Printed Circuit Board	50 €
Enclosure box IP66	8 €
Stainless steel tube	5 €
Cable glands (2x)	6 €
Cable & others	3 €
Total	82 €

5.2.4 Eddy Covariance Method

The eddy covariance (EC) method has been the reference for measuring sensible heat flux in ABL meteorology for decades (see e.g. Aubinet et al. [2012] for a full method description and a detailed review). It requires simultaneous high frequency vertical wind velocity (w) and temperature (T) measurements that are generally measured with a 3D sonic anemometer. Applying a Reynolds decomposition on these measurements, one can isolate the fluctuating part, w' and T' respectively, of each time series. Then the covariance in time $\overline{w'T'}$ can be computed. The prime notation indicates the fluctuating part of a variable after subtraction of the mean, the overbar denotes the time average over the selected sampling interval. Finally, the sensible heat flux in $[W m^{-2}]$ is obtained as follows:

$$H = \rho c_p \overline{w'T'} \quad (5.4)$$

where: $\overline{w'T'}$ = covariance between the vertical velocity and temperature fluctuations $[ms^{-1}K]$
 ρ = density of air $[kg m^{-3}]$
 c_p = specific heat capacity of air $[J kg^{-1}K^{-1}]$

In order to ensure satisfactory results, raw data must be carefully post-processed. In the present study, the following steps were implemented:

- Data selection based on wind direction. The station mast and the sonic anemometer instrument body are perturbing the airflow and indirectly the computed fluxes between the surface and the atmosphere. To avoid this issue, we only kept data within an angle of $\pm 150^\circ$ from the sonic anemometer horizontal (x-)axis pointing into the dominant wind direction.
- Tilt correction. The EC method requires a negligible mean vertical wind component. By applying a double rotation, the sonic anemometer coordinate system is aligned with the

local wind streamlines. In the current study, we used the method proposed by Wilczak et al. [2001].

- Linear detrending of wind and temperature time series over the sampling interval.

The EC method mainly has two drawbacks: the cost of the instrument and its relative complexity. The price of a 3D sonic anemometer plus the data logging system can easily reach 12 k€ which excludes many practical applications requiring spatially distributed measurements of sensible heat flux such as for instance the study fluxes over heterogeneous surfaces. In addition, the setup of the instrument in the field as well as the post-processing procedure of data require respective expertise.

5.2.5 Experimental Setup

The validation experiment was carried out in summer 2015 in the western part of Switzerland between the cities of Geneva and Lausanne (Figure 5.6). The chosen region is a rural area mainly covered with agricultural fields and forests except for a commercial zone located to the north of it. The area is bordered to the south by Lake Geneva. This land cover heterogeneity allows us to define three different sites with distinct surface types: a large gravel-covered rooftop, a flat, wide meadow and a large body of water. The three sites are located within only 2 kilometers and experienced approximately the same local meteorological conditions but different microscale meteorology induced by the land cover. The experimental sites presented in Figure 5.7 had the following setup:

- A low-cost sensible heat flux sensor connected to a Sensorscope station (Barrenetxea et al. [2008b]) being part of a WSN
- A Campbell Scientific 3D sonic anemometer (CSAT3) (Campbell Scientific, Inc. [2017]) connected to a Campbell Scientific CR5000 data logger
- A second low-cost sensible heat flux sensor connected to the same CR5000 data logger

The low-cost sensible heat flux sensors and the sonic anemometer are collocated within 10 cm (Figure 5.7d) and are assumed to sample the same air volume representative of the local atmospheric processes. The instrument height is important for the computation based on the FV method (see Equation 5.2) and sensors were set up at 2 m above ground for the meadow and gravel sites and 3.2 m over the water surface. In addition, the instruments were oriented in the main wind direction to minimize the disturbances induced by the station mast. All sites were chosen with a minimum fetch of 50 m, in case of the meadow and the lake the fetch was much larger. The station is powered by a solar panel and is totally autonomous. The sonic anemometer measures the wind vector in the 3 dimensions along with the air temperature at a frequency of 20 Hz. The low-cost sensible heat flux sensor only measures the temperature and its standard deviation at 20 Hz. The data are processed "on the fly" by the embedded micro-processor and transferred once per minute as mean values to the data logger. The sensible heat flux is then computed based on these temperature estimates using the FV method.

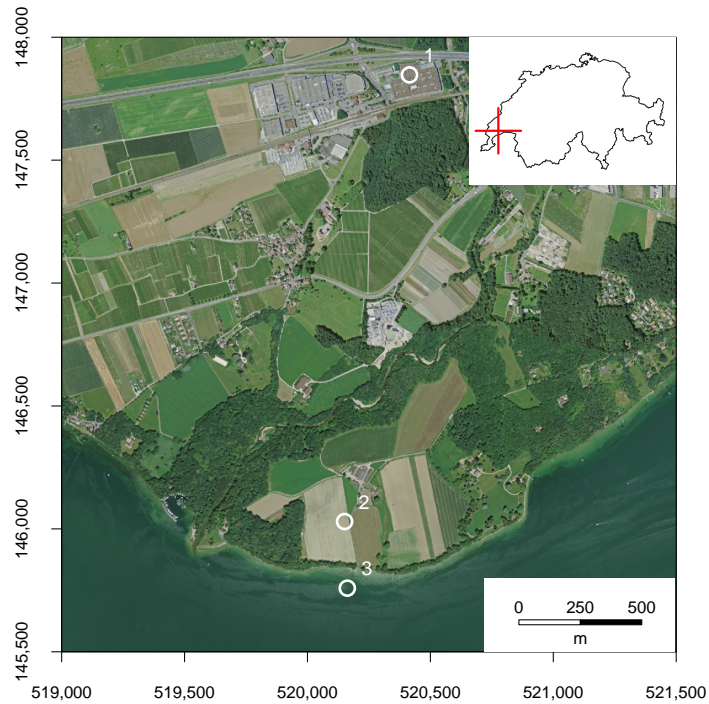


Figure 5.6 – General situation of the validation experiment in the Lake Geneva region. The three sites are indicated with a white circle: 1) flat gravel-covered rooftop 2) wide meadow and 3) water surface of the lake. Coordinates are given in the CH1903 geodetic datum. Orthoimage reproduced with permission from swisstopo (JA110138).

5.3 Results

5.3.1 Comparison of temperature measurements

As a preliminary validation, temperature measurements from the SHF sensor are compared to the reference temperature measurements from the sonic anemometer. Results presented in this section are based on raw data: no post processing has been performed except removing outliers due to data logger failure. Figure 5.8 presents the scatter plots of the mean temperature averaged over 1 minute (the reference is on the x-axis and the TC sensor on y-axis) at the three different sites. Over the gravel surface, the agreement between the two sensors is very good indicated by the high coefficient of determination ($R^2 = 0.98$). Data obtained over the meadow show slightly more spread around the regression line and a few outliers, but the agreement remains good ($R^2 = 0.96$). Over the lake, the number of available points for the comparison is smaller as unfavorable conditions induced some loss of data. However, the resulting correlation is still good ($R^2 = 0.97$). It is worth noting that all three point clouds are not exactly aligned on the diagonal indicating a negative (and almost constant) bias of $\sim 5^\circ \text{C}$ between the two instruments. This was expected, as TCs are known to be very sensitive but not necessarily very accurate in absolute terms. This is however not a problem as the bias is more or less constant and can therefore easily be corrected.

When comparing temperature standard deviations over 1 minute measured by the reference



Figure 5.7 – Setup of the validation experiment carried out in summer 2015: a) station over a large, flat, gravel-covered rooftop b) station over a wide meadow c) station over the lake surface, and d) close-up of the 3D sonic anemometer and the two collocated low-cost sensible heat flux sensors.

and the TC (Figure 5.9), the scatter is substantially larger than for the mean temperature. This is not surprising as the thermocouple is less sensitive to high frequency fluctuations in temperature (mainly due to thermal inertia) compared to the sonic anemometer. Moreover, significant differences between the three sites are noticeable. Over the gravel surface, the coefficient of determination is high ($R^2 = 0.84$) and data show a very good agreement. On the grass field, the spread is slightly larger even though the match remains good ($R^2 = 0.74$). In these two first cases, the slope of the regression curve does not indicate any bias between the sonic anemometer and the SHF sensor. Over the water surface, temperature standard deviations are not only much smaller but the agreement between sensors is also much lower ($R^2 = 0.47$). Several reasons can explain this misalignment. First, the water has a large thermal inertia dampening the air temperature fluctuations; thus the air temperature variance is expected to be smaller than over grass and gravel surfaces. In addition, the latent heat flux is

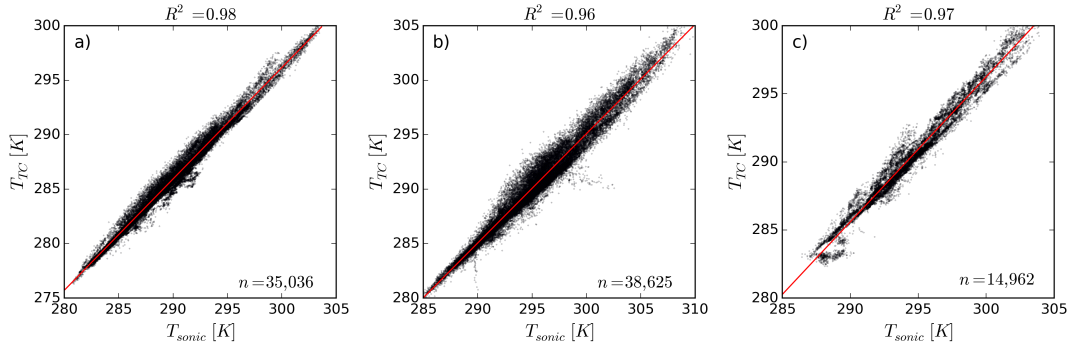


Figure 5.8 – Scatter plots of 1-minute mean temperatures measured with the SHF sensor (T_{TC}) and the 3D sonic anemometer (T_{sonic}) over three different surfaces: a) flat gravel-covered rooftop b) wide flat meadow and c) lake surface. Regression lines are shown in red.

more important as water supply is not a limiting factor (compared to a cropland or a built surface). Overall, the agreement between the temperature data from the sonic anemometer and the SHF sensor, i.e. the thermocouple, is very satisfactory. For computing the sensible heat flux, the temperature and standard deviation are aggregated over 30 minutes period and then the errors observed above are noticeably reduced.

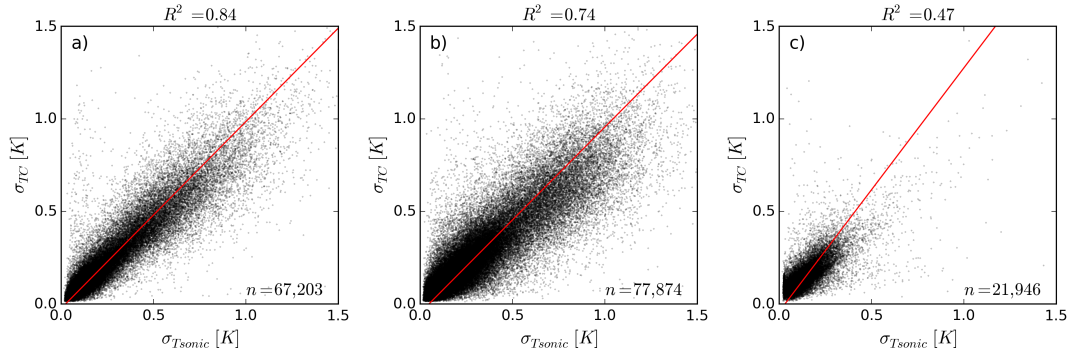


Figure 5.9 – Scatter plots of temperature standard deviation (over 1 minute) measured with the SHF sensor (σ_{TC}) and the 3D sonic anemometer (σ_{Tsonic}) over three different surface types: a) gravel b) grass and c) water. Regression lines are shown in red.

The comparison of two equal thermocouples gives confidence in the robustness of temperature estimates and their variance. The results aggregated over 30 minutes (Figure D.1 in the Appendix) show a very good agreement for the temperature with $R^2 = 0.99$ over the three surfaces. Nevertheless, some outliers are visible outside of the regression line: they are due to electronic problems encountered by the data logger. As before, the constant bias between the two sensors can be corrected by calibrating them with a reliable reference. The scatter plots of the standard deviation show slightly more spread even though the coefficients of determination remain relatively high ($R^2 = 0.89$, $R^2 = 0.80$ and $R^2 = 0.69$ for gravel, grass and water, respectively, Figure D.2 in the Appendix). In particular, this shows the difficulty of measuring accurately the standard deviation of air temperature and obtaining similar results

even with the exact same sensor located only 10 centimeters from each other.

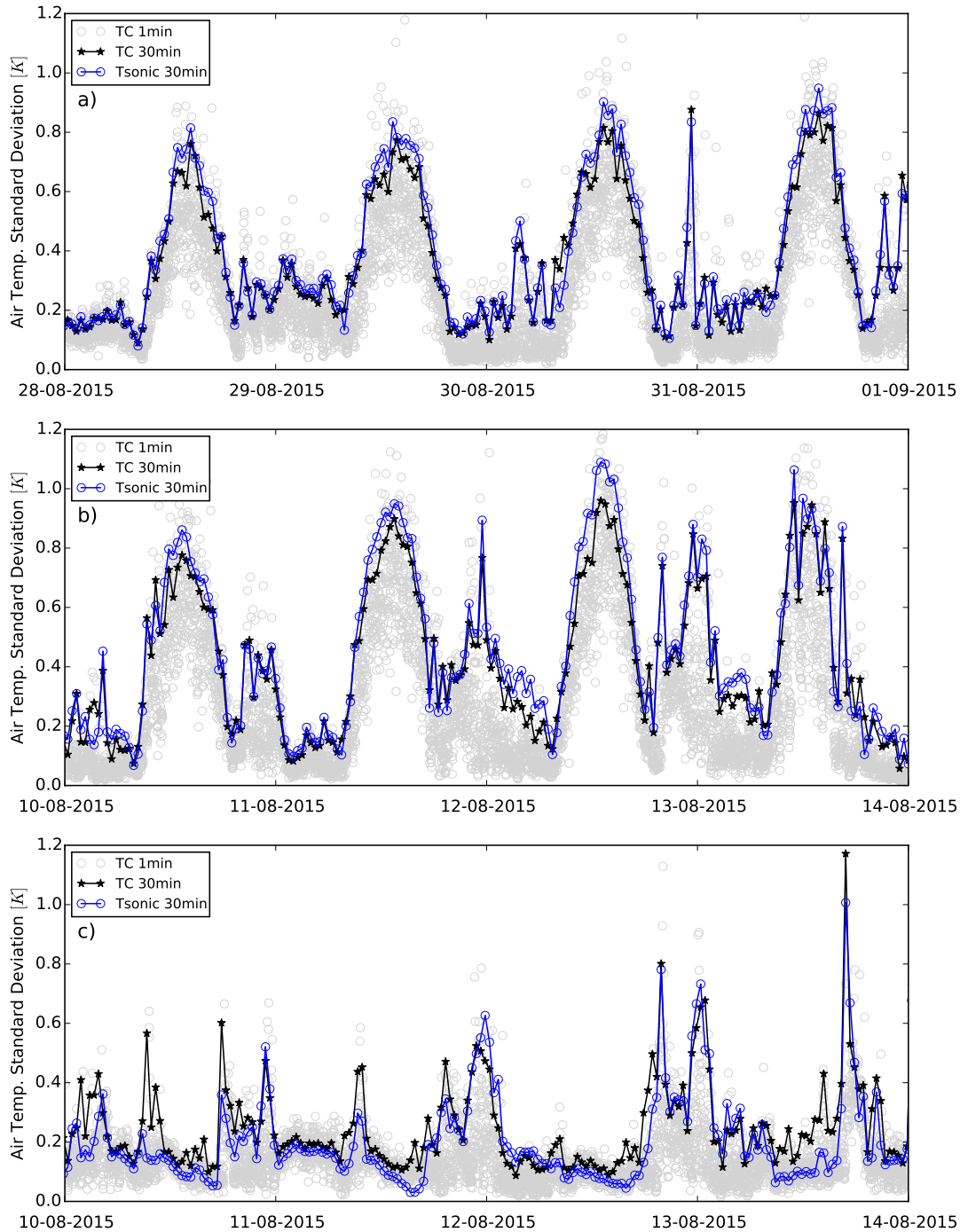


Figure 5.10 – Time series of air temperature standard deviations over different surface types: a) gravel b) grass and c) water. Data are aggregated over 30 minutes from the 3D sonic anemometer (in blue) and the SHF sensor (in black). The original 1-min data from the SHF sensor are in light grey.

To compute the SHF with the FV method, the second moment of air temperature is not only the most sensitive term in Equation 5.2, but also the most difficult one to measure accurately. Additionally, as the air temperature fluctuations are not a linear process, the standard deviation over 30 minutes is not equal to the mean of the 1-min standard deviations. The method used to reconstruct the temperature variance is presented in Appendix D.1. The aggregated results show a very close agreement with the standard deviation from the sonic anemometer (Figure 5.10). The daily cycles are clearly visible over the gravel and the grass surfaces with large values during the day when the surface gets hot and the atmosphere becomes turbulent, and smaller values during the night (with some exceptions). We can notice that the maxima are slightly underestimated by the SHF sensor. As expected, the magnitude in temperature fluctuations is much smaller over the lake and the daily cycle is somehow inverted with maxima around midnight. These night-time fluctuations could be due to thermally-driven winds (lake/land breeze) that are triggered during summer by the local topography and the difference in heat capacity between the land and the water.

Overall, the comparisons between the new SHF sensor and the sonic anemometer serve as a validation of the temperature sensor not only in real-world but also under diverse conditions and confirm the suitability of the chosen TC for the low-cost SHF sensor.

5.3.2 Comparison of sensible heat flux

The eddy covariance method requires defining a time-averaging interval. We choose a 30 minutes period which is relatively standard and thus, computed the sensible heat flux with the FV method over the same interval. In order to distinguish the error inherent to the FV method and the ones introduced by the TC sensor, we additionally compute the sensible heat flux using the FV method but with the temperature from the sonic anemometer. The results for the three sites are presented in Figure 5.11. The few gaps in the EC time series are due to winds from the excluded sectors; these data were removed. For the FV method, we define a threshold of -0.15 for the stability parameter ζ . Unfortunately, this constraint removes numerous points even during periods in summer when convection is limited (Figure 5.11). Over the gravel surface, the SHF sensor is performing well compared to the reference: the diurnal cycle is nicely reproduced and the magnitudes of the SHF are comparable. However, one can notice a systematic underestimation of the daily maximum. This issue is less evident when using the temperature from the sonic anemometer indicating a bias from the sensor and not originating from the method. Over grass, the agreement between the FV method and the EC method is very good: especially the daily peaks are well reproduced. Surprisingly, the low-cost sensor detects high SHF values during nighttime that are not measured by the sonic anemometer and highly unlikely at that period of the day. They seem to be linked with local wind phenomena creating turbulent flow. As this is happening during the night (when the SHF should be negative or small), they can be filtered out easily. Over the lake, fluxes are much smaller and the agreement with EC-derived SHF is lower. Measuring the sensible heat flux over a water body is challenging as the latent heat flux is not limited by the water availability (Vercauteren et al. [2009]).

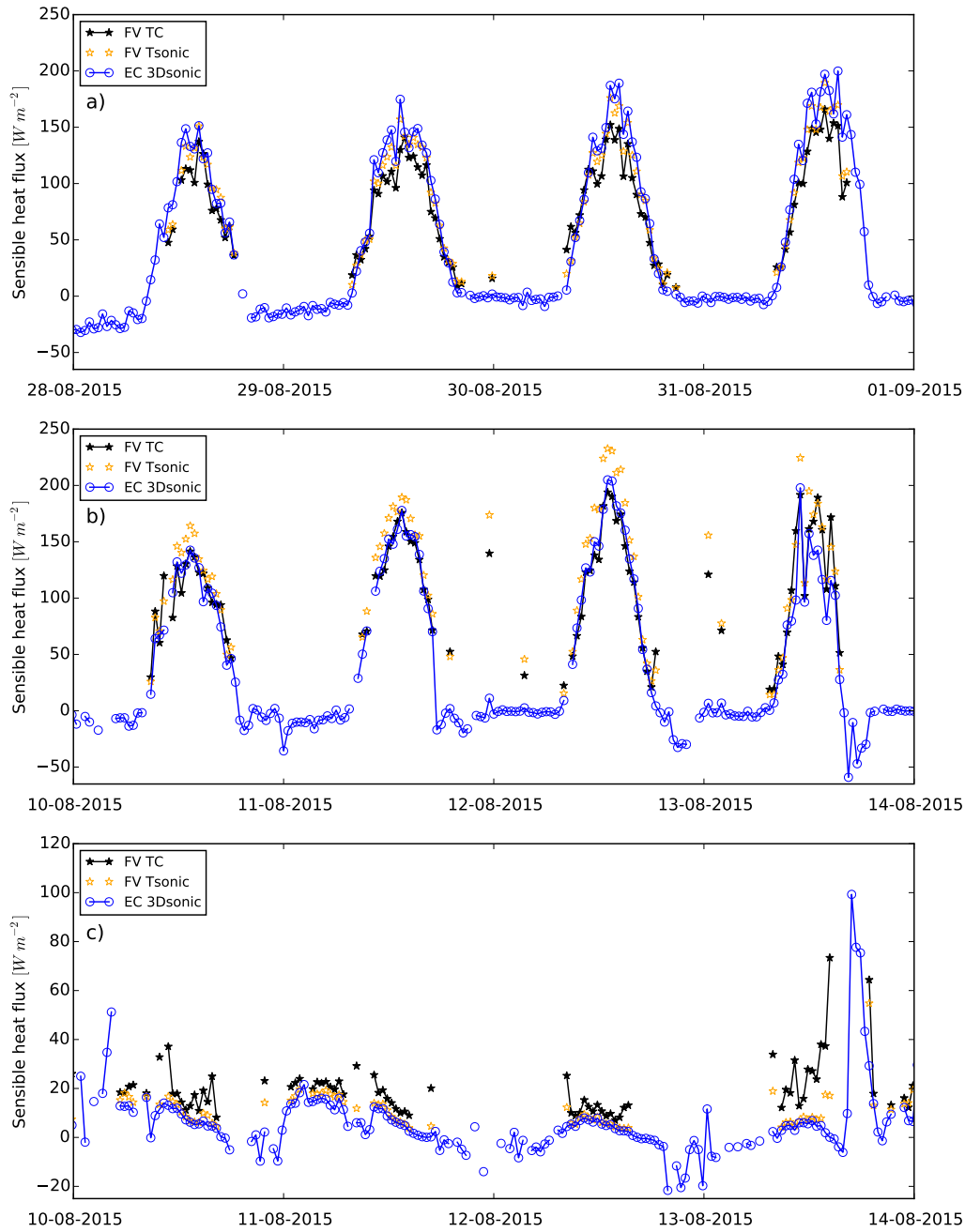


Figure 5.11 – Time series of sensible heat flux over different surface types: a) gravel b) grass and c) water. SHF is computed over 30 minutes with the help of the FV method (in black, using the TC sensor) and the Eddy Covariance (EC) method (in blue, using the 3D sonic anemometer). In orange, the FV method is used based on the temperature estimates given by the sonic anemometer. Note the different scale for SHF in panel c).

Figure 5.12 presents the comparison of SHF computed with the FV method to that from the EC method. Over the gravel surface, the match is very good ($R^2 = 0.94$) between the two sensors even though the negative bias observed previously (Figure 5.11a) is clearly identifiable: the SHF

sensor tends to slightly underestimate the sensible heat flux. Over the grassland, the spread is a bit larger ($R^2 = 0.78$) but no significant bias is visible. The outliers along the y-axis correspond to the ones observed before and during the night (Figure 5.11b). As expected, over the lake, the agreement is relatively low with smaller SHF values and apparent overestimation by the SHF sensor. The results presented in Figure 5.13 compare the EC method and the FV method but using the temperature of the sonic anemometer. In general, these have similar patterns to the results in Figure 5.12 (negative bias over the gravel, outliers during the night over the grass and large spread over the lake). These problems are then inherent to the FV method. On the other hand, the coefficients of determination are lightly higher indicating a better assessment of the mean air temperature and standard deviation by the EC instrumentation.

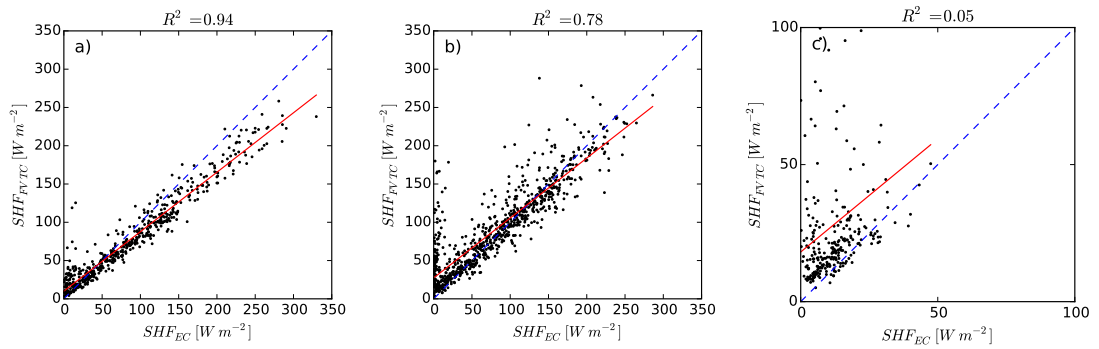


Figure 5.12 – Comparison of sensible heat flux computed with the EC method (SHF_{EC}) and the FV method using the TC temperature (SHF_{FVTC}) over three different surfaces: a) gravel b) grass and c) water. The 1:1 line is shown in blue. Note the different scale in c).

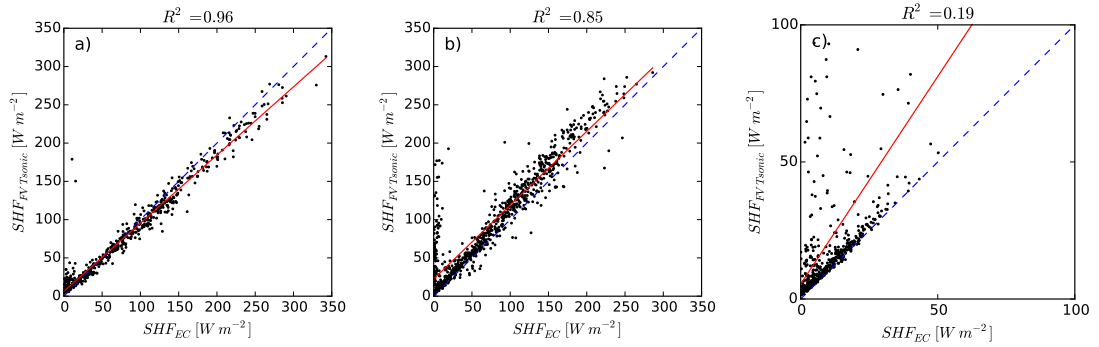


Figure 5.13 – Comparison of sensible heat flux computed with the EC method (SHF_{EC}) and the FV method using the sonic anemometer temperature ($SHF_{FVTsonic}$) over three different surfaces: a) gravel b) grass and c) water. The 1:1 line is shown in blue. Note the different scale in c).

The quantitative performance of the new low-cost sensor compared to the eddy covariance method are presented in Table 5.3. The errors are the smallest over the gravel surface and are quite homogeneous. The bias is negative but relatively small. Interestingly, the errors are becoming much smaller when using the temperature from the sonic anemometer ($SHF_{FVTsonic}$)

indicating that the TC is not able to capture the full signal due to slow response time. Over the grass, the errors are slightly larger but most importantly the generally good performance is strongly penalized by the outliers (indicated by the large difference between the RMSE and the MAE along with the positive bias). On the other hand, the temperature measured by the sonic anemometer doesn't change drastically the performances which means that the SHF sensor is performing well under these conditions. Over the lake, errors are larger acknowledging that the magnitude of the SHF is much smaller. Excluding the site above the water, the errors or the SHF estimates are on the order of 10% to 20% which we consider acceptable for this kind of sensor and actually very promising for potential applications in WSN.

Table 5.3 – Performance of the new low-cost sensible heat flux sensor (root mean square error, mean absolute error, bias) compared to the reference sensor (3D sonic anemometer) over gravel, grass and water surfaces.

		RMSE [Wm^{-2}]	MAE [Wm^{-2}]	Bias [Wm^{-2}]
Gravel	$SHF_{FV TC}$	23.43	17.50	-9.90
	$SHF_{FV Tsonic}$	14.97	9.00	-3.17
Grass	$SHF_{FV TC}$	31.59	19.94	9.04
	$SHF_{FV Tsonic}$	32.20	21.53	19.46
Lake	$SHF_{FV TC}$	35.03	16.77	15.98
	$SHF_{FV Tsonic}$	31.47	11.01	10.95

Overall, the new low-cost sensible heat flux sensor shows promising results. The sensor itself is sensitive enough to measure fast temperature changes. The thermal inertia is negligible and the power consumption remains acceptable. The cost of the sensor, which was one of the motivations of this project, is clearly in line with our a-priori target of <100 €. In addition, the experiments carried out in real outdoor conditions has proved the robustness of the fine-wire thermocouple. Even though sensible heat flux is generally difficult to measure accurately, the new low-cost sensor performs well when compared to the reference sensor. Only over the water surface the discrepancy is larger. Nevertheless, this site was chosen to test the sensor over a variety of surface types, knowing that the sensible heat flux over the lake surface would be smaller than at the other sites. The good performance above the grassland motivates the application of such sensors for spatially distributed SHF measurements over heterogeneous terrain, or in agriculture to locally manage fields during the growing season.

5.4 Conclusions and Outlook

In the framework of the EU FP7 *WeSenseIt* project, a Citizen Observatory of water, the objective was to develop a low-cost sensible heat flux (SHF) sensor. Based on the flux variance (FV) method, a fast response temperature sensor measures the air temperature and its fluctuations at high frequency and calculates the SHF after on-board signal processing. A first challenge during the development phase consisted in finding a suitable thermometer: sensitive and

fast enough, but at the same time robust, inexpensive, and with a low power consumption. Several candidate sensors were available with different technical specifications. A series of tests was performed for identifying the most suitable sensor for this specific application and the final choice fell on a simple fine wire type E thermocouple satisfying most of the imposed constraints. This sensing element was interfaced with a custom-made programmable printed circuit board including a micro-controller which provides several communication protocols for connection to a data logger. The SHF sensor was tested and validated during a field experiment at three different sites with distinct land covers: (1) a large, flat gravel-covered rooftop, (2) a wide grassland and (3) a large open water surface. During this field campaign, the new sensors were compared to a reference instrument, a 3D sonic anemometer, and at the same time, sensors were integrated in a small wireless sensor network (WSN).

The following list presents the principal findings and conclusions:

- Overall, the new SHF produced results in reasonable, in most cases good agreement with the SHF obtained from the sonic anemometers applying the EC method.
- The response time of the thermocouple used for the temperature fluctuation measurements featured a sufficient response time for measured temperature variances comparable to the reference instrument, i.e. the sonic anemometer.
- Measurements at the gravel surface and grassland sites were in better agreement with the reference measurements than at the lake site, most likely due to the larger magnitude of the fluxes at the previous sites and as a result of super-imposed effects of evaporating moisture from the water surface.
- Ignoring some periods at the lake site with challenging conditions, the overall error of the FV method using the SHF sensor over the 11-weeks interval of available measurements is on the order of 10-20% which we judge as reasonable and acceptable for this sensor and method.
- The six deployed SHF sensor fine wire TCs survived at all sites and did not get damaged or destroyed during the whole period of deployment, giving confidence in the durability of the normally fragile sensing element.
- The SHF was successfully interfaced and connected to several data logging platforms using the SDI-12 communication protocol: (1) Campbell Scientific data loggers, (2) Sensorscope WSN nodes, and (3) Arduino UNO boards including an SD card logging shield and a real-time clock.
- The SHF sensor has demonstrated its suitability to be used and integrated in WSN for spatially distributed energy balance studies and environmental monitoring, and is judged as a useful and relevant component in innovative and low-cost environmental sensing of reasonable quality.

As an outlook we suggest some potential developments not only to improve the sensible heat flux estimate but also to extend its utility. A further development of the SHF sensor could be the implementation of the Surface Renewal (SR) method as an alternative way of computing the sensible heat flux. This method assumes that ramp-like temperature profiles observed at the surface are linked to coherent structures of the flow in the surface layer and thus are used as a proxy for air mass movement (Kyaw Tha Paw U et al. [1995], Snyder et al. [1996]). Until recently, a major inconvenience of the SR method was the need for a parameter calibration against a reference measurement (in general the eddy covariance method). However, Shapland et al. [2014] showed that a calibration could be omitted if the frequency response of the temperature sensor in use (in our case the thermocouple) was correctly compensated. Castellví and Snyder [2009] also showed that, under certain conditions, the combination of the SR method and the dissipation method requires no calibration. The implementation of the SR method would bring several advantages to the SHF sensor: first of all, it would reduce the constraints on its applicability in time. In fact, the SR method is not limited to convective conditions and would extend the application of the sensor to periods of negative (downward) sensible heat fluxes for instance at nighttime and/or during the cold seasons which is not possible with the FV approach. Secondly, the combination of both methods (i.e. FV and SR) could be used as a reliability indicator for the sensible heat flux. Finally, the SR method can be applied above a canopy (Spano et al. [2000], Katul et al. [1996], Poblote-Echeverría et al. [2014]) which is particularly interesting for agriculture or viticulture.

A second path to make the SHF sensor useful and attractive for users is the estimation of the latent heat flux (LHF) based on the SHF measurements. The LHF and the related evapo-(transpi)ration is rarely measured outside the scientific community, but is of major interest for agronomists, practitioners managing crops and other decision-makers in the environmental sector. As mentioned in Section 5.1, the LHF could be computed as a residual of the energy balance (see Figure 5.1 and Equation 5.1). This requires only a net radiometer and a soil heat flux plate as additional collocated sensors. Then, the computation of the residual LHF is straightforward and easily manageable on the data logger used. Given that many sites are already equipped with a net radiometer and a soil heat flux plate, addition of a SHF sensor would allow for LHF estimates at minimal cost. Monitoring the micro-meteorology at the field-scale has already proven its utility for example to predict frost events (Watteyne et al. [2016]) and to protect sensitive crops. In addition, the development of the Internet of things (IoT), of which WSNs are a good example, has drastically reduced the cost of data logging systems and sensor deployments in general (Barrenetxea et al. [2008a], Simoni et al. [2011], Malek et al. [2017]).

6 Conclusions and Outlook

This dissertation focuses on snow and hydrological processes taking place in Alpine environments. Due to their complexity, many questions related to the mass and energy balance of the snowpack remain nowadays open. Moreover, the high variability of these processes in space and time add further complexity. By combining experimental data and advanced numerical models, the goal of this thesis is to make a small contribution to our understanding of snowmelt dynamics. The chosen playground is the Dischma valley in the Swiss Alps.

In Chapter 2, we examine the influence of snowmelt on the hydrological response of the Dischma river during the water year 2014-2015. Based on recent advances in *Alpine3D*, we examine how snow distributions and liquid water transport within the snowpack influence runoff dynamics. By combining these results with observations, we demonstrate the added value of a more realistic snow distribution at the onset of the melt season. At the site scale, snowpack runoff is well simulated when the mass balance errors are corrected. At the subbasin scale, a more heterogeneous snowpack leads to a more rapid runoff pulse originating in the shallower areas while an extended melting period is caused by snowmelt from deeper areas. This is a marked improvement over results obtained using a traditional precipitation interpolation method. Hydrological response is also improved by the more realistic snowpack, even though calibration processes smoothen out the differences. The added value of a more complex liquid water transport scheme is obvious at the site scale but decreases at larger scales. Our results highlight not only the importance but also the difficulty of getting a realistic snowpack distribution even in a well-instrumented area. With regard to climate change, the

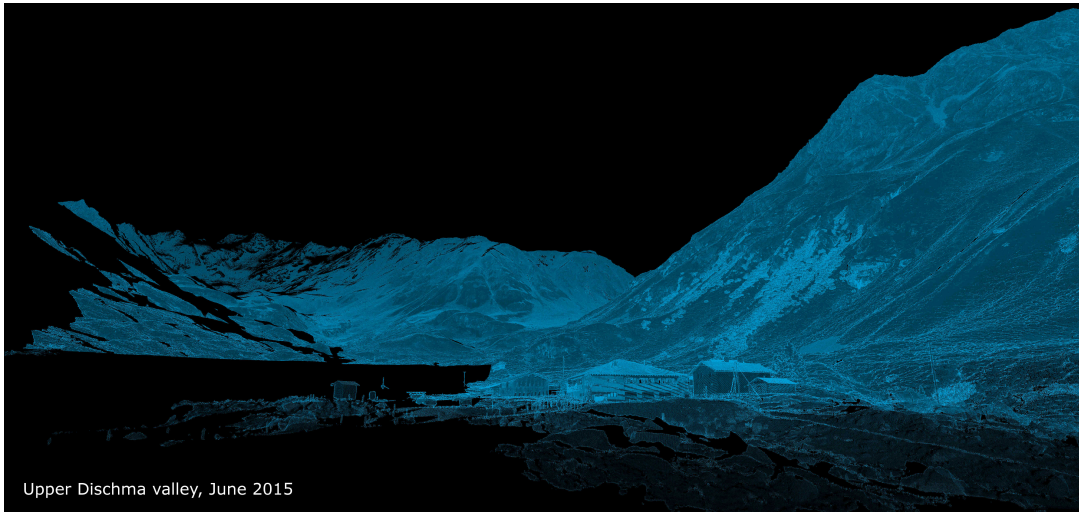
significance of spatial snow variability will be fundamental for snow hydrology, notably in terms of seasonal timing and should be considered in climate impact studies. Our analysis also points out the need of dense automatic monitoring networks for snow and meteorological variables. These data are not only required to force the model, but also to validate its output and improve the understanding of the system. Finally, the misrepresentation of some small-scale processes indicates that the current model resolution is not fine enough to capture the entire spectra of snow variability. These considerations tend toward the development of more physical models that require only limited calibration and represent accurately the different spatial scales.

Based on the same model setup, we examine in Chapter 3 how the energy balance of the snowpack is evolving throughout the year and which energy fluxes are driving the snow ablation at a fine spatial resolution. At the beginning of the melt season, the energy is the limiting factor while later on the snow availability becomes critical. The ablation is mainly driven by three fluxes: the net shortwave and longwave radiation along with the sensible heat flux. As expected, the solar radiation is the largest energy input during the summer. We also assess the robustness of the model chain *Alpine3D-StreamFlow* over the water years 2002-2016. The model reproduces accurately the snowpack evolution as well as the discharge in the river. Nowadays, physically based models are mainly limited to the academic world. However, increasing computational resources should allow for a wider use in the future. In combination with simpler models, one can easily imagine their use in operational forecasting systems. A coupling with an atmospheric modeling system could also be a way of improving snow simulations. This would allow a more accurate representation of mass and energy exchanges between the atmosphere and the surface.

In Chapter 4, we investigate the spatio-temporal variability of the snowpack with the help of a long range TLS. Thanks to this remote sensing technique, we obtain high-resolution snow depth maps throughout the ablation season (mid-April to mid-June). By subtracting consecutive observations, we can analyze the snowmelt dynamics at the hillslope scale. The histograms of the ablation rate shows a bi-modal distribution during most of the season. In addition, their evolution in time is opposite: the first mode tends to lower ablation values while the second one is increasing. We propose an explanation based on their associated limiting factors: the ablation of a shallow snow cover is rapidly limited by the available mass as the snow covered area is decreasing. On the other hand, a deep snow accumulation remains limited by the available energy as the snow cover area is more or less constant. To be validated, this hypothesis will need further investigation. However, such data set is very valuable to better understand the ablation dynamics at the hillslope scale and point scale. Unfortunately, these data remain limited to research catchment. However, the development of airborne and spaceborne LiDAR systems could provide, in a near future, basin-wide snow depth maps over much larger areas. As seen in the first chapter, the assimilation of these data in a model improves significantly the results. Such combination could be a significant step forward in snow hydrology.

In Chapter 5, we present the development a low-cost sensible heat flux sensor based on the

flux variance method, which only requires high frequency air temperature measurements. While it has a few limitations, the instrument is interesting for low-cost and power-limited wireless sensor networks (WSN). These have the potential of providing sensible heat flux over the domain of a much denser network both resolving spatial variability and improving overall representativeness. The applicability of the flux variance method is explored in a field experiment where the low-cost sensors are compared to reference instruments. We evaluate the performance and limitations of these sensors as well as the method itself with respect to the standard sensible heat flux calculations. Through the experiment carried out over different surface types (gravel, grass, water), we demonstrate the added-value of such a sensor. In combination with a net radiometer, the instrument could provide estimates of latent heat flux, which is rarely measured despite its significance in the surface energy balance. Since a few years, the development of low-cost sensor and data logging system opens up new perspective in environmental monitoring by providing denser observational networks. Additionally, thanks to the Internet of Things, these data can be transmitted in real-time and then, be useful for a wider community.



Upper Dischma valley, June 2015

Nothing is easy!
— Dr V. Sharma

A Slope-Scale Snowmelt and Catchment Response

This appendix presents the Supporting Information published along with the article presented in Chapter 2 and published in *Water Resources Research*:

Brauchli T., Trujillo E., Huwald H., Lehning M., 2017: Influence of Slope-Scale Snowmelt on Catchment Response Simulated With the Alpine3D Model, *Water Resources Research*, **53**, 10723-10739. doi:10.1002/2017WR021278

A.1 Supporting Information

The following figures and table are provided to illustrate more in detail the main ideas presented in the paper. They are not compulsory to understand the main messages but provide a nice in-depth analysis of the snowmelt dynamics of the river basin.

Appendix A. Slope-Scale Snowmelt and Catchment Response

Table A.1 – Statistics of snow distributions at peak accumulation (April 15, 2015) for the original ADS data (spatial resolution: 2 m x 2 m), the aggregated data (grid size: 100 m) assimilated in this study and the different model configurations.

	Original ADS data (2 m)	Aggregated ADS data (100 m)	Ref-BK	Scal-BK	Ref-RE	Scal-RE
Mean [m]	1.42	1.42	1.56	1.55	1.54	1.53
Standard deviation [m]	1.00	0.71	0.31	0.72	0.32	0.73
Coefficient of variation [-]	0.70	0.50	0.20	0.46	0.21	0.48
Skewness	1.06	0.63	-0.99	0.34	-0.98	0.31
IQR [m]	1.31	0.93	0.34	0.93	0.35	0.97

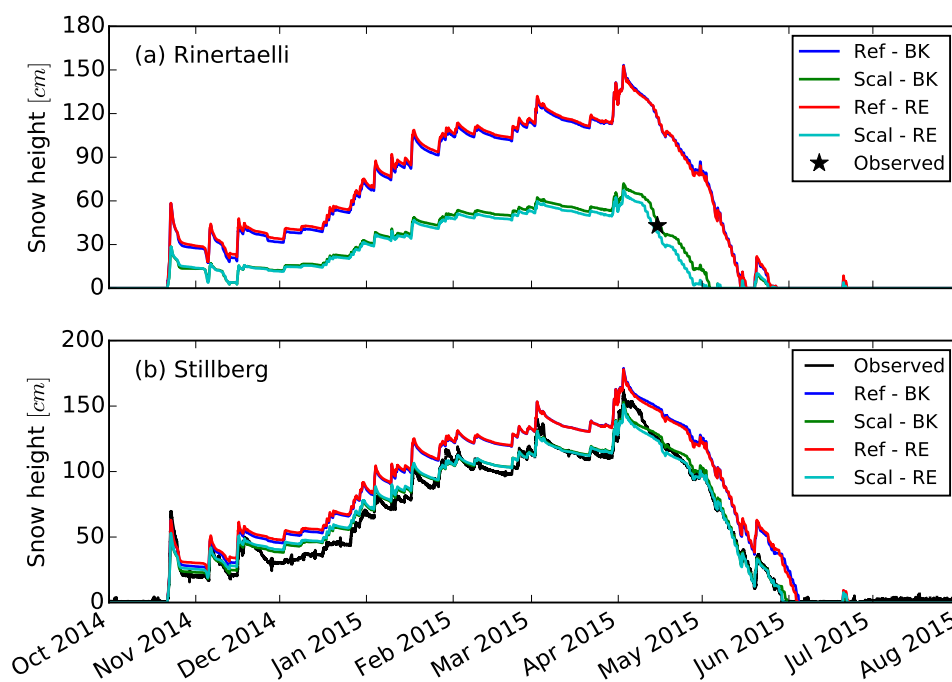


Figure A.1 – Comparison of the snow height at Rinertaelli (a) and Stillberg (b) for the four model configurations: reference interpolation and bucket scheme (REF - BK), scaling method and bucket scheme (Scal - BK), reference interpolation and Richards Equation (Ref - RE), scaling method and Richards Equation (Scal - RE). The one-time snow depth measurement in Rinertaelli comes from the ADS dataset. The continuous measurement in Stillberg comes from the *IMIS* station.

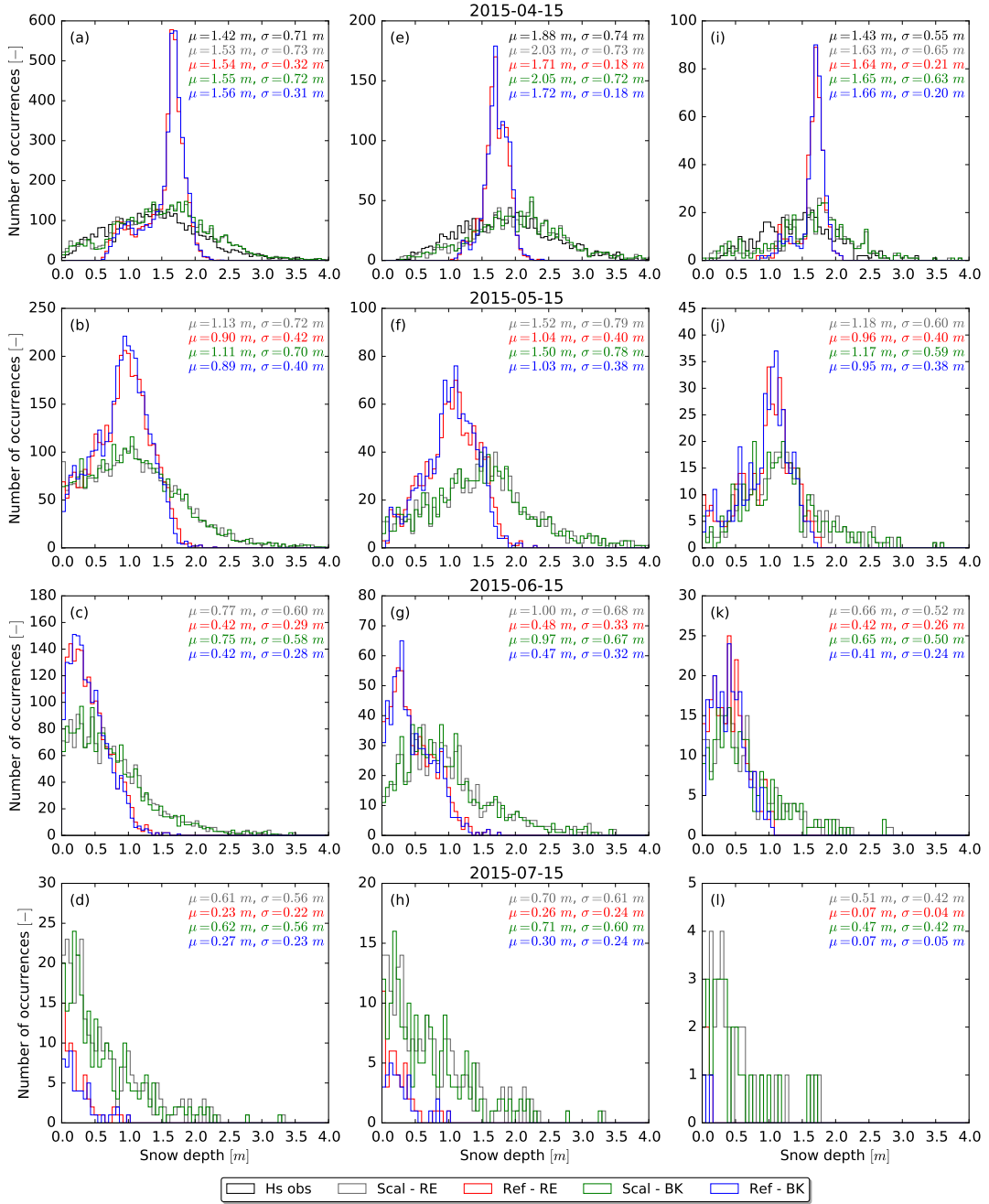


Figure A.2 – Histograms of snow depth distributions throughout the melt season for the different simulations (see label) and observations (in black) over the entire Dischma basin on the left (a, b, c, d), the headwaters sub-catchment in the middle (e, f, g, h) and the Rinertaelli sub-basin on the right (i, j, k, l). The mean snow depth μ and standard deviation σ are indicated on each histograms.

Appendix A. Slope-Scale Snowmelt and Catchment Response

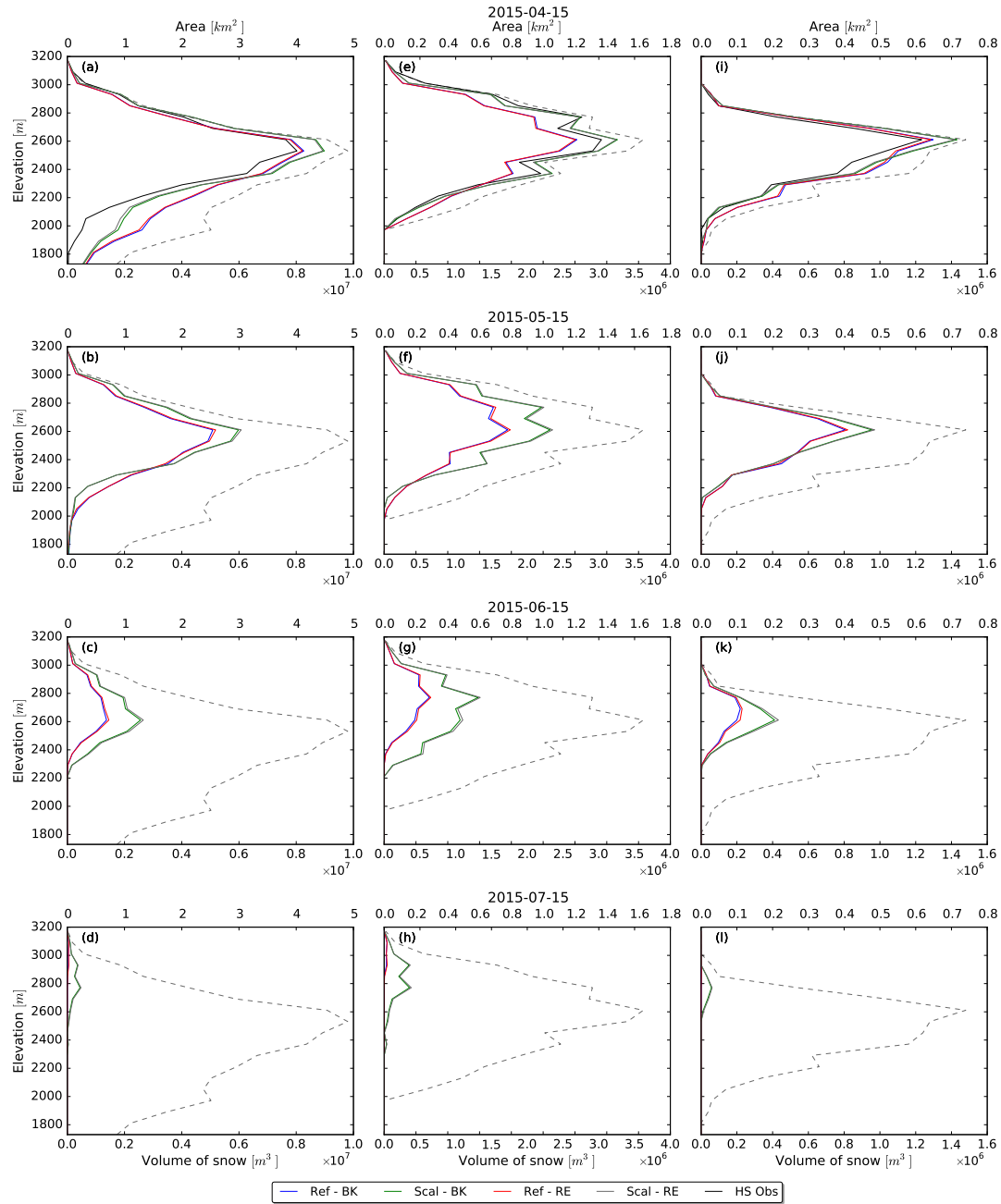


Figure A.3 – Snow distribution as a function of elevation throughout the melt season for the entire Dischma basin on the left, the headwaters sub-basin in the middle, and the Rinertaelli sub-basin on the right. The dashed grey curve represents the basin area distribution as function of elevation.

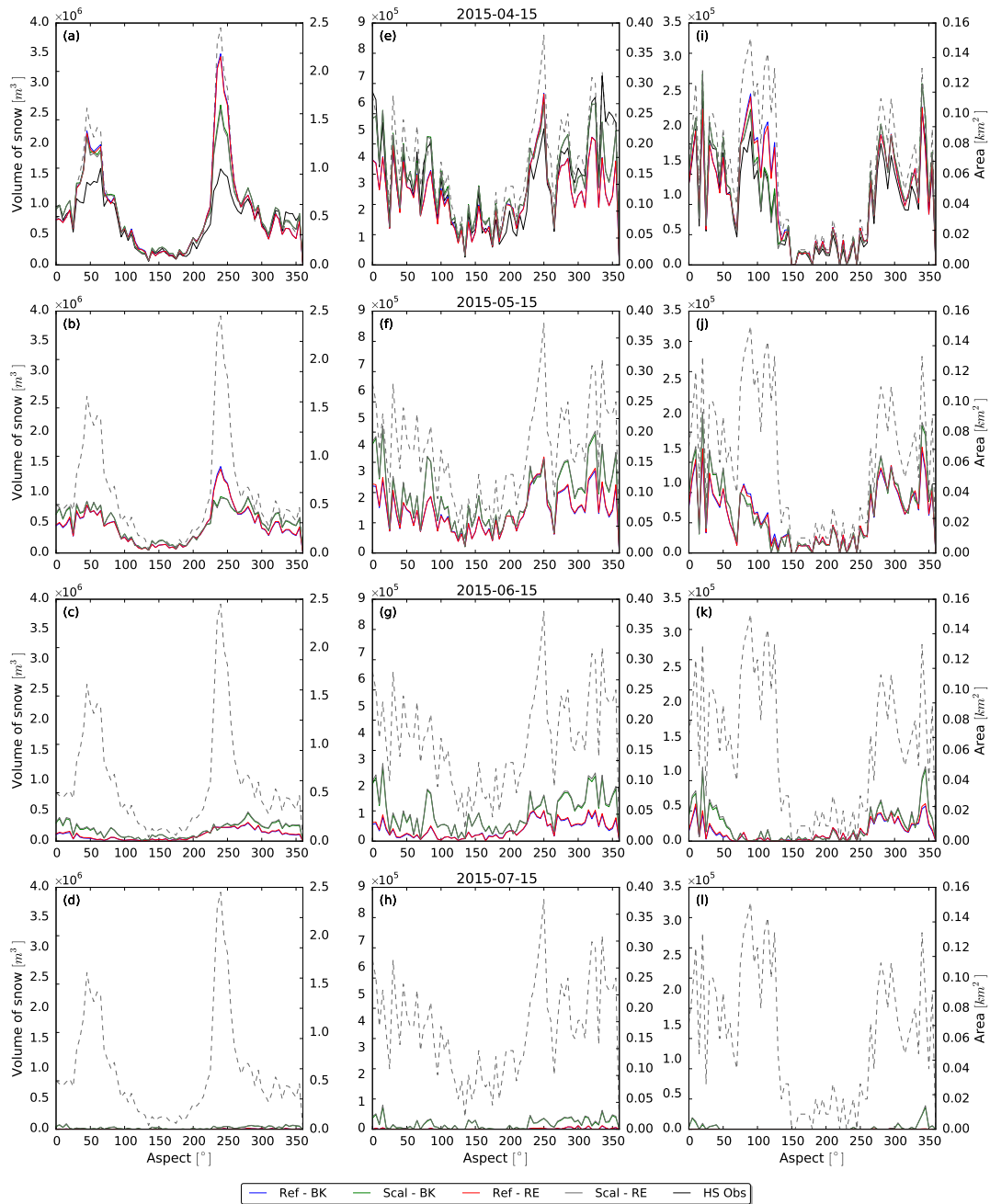


Figure A.4 – Snow distribution as of function of aspect throughout the melt season for the entire Dischma basin on the left, the headwaters sub-catchment in the middle and the Rinertaelli sub-basin on the right. The dashed grey curve represents the basin area distribution as function of aspect.

B Energy partitioning during the snowmelt season

Appendix B. Energy partitioning during the snowmelt season

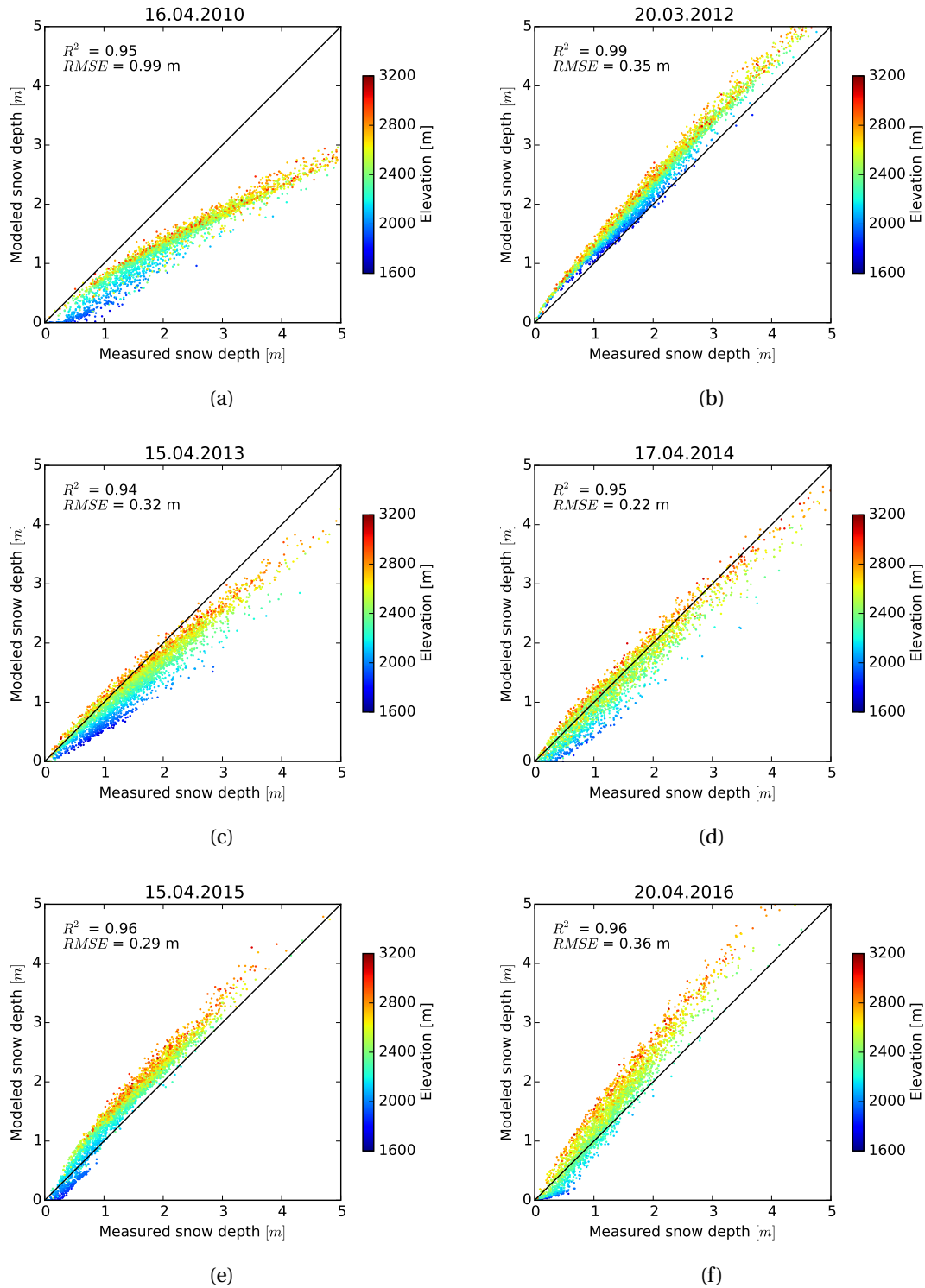


Figure B.1 – Modeled versus measured (ADS) snow depths over the Dischma River basin around peak accumulation for water years 2010 (a) and 2012 to 2016 (b-f). The date of acquisition is indicated on top for every plot. Color indicates the elevation of each grid cell.

C Spatio-temporal variability of snowmelt

C.1 Post-processing procedure of the TLS data

The general procedure used in this study to post-process the TLS data is explained in the following paragraphs.

C.1.1 Correction of the inclination errors

During a scan, the TLS is subject to small movements of the tripod (snow settling, soft ground or wind). Two inclinometers are measuring continuously the roll and pitch angles of the instrument. Figure C.1 presents as an example the output from the inclination sensors during a 35-min scan. As we are scanning slopes at a distance encompassed between 1 km and 3 km, we cannot neglect these errors and have to compensate them in time. This is complicated by the fact that the manufacturer is not providing any ready-to-use tool that can do it and. Additionally, the file format of the raw data is a proprietary format and can only be read with the help of specific libraries. With the help of Pete Gadomski, we finally developed a small

Appendix C. Spatio-temporal variability of snowmelt

home-made tool in C++ that process the raw files and apply the tilt correction.

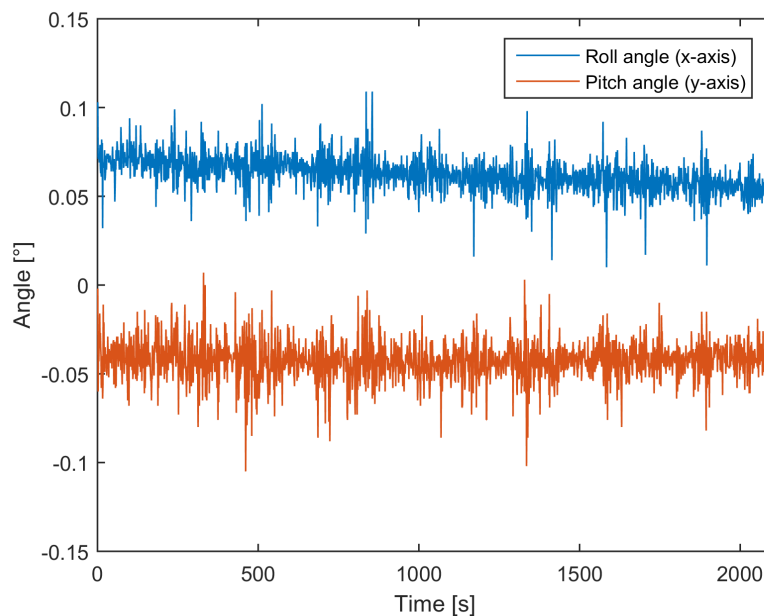


Figure C.1 – Roll and pitch angles measured by the two built-in inclinometers of the VZ-6000 scanner during a 35-min scan.

Mathematically, this operation can be described by a double rotation around the y-axis (pitch) and x-axis (roll) respectively in an Euclidian space. If we define the pitch angle as θ , we have the following rotation matrix:

$$R_y(\theta) = \begin{bmatrix} \cos\theta & 0 & \sin\theta \\ 0 & 1 & 0 \\ -\sin\theta & 0 & \cos\theta \end{bmatrix} \quad (\text{C.1})$$

With the roll angle ϕ , we have:

$$R_x(\phi) = \begin{bmatrix} 1 & 0 & 0 \\ 0 & \cos\phi & -\sin\phi \\ 0 & \sin\phi & \cos\phi \end{bmatrix} \quad (\text{C.2})$$

From the scanner documentation, we know that a point P_{ENU} in a ENU frame (East, North, Up) can be obtained from a point P_{SOCS} in the Scanner's Own Coordinate System by applying

the following transformation:

$$P_{ENU} = R_z(\psi)R_y(\theta)R_x(\phi)P_{SOCS} \quad (C.3)$$

In our case, the yaw correction is null and then $R_z(\psi)$ is equal to the identity matrix. The transformation from one coordinate system to the other is simply the multiplication of the two matrices presented in Equation C.1 and C.2 which is equal to:

$$R(\theta, \phi) = \begin{bmatrix} \cos \theta & \sin \theta \cos \phi & \sin \theta \sin \phi \\ 0 & \cos \phi & -\sin \phi \\ -\sin \theta & \cos \theta \sin \phi & \cos \theta \cos \phi \end{bmatrix} \quad (C.4)$$

For every single scan, the point cloud is post-processed by applying the double rotation presented in Equation C.4 to each triplet. As the tilt angle is changing during the scan, we compute a time-varying roll and pitch angle. In addition, we apply a smoothing of the inclinometer data to filter out the high frequency changes (see Figure C.1) that are considered as noise.

C.1.2 Calculation of azimuth

In order to orientate the scanner with respect to the North, we have to accurately determine the relative position of each reflector around the TLS. Before scanning the snow surface, we perform fine scans of each of these reflectors. As illustrated in Figure C.2a, we obtain from the scanner a three-dimensional point cloud together with the amplitude of the reflection. Given that the reflectors are covered with a high-reflectivity material, we can isolate them by filtering the data based on the amplitude (Figure C.2b). Then, we compute the change in amplitude and define the edge of the reflector where the gradient is the highest (Figure C.2c). Finally, we fit an ellipse on this surface which determine the center of the reflector and thus, its coordinates relatively to the scanner.

We can now combine the reflectors' absolute position (obtained with a GNSS receiver) and their relative position (with respect to the TLS coordinate system). With the help of a geodetic software, we compute the azimuth angle relative to the North. This operation is illustrated in Figure C.3 for the Duerrboden site: the TLS is surrounded by six reflectors. Moreover, the software provides an uncertainty estimate and enables removing erroneous measurements as the system is redundant. This can happen if a reflector has moved from its measured position for an unknown reason.

Appendix C. Spatio-temporal variability of snowmelt

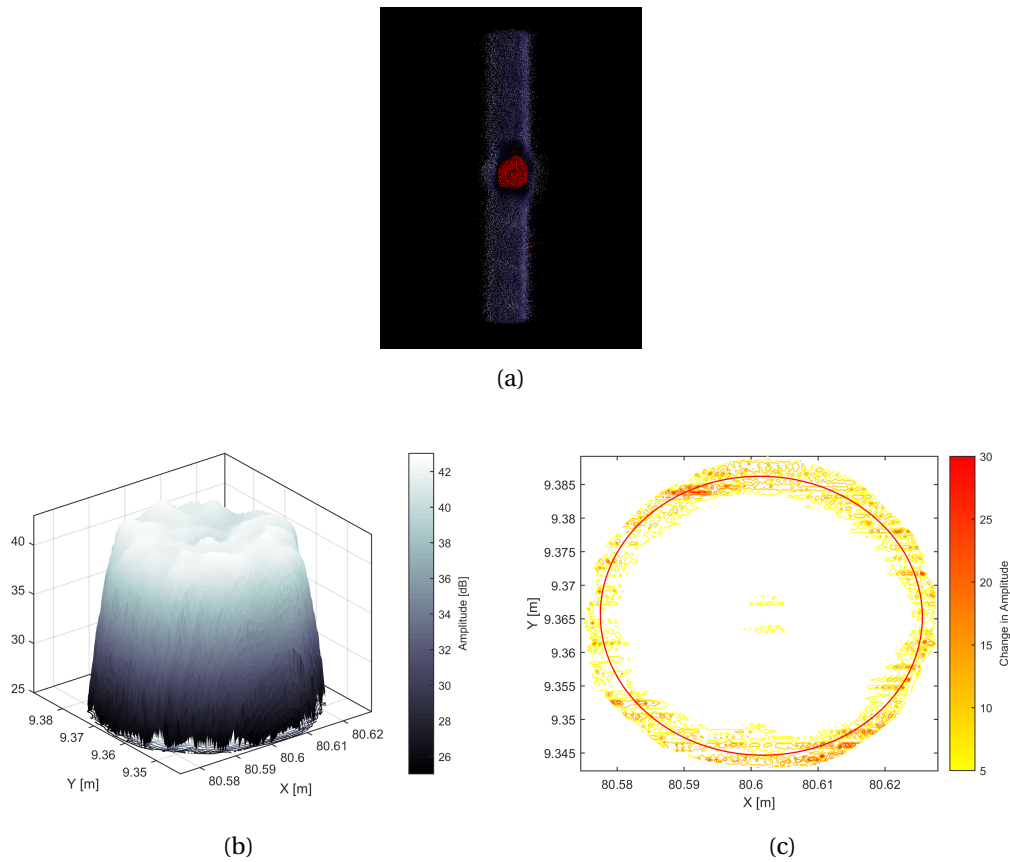


Figure C.2 – Illustration of the post-processing applied to the reflector point cloud. (a) 3D raw data with higher amplitude on the reflector. (b) Determination of the reflector position based on the amplitude. (c) Change in amplitude and fitted ellipse.

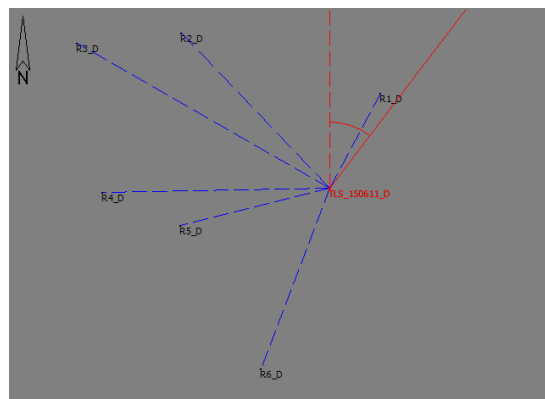


Figure C.3 – Position of the scanner (labeled TLS_150611_D) and the six reflectors (labeled R1_D to R6_D) for the Duerrboden site. The azimuth angle relative to the North is indicated in red.

D A low-cost Sensible Heat Flux sensor for WSN

This appendix presents the Supporting Information published along with the article presented in Chapter 5

D.1 Mathematical derivation of the 30-min variance

In this Appendix, we show how we obtain the 30-min variance values based on 1-min data. This step is necessary as our sensor outputs the mean air temperature and variance over 1 minute interval. Nevertheless, the computation of the sensible heat flux requires these values over a period of 30 minutes. The mean temperature is easily computed as it is a linear quantity. The determination of the variance is slightly more complicated and is detailed below.

By definition, the standard deviation σ of a finite variable x_i measured N times is equal to:

$$\sigma = \sqrt{\frac{1}{N} \sum_{i=1}^N (x_i - \mu)^2} \quad (\text{D.1})$$

with the mean μ defined as:

$$\mu = \frac{1}{N} \sum_{i=1}^N x_i \quad (\text{D.2})$$

Appendix D. A low-cost Sensible Heat Flux sensor for WSN

If we square Equation D.1 and develop the different terms, we have:

$$\begin{aligned}\sigma^2 &= \frac{1}{N} \sum_{i=1}^N (x_i - \mu)^2 \\ &= \frac{1}{N} \left[\sum_{i=1}^N x_i^2 - 2\mu \sum_{i=1}^N x_i + N\mu^2 \right]\end{aligned}\tag{D.3}$$

When we rearrange Equation D.2, we get:

$$\sum_{i=1}^N x_i = N\mu\tag{D.4}$$

We can now substitute Equation D.4 in Equation D.3 and find:

$$\begin{aligned}\sigma^2 &= \frac{1}{N} \left[\sum_{i=1}^N x_i^2 - 2N\mu^2 + N\mu^2 \right] \\ &= \frac{1}{N} \sum_{i=1}^N x_i^2 - \mu^2\end{aligned}\tag{D.5}$$

Assuming that the variance σ^2 and the mean μ in Equation D.5 represent the 30-min variables, we can now substitute the 1-min mean μ_{1min} and variance σ_{1min} that are computed over $n = N/30$ elements:

$$\mu = \frac{1}{30} \sum_{j=1}^{30} \mu_{1min,j}\tag{D.6}$$

$$\sum_{i=1}^N x_i^2 = \sum_{j=1}^{30} \sum_{k=1}^n x_{jk}^2 = \sum_{j=1}^{30} n \left(\sigma_{1min,j}^2 + \mu_{1min,j}^2 \right)\tag{D.7}$$

Finally, we obtain:

$$\sigma^2 = \frac{1}{N} \sum_{j=1}^{30} n \left(\sigma_{1min,j}^2 + \mu_{1min,j}^2 \right) - \left(\frac{1}{30} \sum_{j=1}^{30} \mu_{1min,j} \right)^2\tag{D.8}$$

N.B. We apply a linear detrending on temperature data before computing these quantities.

D.2 Comparison of temperature measurements

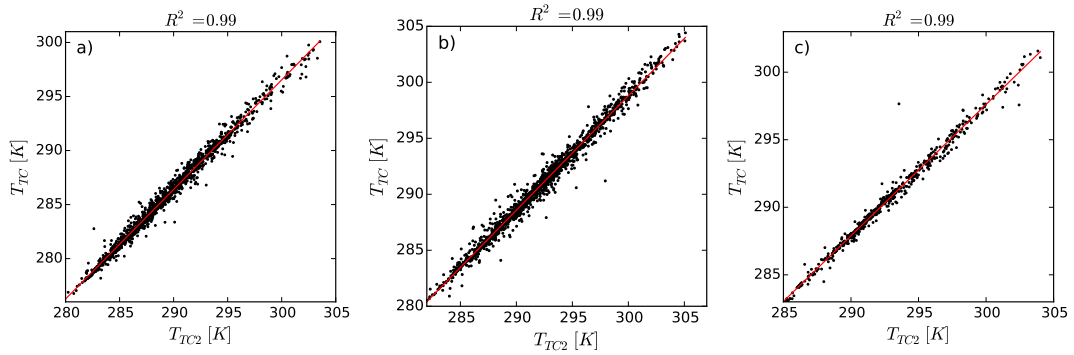


Figure D.1 – Scatter plots of mean temperature (over 30 minutes) measured with two similar TC over the three different surfaces: a) the gravel-covered rooftop, b) the meadow and c) the lake.

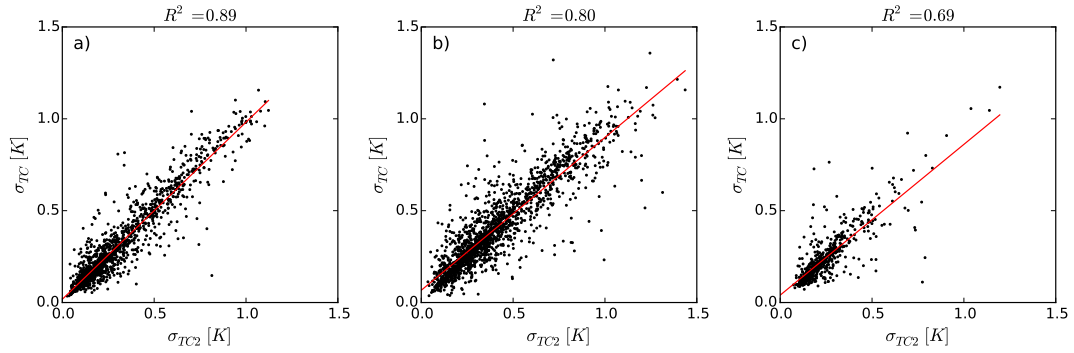


Figure D.2 – Scatter plots of temperature standard deviation (over 30 minutes) measured with two similar TC over the three different surfaces: a) the rooftop, b) the meadow and c) the lake.

Bibliography

- N. Addor, O. Rössler, N. Köplin, M. Huss, R. Weingartner, and J. Seibert. Robust changes and sources of uncertainty in the projected hydrological regimes of Swiss catchments. *Water Resources Research*, 50(10):7541–7562, Oct. 2014. ISSN 1944-7973. doi: 10.1002/2014WR015549. URL <http://onlinelibrary.wiley.com/doi/10.1002/2014WR015549/abstract>.
- J. Albertson, M. Parlange, G. Katul, Chia-Ren Chu, H. Stricker, and S. Tyler. Sensible heat flux from arid regions: a simple flux-variance method. *Water Resources Research*, 31(4):969–973, 1995. ISSN 00431397.
- S. P. Anderton, S. M. White, and B. Alvera. Evaluation of spatial variability in snow water equivalent for a high mountain catchment. *Hydrological Processes*, 18(3):435–453, 2004. ISSN 1099-1085. doi: 10.1002/hyp.1319. URL <http://onlinelibrary.wiley.com/doi/10.1002/hyp.1319/abstract>.
- H. Aschwanden, R. Weingartner, and U. B. A. P. Geographie-Gewässerkunde. *Die Abflussregimes der Schweiz*. Die Abflussregimes der Schweiz. Geographisches Institut der Universität Bern, Abt. Physikalische Geographie-Gewässerkunde, 1985.
- M. Aubinet, T. Vesala, and D. Papale. *Eddy Covariance: A Practical Guide to Measurement and Data Analysis*. Springer, Dordrecht ; New York, 2012 edition, Jan. 2012. ISBN 978-94-007-2350-4.
- S. Baggi and J. Schweizer. Characteristics of wet-snow avalanche activity: 20 years of observations from a high alpine valley (Dischma, Switzerland). *Natural Hazards*, 50(1): 97–108, July 2009. ISSN 0921-030X, 1573-0840. doi: 10.1007/s11069-008-9322-7. URL <https://link.springer.com/article/10.1007/s11069-008-9322-7>.
- D. Baldocchi. Measuring fluxes of trace gases and energy between ecosystems and the atmosphere – the state and future of the eddy covariance method. *Global Change Biology*, 20(12):3600–3609, Dec. 2014. ISSN 1365-2486. doi: 10.1111/gcb.12649. URL <http://onlinelibrary.wiley.com/doi/10.1111/gcb.12649/abstract>.
- R. C. Bales, N. P. Molotch, T. H. Painter, M. D. Dettinger, R. Rice, and J. Dozier. Mountain hydrology of the western United States. *Water Resources Research*, 42(8):W08432, Aug. 2006. ISSN 1944-7973. doi: 10.1029/2005WR004387. URL <http://onlinelibrary.wiley.com/doi/10.1029/2005WR004387/abstract>.

Bibliography

- R. C. Bales, J. W. Hopmans, A. T. O'Geen, M. Meadows, P. C. Hartsough, P. Kirchner, C. T. Hunsaker, and D. Beaudette. Soil Moisture Response to Snowmelt and Rainfall in a Sierra Nevada Mixed-Conifer Forest. *Vadose Zone Journal*, 10(3):786, 2011. ISSN 1539-1663. doi: 10.2136/vzj2011.0001. URL <https://www.soils.org/publications/vzj/abstracts/10/3/786>.
- M. Banzi and M. Shiloh. *Getting started with Arduino: the open source electronics prototyping platform*. Maker Media, Inc., 2014.
- I. Barbeito, M. A. Dawes, C. Rixen, J. Senn, and P. Bebi. Factors driving mortality and growth at treeline: a 30-year experiment of 92 000 conifers. *Ecology*, 93(2):389–401, Feb. 2012. ISSN 1939-9170. doi: 10.1890/11-0384.1. URL <http://onlinelibrary.wiley.com/doi/10.1890/11-0384.1/abstract>.
- T. P. Barnett, J. C. Adam, and D. P. Lettenmaier. Potential impacts of a warming climate on water availability in snow-dominated regions. *Nature*, 438(7066):303–309, Nov. 2005. ISSN 0028-0836. doi: 10.1038/nature04141. URL <http://www.nature.com/nature/journal/v438/n7066/abs/nature04141.html>.
- G. Barrenetxea, F. Ingelrest, G. Schaefer, and M. Vetterli. Wireless Sensor Networks for Environmental Monitoring: The SensorScope Experience. *The 20th IEEE International Zurich Seminar on Communications (IZS 2008)*, 2008a. URL <https://infoscience.epfl.ch/record/115311>.
- G. Barrenetxea, F. Ingelrest, G. Schaefer, M. Vetterli, O. Couach, and M. Parlange. SensorScope: Out-of-the-Box Environmental Monitoring. In *2008 International Conference on Information Processing in Sensor Networks (ipsn 2008)*, pages 332–343, Apr. 2008b. doi: 10.1109/IPSN.2008.28.
- P. Bartelt and M. Lehning. A physical SNOWPACK model for the Swiss avalanche warning: Part I: numerical model. *Cold Regions Science and Technology*, 35(3):123–145, Nov. 2002. ISSN 0165-232X. doi: 10.1016/S0165-232X(02)00074-5. URL <http://www.sciencedirect.com/science/article/pii/S0165232X02000745>.
- M. Bavay and T. Egger. MeteoIO 2.4.2: a preprocessing library for meteorological data. *Geosci. Model Dev.*, 7(6):3135–3151, 2014. ISSN 1991-9603. doi: 10.5194/gmd-7-3135-2014. URL <http://www.geosci-model-dev.net/7/3135/2014/>.
- M. Bavay, M. Lehning, T. Jonas, and H. Löwe. Simulations of future snow cover and discharge in Alpine headwater catchments. *Hydrological Processes*, 23(1):95–108, Jan. 2009. ISSN 1099-1085. doi: 10.1002/hyp.7195. URL <http://onlinelibrary.wiley.com/doi/10.1002/hyp.7195/abstract>.
- M. Bavay, T. Grünwald, and M. Lehning. Response of snow cover and runoff to climate change in high Alpine catchments of Eastern Switzerland. *Advances in Water Resources*, 55:4–16, 2013. ISSN 0309-1708. doi: 10.1016/j.advwatres.2012.12.009. URL <http://www.sciencedirect.com/science/article/pii/S0309170812003193>.

- P. Bebi. Long term meteorological and snow station at 2085 m asl, Stillberg, Davos, Switzerland (1975 - present), WSL Institute for snow and avalanche research SLF, 2016. URL <https://www.envidat.ch/dataset/stillberg-climate>.
- M. Beniston. Variations of Snow Depth and Duration in the Swiss Alps Over the Last 50 Years: Links to Changes in Large-Scale Climatic Forcings. In H. F. Diaz, M. Beniston, and R. S. Bradley, editors, *Climatic Change at High Elevation Sites*, pages 49–68. Springer Netherlands, 1997. ISBN 978-90-481-4890-5 978-94-015-8905-5. doi: 10.1007/978-94-015-8905-5_3. URL http://link.springer.com/chapter/10.1007/978-94-015-8905-5_3.
- G. Blöschl. Scaling issues in snow hydrology. *Hydrological Processes*, 13(14-15):2149–2175, Oct. 1999. ISSN 1099-1085. doi: 10.1002/(SICI)1099-1085(199910)13:14/15<2149::AID-HYP847>3.0.CO;2-8. URL [http://onlinelibrary.wiley.com/doi/10.1002/\(SICI\)1099-1085\(199910\)13:14/15<2149::AID-HYP847>3.0.CO;2-8/abstract](http://onlinelibrary.wiley.com/doi/10.1002/(SICI)1099-1085(199910)13:14/15<2149::AID-HYP847>3.0.CO;2-8/abstract).
- G. Blöschl and R. Kirnbauer. An analysis of snow cover patterns in a small alpine catchment. *Hydrological Processes*, 6(1):99–109, Jan. 1992. ISSN 1099-1085. doi: 10.1002/hyp.3360060109. URL <http://onlinelibrary.wiley.com/doi/10.1002/hyp.3360060109/abstract>.
- G. Botter, E. Bertuzzo, and A. Rinaldo. Transport in the hydrologic response: Travel time distributions, soil moisture dynamics, and the old water paradox. *Water Resources Research*, 46(3):W03514, Mar. 2010. ISSN 1944-7973. doi: 10.1029/2009WR008371. URL <http://onlinelibrary.wiley.com/doi/10.1029/2009WR008371/abstract>.
- R. D. Brown and B. E. Goodison. Snow Cover. In *Encyclopedia of Hydrological Sciences*. John Wiley & Sons, Ltd, 2006. ISBN 978-0-470-84894-4. URL <http://onlinelibrary.wiley.com/doi/10.1002/0470848944.hsa165/abstract>.
- E. Brun, V. Simon, E. Martin, C. Gendreau, and C. Coleau. An Energy and Mass Model of Snow Cover Suitable for Operational Avalanche Forecasting. *Journal of Glaciology*, 35(121):333–342, Jan. 1989. doi: 10.3198/1989JoG35-121-333-342.
- D. H. Burn. Hydrologic effects of climatic change in west-central Canada. *Journal of Hydrology*, 160(1-4):53–70, Aug. 1994. ISSN 00221694. doi: 10.1016/0022-1694(94)90033-7. URL <http://linkinghub.elsevier.com/retrieve/pii/0022169494900337>.
- Y. Bühler, M. Marty, L. Egli, J. Veitinger, T. Jonas, P. Thee, and C. Ginzler. Snow depth mapping in high-alpine catchments using digital photogrammetry. *The Cryosphere*, 9(1):229–243, 2015. ISSN 1994-0424. doi: 10.5194/tc-9-229-2015. URL <http://www.the-cryosphere.net/9/229/2015/>.
- Y. Bühler, M. S. Adams, R. Bösch, and A. Stoffel. Mapping snow depth in alpine terrain with unmanned aerial systems (UASs): potential and limitations. *The Cryosphere*, 10(3):1075–1088, 2016. ISSN 1994-0424. doi: 10.5194/tc-10-1075-2016. URL <http://www.the-cryosphere.net/10/1075/2016/>.

Bibliography

- Campbell Scientific, Inc. CSAT3 Three Dimensional Sonic Anemometer. Instruction Manual Revision:4/17, 2017.
- F. Castellví and R. L. Snyder. Combining the dissipation method and surface renewal analysis to estimate scalar fluxes from the time traces over rangeland grass near Ione (California). *Hydrological Processes*, 23(6):842–857, Mar. 2009. ISSN 1099-1085. doi: 10.1002/hyp.7223. URL <http://onlinelibrary.wiley.com/doi/10.1002/hyp.7223/abstract>.
- F. Ciravegna, H. Huwald, V. Lanfranchi, and U. Wehn de Montalvo. Citizen observatories: the WeSenseIt vision. *Proceedings of the INSPIRE*, 2013.
- M. P. Clark, J. Hendrikx, A. G. Slater, D. Kavetski, B. Anderson, N. J. Cullen, T. Kerr, E. Örn Hreinsson, and R. A. Woods. Representing spatial variability of snow water equivalent in hydrologic and land-surface models: A review. *Water Resources Research*, 47(7):W07539, 2011. ISSN 1944-7973. doi: 10.1029/2011WR010745. URL <http://onlinelibrary.wiley.com/doi/10.1029/2011WR010745/abstract>.
- S. C. Colbeck. An overview of seasonal snow metamorphism. *Reviews of Geophysics*, 20(1): 45–61, Feb. 1982. ISSN 1944-9208. doi: 10.1029/RG020i001p00045. URL <http://onlinelibrary.wiley.com/doi/10.1029/RG020i001p00045/abstract>.
- F. Comola, B. Schaeffli, A. Rinaldo, and M. Lehning. Thermodynamics in the hydrologic response: Travel time formulation and application to Alpine catchments. *Water Resources Research*, 51(3):1671–1687, Mar. 2015a. ISSN 1944-7973. doi: 10.1002/2014WR016228. URL <http://onlinelibrary.wiley.com/doi/10.1002/2014WR016228/abstract>.
- F. Comola, B. Schaeffli, P. D. Ronco, G. Botter, M. Bavay, A. Rinaldo, and M. Lehning. Scale-dependent effects of solar radiation patterns on the snow-dominated hydrologic response. *Geophysical Research Letters*, 42(10):2015GL064075, 2015b. ISSN 1944-8007. doi: 10.1002/2015GL064075. URL <http://onlinelibrary.wiley.com/doi/10.1002/2015GL064075/abstract>.
- D. S. Crook and A. M. Jones. Design Principles from Traditional Mountain Irrigation Systems (Bisses) in the Valais, Switzerland. *Mountain Research and Development*, 19(2):79–99, 1999. ISSN 0276-4741. doi: 10.2307/3674250. URL <http://www.jstor.org/stable/3674250>.
- T. J. Day. On the precision of salt dilution gauging. *Journal of Hydrology*, 31(3):293–306, 1976. ISSN 0022-1694. doi: 10.1016/0022-1694(76)90130-X. URL <http://www.sciencedirect.com/science/article/pii/002216947690130X>.
- J. S. Deems and T. H. Painter. Lidar measurement of snow depth: accuracy and error sources. In *proceedings of the international snow science workshop*, pages 1–6, 2006.
- J. S. Deems, T. H. Painter, and D. C. Finnegan. Lidar measurement of snow depth: a review. *Journal of Glaciology*, 59(215):467–479, July 2013. doi: 10.3189/2013JoG12J154.
- J. S. Deems, P. J. Gadowski, D. Vellone, R. Evanczyk, A. L. LeWinter, K. W. Birkeland, and D. C. Finnegan. Mapping starting zone snow depth with a ground-based lidar to assist avalanche

- control and forecasting. *Cold Regions Science and Technology*, 120:197–204, Dec. 2015. ISSN 0165-232X. doi: 10.1016/j.coldregions.2015.09.002. URL <http://www.sciencedirect.com/science/article/pii/S0165232X15001883>.
- D. R. DeWalle and A. Rango. *Principles of snow hydrology*. Cambridge University Press, Cambridge, 2008. ISBN 978-0-521-82362-30-521-82362-5978-0-511-41214-10-511-41214-2978-0-511-53567-31010179780511535673.
- J. Dozier. Mountain hydrology, snow color, and the fourth paradigm. *Eos, Transactions American Geophysical Union*, 92(43):373–374, Oct. 2011. ISSN 2324-9250. doi: 10.1029/2011EO430001. URL <http://onlinelibrary.wiley.com/doi/10.1029/2011EO430001/abstract>.
- L. Egli, T. Jonas, T. Grünwald, M. Schirmer, and P. Burlando. Dynamics of snow ablation in a small Alpine catchment observed by repeated terrestrial laser scans. *Hydrological Processes*, 26(10):1574–1585, 2012. ISSN 1099-1085. doi: 10.1002/hyp.8244. URL <http://onlinelibrary.wiley.com/doi/10.1002/hyp.8244/abstract>.
- D. Eiriksson, M. Whitson, C. H. Luce, H. P. Marshall, J. Bradford, S. G. Benner, T. Black, H. Hetrick, and J. P. McNamara. An evaluation of the hydrologic relevance of lateral flow in snow at hillslope and catchment scales. *Hydrological Processes*, 27(5):640–654, Feb. 2013. ISSN 1099-1085. doi: 10.1002/hyp.9666. URL <http://onlinelibrary.wiley.com/doi/10.1002/hyp.9666/abstract>.
- K. Elder, J. Dozier, and J. Michaelsen. Snow accumulation and distribution in an Alpine Watershed. *Water Resources Research*, 27(7):1541–1552, July 1991. ISSN 1944-7973. doi: 10.1029/91WR00506. URL <http://onlinelibrary.wiley.com/doi/10.1029/91WR00506/abstract>.
- R. Essery, N. Rutter, J. Pomeroy, R. Baxter, M. Stähli, D. Gustafsson, A. Barr, P. Bartlett, and K. Elder. SNOWMIP2: An Evaluation of Forest Snow Process Simulations. *Bulletin of the American Meteorological Society*, 90(8):1120–1135, Aug. 2009. ISSN 0003-0007. doi: 10.1175/2009BAMS2629.1. URL <http://journals.ametsoc.org/doi/abs/10.1175/2009BAMS2629.1>.
- P. Etchevers, E. Martin, R. Brown, C. Fierz, Y. Lejeune, E. Bazile, A. Boone, Y.-J. Dai, R. Essery, A. Fernandez, Y. Gusev, R. Jordan, V. Koren, E. Kowalczyk, N. O. Nasonova, R. D. Pyles, A. Schlosser, A. B. Shmakin, T. G. Smirnova, U. Strasser, D. Verseghy, T. Yamazaki, and Z.-L. Yang. Validation of the energy budget of an alpine snowpack simulated by several snow models (SnowMIP project). *Annals of Glaciology*, 38(1):150–158, Jan. 2004. ISSN 02603055, 17275644. doi: 10.3189/172756404781814825. URL <http://openurl.ingenta.com/content/xref?genre=article&issn=0260-3055&volume=38&issue=1&spage=150>.
- M. Fischer, M. Huss, M. Kummert, and M. Hoelzle. Application and validation of long-range terrestrial laser scanning to monitor the mass balance of very small glaciers in the Swiss Alps. *The Cryosphere*, 10(3):1279–1295, June 2016. ISSN 1994-0424. doi: 10.5194/tc-10-1279-2016. URL <https://www.the-cryosphere.net/10/1279/2016/>.

Bibliography

- FOEN. Federal Office for the Environment - Hydrological data and forecasts: Dischmabach - Davos, Kriegsmatte, 2017. URL <http://www.hydrodaten.admin.ch/en/2327.html>.
- FOEN. Federal Office for the Environment - Hydrological data and forecasts: Hydrological Study Areas in Switzerland (HUG), 2018. URL <https://www.bafu.admin.ch/bafu/en/home/topics/water/state/water--monitoring-networks/hydrological-study-areas-in-switzerland--hug-.html>.
- T. Foken and C. J. Nappo. *Micrometeorology*. Springer, Berlin, 2008. ISBN 978-3-540-74665-2. URL http://sfx.ethz.ch/sfx_locator?sid=ALEPH:EBI01&genre=book&isbn=9783540746669&id=doi:10.1007/978-3-540-74666-9.
- C. Frei and C. Schär. A precipitation climatology of the Alps from high-resolution rain-gauge observations. *International Journal of Climatology*, 18(8):873–900, 1998. ISSN 1097-0088. doi: 10.1002/(SICI)1097-0088(19980630)18:8<873::AID-JOC255>3.0.CO;2-9. URL [http://onlinelibrary.wiley.com/doi/10.1002/\(SICI\)1097-0088\(19980630\)18:8<873::AID-JOC255>3.0.CO;2-9/abstract](http://onlinelibrary.wiley.com/doi/10.1002/(SICI)1097-0088(19980630)18:8<873::AID-JOC255>3.0.CO;2-9/abstract).
- A. Gallice, M. Bavay, T. Brauchli, F. Comola, M. Lehning, and H. Huwald. StreamFlow 1.0: an extension to the spatially distributed snow model Alpine3d for hydrological modelling and deterministic stream temperature prediction. *Geosci. Model Dev.*, 9(12):4491–4519, 2016. ISSN 1991-9603. doi: 10.5194/gmd-9-4491-2016. URL <http://www.geosci-model-dev.net/9/4491/2016/>.
- R. Geiger, R. H. Aron, and P. Todhunter. *The Climate Near the Ground*. Rowman & Littlefield, 2003. ISBN 978-0-7425-1857-5. Google-Books-ID: KaJHBv9FbYIC.
- F. Gerber, M. Lehning, S. W. Hoch, and R. Mott. A close-ridge small-scale atmospheric flow field and its influence on snow accumulation. *Journal of Geophysical Research: Atmospheres*, 122(15):2016JD026258, Aug. 2017. ISSN 2169-8996. doi: 10.1002/2016JD026258. URL <http://onlinelibrary.wiley.com/doi/10.1002/2016JD026258/abstract>.
- B. E. Goodison, P. Y. T. Louie, and D. Yang. The WMO solid precipitation measurement inter-comparison. *World Meteorological Organization-Publications-WMO TD*, pages 65–70, 1997. URL https://www.researchgate.net/profile/Daqing_Yang/publication/248460987_WMO_solid_precipitation_measurement_intercomparison/links/5440381c0cf2fd72f99dd3b0.pdf.
- I. Gouttevin, M. Lehning, T. Jonas, D. Gustafsson, and M. Mölder. A two-layer canopy model with thermal inertia for an improved snowpack energy balance below needleleaf forest (model SNOWPACK, version 3.2.1, revision 741). *Geoscientific Model Development*, 8(8): 2379–2398, Aug. 2015. ISSN 1991-9603. doi: 10.5194/gmd-8-2379-2015. URL <http://www.geosci-model-dev.net/8/2379/2015/>.
- T. Grünewald and M. Lehning. Altitudinal dependency of snow amounts in two small alpine catchments: can catchment-wide snow amounts be estimated via single snow or

- precipitation stations? *Annals of Glaciology*, 52(58):153–158, Aug. 2011. doi: 10.3189/172756411797252248.
- T. Grünewald and M. Lehning. Are flat-field snow depth measurements representative? A comparison of selected index sites with areal snow depth measurements at the small catchment scale. *Hydrological Processes*, 29(7):1717–1728, Mar. 2015. ISSN 1099-1085. doi: 10.1002/hyp.10295. URL <https://onlinelibrary.wiley.com/doi/abs/10.1002/hyp.10295>.
- T. Grünewald, M. Schirmer, R. Mott, and M. Lehning. Spatial and temporal variability of snow depth and ablation rates in a small mountain catchment. *The Cryosphere*, 4(2):215–225, 2010. ISSN 1994-0424. doi: 10.5194/tc-4-215-2010. URL <http://www.the-cryosphere.net/4/215/2010/>.
- T. Grünewald, Y. Bühler, and M. Lehning. Elevation dependency of mountain snow depth. *The Cryosphere*, 8(6):2381–2394, 2014. ISSN 1994-0424. doi: 10.5194/tc-8-2381-2014. URL <http://www.the-cryosphere.net/8/2381/2014/>.
- J. Gurtz, M. Zappa, K. Jasper, H. Lang, M. Verbunt, A. Badoux, and T. Vitvar. A comparative study in modelling runoff and its components in two mountainous catchments. *Hydrological Processes*, 17(2):297–311, 2003. ISSN 1099-1085. doi: 10.1002/hyp.1125. URL <http://onlinelibrary.wiley.com/doi/10.1002/hyp.1125/abstract>.
- R. J. Harding and J. W. Pomeroy. The Energy Balance of the Winter Boreal Landscape. *Journal of Climate*, 9(11):2778–2787, Nov. 1996. ISSN 0894-8755. doi: 10.1175/1520-0442(1996)009<2778:TEBOTW>2.0.CO;2. URL [http://journals.ametsoc.org/doi/abs/10.1175/1520-0442\(1996\)009%3C2778:TEBOTW%3E2.0.CO;2](http://journals.ametsoc.org/doi/abs/10.1175/1520-0442(1996)009%3C2778:TEBOTW%3E2.0.CO;2).
- J. Hatfield, J. Baker, T. J. Sauer, and R. Horton. Soil Heat Flux. In *Agronomy Monograph*. American Society of Agronomy, Crop Science Society of America, and Soil Science Society of America, 2005. ISBN 978-0-89118-268-9. doi: 10.2134/agronmonogr47.c7. URL <https://dl.sciencesocieties.org/publications/books/abstracts/agronymonogra/micrometeorolog/131>.
- R. Hock. Temperature index melt modelling in mountain areas. *Journal of Hydrology*, 282(1–4):104–115, Nov. 2003. ISSN 0022-1694. doi: 10.1016/S0022-1694(03)00257-9. URL <http://www.sciencedirect.com/science/article/pii/S0022169403002579>.
- C. Hopkinson, M. Sitar, L. Chasmer, and P. Treitz. Mapping snowpack depth beneath forest canopies using airborne lidar. *Photogrammetric Engineering & Remote Sensing*, 70(3):323–330, 2004.
- P. Horton, B. Schaeffli, A. Mezghani, B. Hingray, and A. Musy. Assessment of climate-change impacts on alpine discharge regimes with climate model uncertainty. *Hydrological Processes*, 20(10):2091–2109, 2006. ISSN 1099-1085. doi: 10.1002/hyp.6197. URL <http://onlinelibrary.wiley.com/doi/10.1002/hyp.6197/abstract>.

Bibliography

- H. Huwald, C. W. Higgins, W. C. Evans, A. Bahr, A. Martinoli, and M. B. Parlange. Estimation of sensible heat flux using a flux variance approach, in preparation. 2018.
- D. Ineichen, E. Brockmann, and S. Schaer. Enhancing the Swiss permanent GPS network (AGNES) for GLONASS. *Subcommission for the European reference frame (EUREF)*, 2007.
- F. A. Isotta, C. Frei, V. Weigluni, M. Perčec Tadić, P. Lassègues, B. Rudolf, V. Pavan, C. Cacciamani, G. Antolini, S. M. Ratto, M. Munari, S. Micheletti, V. Bonati, C. Lussana, C. Ronchi, E. Panettieri, G. Marigo, and G. Vertačnik. The climate of daily precipitation in the Alps: development and analysis of a high-resolution grid dataset from pan-Alpine rain-gauge data. *International Journal of Climatology*, 34(5):1657–1675, Apr. 2014. ISSN 1097-0088. doi: 10.1002/joc.3794. URL <http://onlinelibrary.wiley.com/doi/10.1002/joc.3794/abstract>.
- T. Jonas, C. Marty, and J. Magnusson. Estimating the snow water equivalent from snow depth measurements in the Swiss Alps. *Journal of Hydrology*, 378(1–2):161–167, Nov. 2009. ISSN 0022-1694. doi: 10.1016/j.jhydrol.2009.09.021. URL <http://www.sciencedirect.com/science/article/pii/S0022169409005848>.
- R. Juras, S. Würzer, J. Pavlásek, T. Vitvar, and T. Jonas. Rainwater propagation through snowpack during rain-on-snow sprinkling experiments under different snow conditions. *Hydrol. Earth Syst. Sci.*, 21(9):4973–4987, Sept. 2017. ISSN 1607-7938. doi: 10.5194/hess-21-4973-2017. URL <https://www.hydrol-earth-syst-sci.net/21/4973/2017/>.
- R. Kattelmann. Snowmelt lysimeters in the evaluation of snowmelt models. *Annals of Glaciology*, 31(1):406–410, Jan. 2000. ISSN 02603055, 17275644. doi: 10.3189/172756400781820048. URL <http://openurl.ingenta.com/content/xref?genre=article&issn=0260-3055&volume=31&issue=1&page=406>.
- R. C. Kattelmann. Snowmelt lysimeters: design and use. In *Proceedings of the 52nd Annual Western Snow Conference*, Proceedings of the 52nd Annual Western Snow Conference, pages 68–79, Sun Valley, Idaho, Apr. 1984. Western Snow Conference.
- G. Katul, C.-I. Hsieh, R. Oren, D. Ellsworth, and N. Phillips. Latent and sensible heat flux predictions from a uniform pine forest using surface renewal and flux variance methods. *Boundary-Layer Meteorology*, 80(3):249–282, Aug. 1996. ISSN 0006-8314, 1573-1472. doi: 10.1007/BF00119545. URL <https://link.springer.com/article/10.1007/BF00119545>.
- N. J. Kinar and J. W. Pomeroy. Measurement of the physical properties of the snowpack. *Reviews of Geophysics*, 53(2):2015RG000481, 2015. ISSN 1944-9208. doi: 10.1002/2015RG000481. URL <http://onlinelibrary.wiley.com/doi/10.1002/2015RG000481/abstract>.
- P. R. Kormos, D. Marks, J. P. McNamara, H. P. Marshall, A. Winstral, and A. N. Flores. Snow distribution, melt and surface water inputs to the soil in the mountain rain–snow transition zone. *Journal of Hydrology*, 519:190–204, Nov. 2014. ISSN 0022-1694. doi: 10.1016/j.jhydrol.2014.06.051. URL <http://www.sciencedirect.com/science/article/pii/S0022169414005113>.

- M. Kumar, D. Marks, J. Dozier, M. Reba, and A. Winstral. Evaluation of distributed hydrologic impacts of temperature-index and energy-based snow models. *Advances in Water Resources*, 56:77–89, June 2013. ISSN 03091708. doi: 10.1016/j.advwatres.2013.03.006. URL <http://linkinghub.elsevier.com/retrieve/pii/S0309170813000389>.
- Kyaw Tha Paw U, J. Qiu, H.-B. Su, T. Watanabe, and Y. Brunet. Surface renewal analysis: a new method to obtain scalar fluxes. *Agricultural and Forest Meteorology*, 74(1):119–137, Apr. 1995. ISSN 0168-1923. doi: 10.1016/0168-1923(94)02182-J. URL <http://www.sciencedirect.com/science/article/pii/016819239402182J>.
- V. Lanfranchi, S. N. Wrigley, N. Ireson, U. Wehn, and F. Ciravegna. Citizens' observatories for situation awareness in flooding. In *ISCRAM*, 2014.
- M. Lehning. Energy Balance and Thermophysical Processes in Snowpacks. In *Encyclopedia of Hydrological Sciences*. John Wiley & Sons, Ltd, 2006. ISBN 978-0-470-84894-4.
- M. Lehning, P. Bartelt, B. Brown, T. Russi, U. Stöckli, and M. Zimmerli. A network of automatic weather and snow stations and supplementary model calculations providing snowpack information for avalanche warning. In *Proceedings of the International Snow Science Workshop "a Merging of Theory and Practice"*, pages 225–233, 1998. URL <http://arc.lib.montana.edu/snow-science/objects/issw-1998-225-233.pdf>.
- M. Lehning, P. Bartelt, B. Brown, T. Russi, U. Stöckli, and M. Zimmerli. Snowpack model calculations for avalanche warning based upon a new network of weather and snow stations. *Cold Regions Science and Technology*, 30(1–3):145–157, 1999. ISSN 0165-232X. doi: 10.1016/S0165-232X(99)00022-1. URL <http://www.sciencedirect.com/science/article/pii/S0165232X99000221>.
- M. Lehning, P. Bartelt, B. Brown, and C. Fierz. A physical SNOWPACK model for the Swiss avalanche warning: Part III: meteorological forcing, thin layer formation and evaluation. *Cold Regions Science and Technology*, 35(3):169–184, Nov. 2002a. ISSN 0165-232X. doi: 10.1016/S0165-232X(02)00072-1. URL <http://www.sciencedirect.com/science/article/pii/S0165232X02000721>.
- M. Lehning, P. Bartelt, B. Brown, C. Fierz, and P. Satyawali. A physical SNOWPACK model for the Swiss avalanche warning: Part II. Snow microstructure. *Cold Regions Science and Technology*, 35(3):147–167, Nov. 2002b. ISSN 0165-232X. doi: 10.1016/S0165-232X(02)00073-3. URL <http://www.sciencedirect.com/science/article/pii/S0165232X02000733>.
- M. Lehning, I. Völksch, D. Gustafsson, T. A. Nguyen, M. Stähli, and M. Zappa. ALPINE3d: a detailed model of mountain surface processes and its application to snow hydrology. *Hydrological Processes*, 20(10):2111–2128, 2006. ISSN 1099-1085. doi: 10.1002/hyp.6204. URL <http://onlinelibrary.wiley.com/doi/10.1002/hyp.6204/abstract>.
- M. Lehning, H. Löwe, M. Ryser, and N. Raderschall. Inhomogeneous precipitation distribution and snow transport in steep terrain. *Water Resources Research*, 44(7):W07404, 2008. ISSN

Bibliography

- 1944-7973. doi: 10.1029/2007WR006545. URL <http://onlinelibrary.wiley.com/doi/10.1029/2007WR006545/abstract>.
- H.-P. Liniger, R. Weingartner, and M. Grosjean. *Mountains of the world: water towers for the 21st century - A contribution to Global Freshwater Management. Mountain agenda.*, volume Nr. 207 of *Publikation Gewässerkunde*. Institut of Geography, Berne, 1998.
- C. H. Luce, D. G. Tarboton, and K. R. Cooley. The influence of the spatial distribution of snow on basin-averaged snowmelt. *Hydrological Processes*, 12(10-11):1671–1683, 1998. ISSN 1099-1085. doi: 10.1002/(SICI)1099-1085(199808/09)12:10/11<1671::AID-HYP688>3.0.CO;2-N. URL [http://onlinelibrary.wiley.com/doi/10.1002/\(SICI\)1099-1085\(199808/09\)12:10/11<1671::AID-HYP688>3.0.CO;2-N/abstract](http://onlinelibrary.wiley.com/doi/10.1002/(SICI)1099-1085(199808/09)12:10/11<1671::AID-HYP688>3.0.CO;2-N/abstract).
- J. D. Lundquist and M. D. Dettinger. How snowpack heterogeneity affects diurnal streamflow timing. *Water Resources Research*, 41(5):W05007, 2005. ISSN 1944-7973. doi: 10.1029/2004WR003649. URL <http://onlinelibrary.wiley.com/doi/10.1029/2004WR003649/abstract>.
- D. H. Male and R. J. Granger. Snow surface energy exchange. *Water Resources Research*, 17(3):609–627, June 1981. ISSN 1944-7973. doi: 10.1029/WR017i003p00609. URL <http://onlinelibrary.wiley.com/doi/10.1029/WR017i003p00609/abstract>.
- S. A. Malek, F. Avanzi, K. Brun-Laguna, T. Maurer, C. A. Oroza, P. C. Hartsough, T. Watteyne, and S. D. Glaser. Real-Time Alpine Measurement System Using Wireless Sensor Networks. *Sensors*, 17(11):2583, Nov. 2017. doi: 10.3390/s17112583. URL <http://www.mdpi.com/1424-8220/17/11/2583>.
- D. Marks and J. Dozier. Climate and energy exchange at the snow surface in the Alpine Region of the Sierra Nevada: 2. Snow cover energy balance. *Water Resources Research*, 28(11):3043–3054, Nov. 1992. ISSN 1944-7973. doi: 10.1029/92WR01483. URL <http://onlinelibrary.wiley.com/doi/10.1029/92WR01483/abstract>.
- D. Marks, J. Domingo, D. Susong, T. Link, and D. Garen. A spatially distributed energy balance snowmelt model for application in mountain basins. *Hydrological Processes*, 13(12-13):1935–1959, Sept. 1999. ISSN 1099-1085. doi: 10.1002/(SICI)1099-1085(199909)13:12/13<1935::AID-HYP868>3.0.CO;2-C. URL [http://onlinelibrary.wiley.com/doi/10.1002/\(SICI\)1099-1085\(199909\)13:12/13<1935::AID-HYP868>3.0.CO;2-C/abstract](http://onlinelibrary.wiley.com/doi/10.1002/(SICI)1099-1085(199909)13:12/13<1935::AID-HYP868>3.0.CO;2-C/abstract).
- J. Martinec. Snowmelt - Runoff Model for Stream Flow Forecasts. *Hydrology Research*, 6(3):145–154, June 1975. ISSN 0029-1277, 2224-7955. URL <http://hr.iwaponline.com/content/6/3/145>.
- J. Martinec and A. Rango. Interpretation and utilization of areal snow cover data from satellites. *Annals of Glaciology*, 1987. URL http://www.igsoc.org:8080/annals/9/igs_annals_vol09_year1987_pg166-169.pdf.

- J. R. Martinec. Discharge forecasts in mountain basins based on satellite snow cover mapping. [Dinwoody Creek Basin, Wyoming and the Dischma Basin, Switzerland]. May 1980. URL <https://ntrs.nasa.gov/search.jsp?R=19800017258>.
- C. Marty, S. Schlögl, M. Bavay, and M. Lehning. How much can we save? Impact of different emission scenarios on future snow cover in the Alps. *The Cryosphere*, 11(1):517–529, Feb. 2017. ISSN 1994-0424. doi: 10.5194/tc-11-517-2017. URL <https://www.the-cryosphere.net/11/517/2017/>.
- A. B. Mazurkiewicz, D. G. Callery, and J. J. McDonnell. Assessing the controls of the snow energy balance and water available for runoff in a rain-on-snow environment. *Journal of Hydrology*, 354(1):1–14, June 2008. ISSN 0022-1694. doi: 10.1016/j.jhydrol.2007.12.027. URL <http://www.sciencedirect.com/science/article/pii/S0022169408000061>.
- M. Mazzoleni, V. J. Cortes Arevalo, U. Wehn, L. Alfonso, D. Norbiato, M. Monego, M. Ferri, and D. P. Solomatine. Exploring the influence of citizen involvement on the assimilation of crowdsourced observations: a modelling study based on the 2013 flood event in the Bacchiglione catchment (Italy). *Hydrol. Earth Syst. Sci.*, 22(1):391–416, Jan. 2018. ISSN 1607-7938. doi: 10.5194/hess-22-391-2018. URL <https://www.hydrol-earth-syst-sci.net/22/391/2018/>.
- D. Mellis, M. Banzi, D. Cuartielles, and T. Igoe. Arduino: An open electronic prototyping platform. In *Proc. Chi*, volume 2007, 2007.
- L. Menzel, H. Lang, and M. Rohmann. Plate 4.1 Mean Annual Actual Evaporation 1973–1992, 1999.
- G. Michlmayr, M. Lehning, G. Koboltschnig, H. Holzmann, M. Zappa, R. Mott, and W. Schöner. Application of the Alpine 3d model for glacier mass balance and glacier runoff studies at Goldbergkees, Austria. *Hydrological Processes*, 22(19):3941–3949, Sept. 2008. ISSN 1099-1085. doi: 10.1002/hyp.7102. URL <http://onlinelibrary.wiley.com/doi/10.1002/hyp.7102/abstract>.
- H. Middelkoop, K. Daamen, D. Gellens, W. Grabs, J. C. J. Kwadijk, H. Lang, B. W. a. H. Parmet, B. Schädler, J. Schulla, and K. Wilke. Impact of Climate Change on Hydrological Regimes and Water Resources Management in the Rhine Basin. *Climatic Change*, 49(1-2):105–128, Apr. 2001. ISSN 0165-0009, 1573-1480. doi: 10.1023/A:1010784727448. URL <http://link.springer.com/article/10.1023/A:1010784727448>.
- A. S. Monin and A. M. F. Obukhov. Basic laws of turbulent mixing in the surface layer of the atmosphere. *Contrib. Geophys. Inst. Acad. Sci. USSR*, 151:163–187, 1954. URL http://www.mcnaught.com/keith/papers/Monin_and_Obukhov_1954.pdf.
- R. Mott and M. Lehning. Meteorological Modeling of Very High-Resolution Wind Fields and Snow Deposition for Mountains. *Journal of Hydrometeorology*, 11(4):934–949, Apr. 2010. ISSN 1525-755X. doi: 10.1175/2010JHM1216.1. URL <http://journals.ametsoc.org/doi/full/10.1175/2010JHM1216.1>.

Bibliography

- R. Mott, M. Schirmer, M. Bavay, T. Grünewald, and M. Lehning. Understanding snow-transport processes shaping the mountain snow-cover. *The Cryosphere*, 4(4):545–559, 2010. ISSN 1994-0424. doi: 10.5194/tc-4-545-2010. URL <http://www.the-cryosphere.net/4/545/2010/>.
- R. Mott, L. Egli, T. Grünewald, N. Dawes, C. Manes, M. Bavay, and M. Lehning. Micrometeorological processes driving snow ablation in an Alpine catchment. *The Cryosphere*, 5(4):1083–1098, Nov. 2011. ISSN 1994-0424. doi: 10.5194/tc-5-1083-2011. URL <http://www.the-cryosphere.net/5/1083/2011/>.
- R. Mott, C. Gromke, T. Grünewald, and M. Lehning. Relative importance of advective heat transport and boundary layer decoupling in the melt dynamics of a patchy snow cover. *Advances in Water Resources*, 55:88–97, 2013. ISSN 0309-1708. doi: 10.1016/j.advwatres.2012.03.001. URL <http://www.sciencedirect.com/science/article/pii/S0309170812000504>.
- R. Mott, D. Scipión, M. Schneebeli, N. Dawes, A. Berne, and M. Lehning. Orographic effects on snow deposition patterns in mountainous terrain. *Journal of Geophysical Research: Atmospheres*, 119(3):1419–1439, Feb. 2014. ISSN 2169-8996. doi: 10.1002/2013JD019880. URL <http://onlinelibrary.wiley.com/doi/10.1002/2013JD019880/abstract>.
- R. Mott, M. Daniels, and M. Lehning. Atmospheric Flow Development and Associated Changes in Turbulent Sensible Heat Flux over a Patchy Mountain Snow Cover. *Journal of Hydrometeorology*, 16(3):1315–1340, 2015. ISSN 1525-755X. doi: 10.1175/JHM-D-14-0036.1. URL <http://journals.ametsoc.org/doi/abs/10.1175/JHM-D-14-0036.1>.
- R. Mott, S. Schlögl, L. Dirks, and M. Lehning. Impact of Extreme Land Surface Heterogeneity on Micrometeorology over Spring Snow Cover. *Journal of Hydrometeorology*, 18(10):2705–2722, Aug. 2017. ISSN 1525-755X. doi: 10.1175/JHM-D-17-0074.1. URL <http://journals.ametsoc.org/doi/abs/10.1175/JHM-D-17-0074.1>.
- K. N. Musselman, M. P. Clark, C. Liu, K. Ikeda, and R. Rasmussen. Slower snowmelt in a warmer world. *Nature Climate Change*, 7(3):214–219, Mar. 2017. ISSN 1758-678X. doi: 10.1038/nclimate3225. URL <http://www.nature.com/nclimate/journal/v7/n3/full/nclimate3225.html>.
- J. E. Nash and J. V. Sutcliffe. River flow forecasting through conceptual models part I — A discussion of principles. *Journal of Hydrology*, 10(3):282–290, 1970. ISSN 0022-1694. doi: 10.1016/0022-1694(70)90255-6. URL <http://www.sciencedirect.com/science/article/pii/0022169470902556>.
- A. W. Nolin. Recent advances in remote sensing of seasonal snow. *Journal of Glaciology*, 56(200):1141–1150, 2010. doi: 10.3189/002214311796406077.
- A. Ohmura. Physical Basis for the Temperature-Based Melt-Index Method. *Journal of Applied Meteorology*, 40(4):753–761, Apr. 2001. ISSN 0894-8763. doi: 10.1175/1520-0450(2001)040<0753:PBFTTB>2.0.CO;2. URL <https://journals.ametsoc.org/doi/10.1175/1520-0450%282001%29040%3C0753%3APBFTTB%3E2.0.CO%3B2>.

- R. K. Pachauri, M. R. Allen, V. R. Barros, J. Broome, W. Cramer, R. Christ, J. A. Church, L. Clarke, Q. Dahe, P. Dasgupta, N. K. Dubash, O. Edenhofer, I. Elgizouli, C. B. Field, P. Forster, P. Friedlingstein, J. Fuglestedt, L. Gomez-Echeverri, S. Hallegatte, G. Hegerl, M. Howden, K. Jiang, B. Jimenez Cisneroz, V. Kattsov, H. Lee, K. J. Mach, J. Marotzke, M. D. Mastrandrea, L. Meyer, J. Minx, Y. Mulugetta, K. O'Brien, M. Oppenheimer, J. J. Pereira, R. Pichs-Madruga, G.-K. Plattner, H.-O. Pörtner, S. B. Power, B. Preston, N. H. Ravindranath, A. Reisinger, K. Riahi, M. Rusticucci, R. Scholes, K. Seyboth, Y. Sokona, R. Stavins, T. F. Stocker, P. Tschakert, D. van Vuuren, and J.-P. van Ypserle. *Climate Change 2014: Synthesis Report. Contribution of Working Groups I, II and III to the Fifth Assessment Report of the Intergovernmental Panel on Climate Change*. IPCC, Geneva, Switzerland, 2014. ISBN 978-92-9169-143-2. URL <https://epic.awi.de/37530/>.
- T. H. Painter, D. F. Berisford, J. W. Boardman, K. J. Bormann, J. S. Deems, F. Gehrke, A. Hedrick, M. Joyce, R. Laidlaw, D. Marks, C. Mattmann, B. McGurk, P. Ramirez, M. Richardson, S. M. Skiles, F. C. Seidel, and A. Winstral. The Airborne Snow Observatory: Fusion of scanning lidar, imaging spectrometer, and physically-based modeling for mapping snow water equivalent and snow albedo. *Remote Sensing of Environment*, 184:139–152, Oct. 2016. ISSN 0034-4257. doi: 10.1016/j.rse.2016.06.018. URL <http://www.sciencedirect.com/science/article/pii/S0034425716302577>.
- C. Poblete-Echeverría, D. Sepúlveda-Reyes, and S. Ortega-Farías. Effect of height and time lag on the estimation of sensible heat flux over a drip-irrigated vineyard using the surface renewal (SR) method across distinct phenological stages. *Agricultural Water Management*, 141:74–83, July 2014. ISSN 0378-3774. doi: 10.1016/j.agwat.2014.04.006. URL <http://www.sciencedirect.com/science/article/pii/S0378377414001085>.
- A. Prokop. Assessing the applicability of terrestrial laser scanning for spatial snow depth measurements. *Cold Regions Science and Technology*, 54(3):155–163, Nov. 2008. ISSN 0165-232X. doi: 10.1016/j.coldregions.2008.07.002. URL <http://www.sciencedirect.com/science/article/pii/S0165232X08001018>.
- A. Prokop, M. Schirmer, M. Rub, M. Lehning, and M. Stocker. A comparison of measurement methods: terrestrial laser scanning, tachymetry and snow probing for the determination of the spatial snow-depth distribution on slopes. *Annals of Glaciology*, 49(1):210–216, Oct. 2008. doi: 10.3189/172756408787814726.
- A. Prokop, P. Schön, F. Singer, G. Pulfer, M. Naaim, E. Thibert, and A. Soruco. Merging terrestrial laser scanning technology with photogrammetric and total station data for the determination of avalanche modeling parameters. *Cold Regions Science and Technology*, 110:223–230, 2015. ISSN 0165-232X. doi: 10.1016/j.coldregions.2014.11.009. URL <http://www.sciencedirect.com/science/article/pii/S0165232X14002110>.
- M. S. Raleigh and E. E. Small. Snowpack density modeling is the primary source of uncertainty when mapping basin-wide SWE with lidar. *Geophysical Research Letters*, 44

Bibliography

- (8):2016GL071999, Apr. 2017. ISSN 1944-8007. doi: 10.1002/2016GL071999. URL <http://onlinelibrary.wiley.com/doi/10.1002/2016GL071999/abstract>.
- G. Rees. *Remote sensing of snow and ice*. Taylor & Francis, Boca Raton, 2006. ISBN 978-0-415-29831-5.
- J. Revuelto, J. I. López-Moreno, C. Azorin-Molina, J. Zabalza, G. Arguedas, and S. M. Vicente-Serrano. Mapping the annual evolution of snow depth in a small catchment in the Pyrenees using the long-range terrestrial laser scanning. *Journal of Maps*, 10(3):379–393, 2014. ISSN null. doi: 10.1080/17445647.2013.869268. URL <http://dx.doi.org/10.1080/17445647.2013.869268>.
- M. Richardson and S. Wallace. *Getting started with raspberry PI*. " O'Reilly Media, Inc.", 2012.
- J. C. Rodda and I. A. Shiklomanov. *World water resources at the beginning of the 21st century*. Cambridge [England] ; New York : Cambridge University Press, 2003. ISBN 978-0-521-82085-1. URL <https://trove.nla.gov.au/version/19098906>.
- G. H. Roe. Orographic Precipitation. *Annual Review of Earth and Planetary Sciences*, 33(1):645–671, 2005. doi: 10.1146/annurev.earth.33.092203.122541. URL <http://www.annualreviews.org/doi/abs/10.1146/annurev.earth.33.092203.122541>.
- B. Schaefli. Snow hydrology signatures for model identification within a limits-of-acceptability approach. *Hydrological Processes*, 30(22):4019–4035, Oct. 2016. ISSN 1099-1085. doi: 10.1002/hyp.10972. URL <http://onlinelibrary.wiley.com/doi/10.1002/hyp.10972/abstract>.
- B. Schaefli, B. Hingray, and A. Musy. Climate change and hydropower production in the Swiss Alps: quantification of potential impacts and related modelling uncertainties. *Hydrology and Earth System Sciences*, 11(3):1191–1205, May 2007. ISSN 1607-7938. doi: 10.5194/hess-11-1191-2007. URL <http://www.hydrol-earth-syst-sci.net/11/1191/2007/>.
- B. Schaefli, N. Ceperley, T. Brauchli, M. Lehning, T. Jonas, and M. Zappa. The Dischma river mystery: why does my snow hydrological model not work here ? volume 18, pages EPSC2016–1624, Apr. 2016. URL <http://adsabs.harvard.edu/abs/2016EGUGA..18.1624S>.
- A. Schaffhauser, M. Adams, R. Fromm, P. Jörg, G. Luzi, L. Noferini, and R. Sailer. Remote sensing based retrieval of snow cover properties. *Cold Regions Science and Technology*, 54(3):164–175, Nov. 2008. ISSN 0165-232X. doi: 10.1016/j.coldregions.2008.07.007. URL <http://www.sciencedirect.com/science/article/pii/S0165232X08001079>.
- M. Schirmer, V. Wirz, A. Clifton, and M. Lehning. Persistence in intra-annual snow depth distribution: 1. Measurements and topographic control. *Water Resources Research*, 47(9): W09516, Sept. 2011. ISSN 1944-7973. doi: 10.1029/2010WR009426. URL <http://onlinelibrary.wiley.com/doi/10.1029/2010WR009426/abstract>.

- S. Schlögl, C. Marty, M. Bavay, and M. Lehning. Sensitivity of Alpine3d modeled snow cover to modifications in DEM resolution, station coverage and meteorological input quantities. *Environmental Modelling & Software*, 83:387–396, Sept. 2016. ISSN 1364-8152. doi: 10.1016/j.envsoft.2016.02.017. URL <http://www.sciencedirect.com/science/article/pii/S1364815216300378>.
- E. Schmucki, C. Marty, C. Fierz, and M. Lehning. Evaluation of modelled snow depth and snow water equivalent at three contrasting sites in Switzerland using SNOWPACK simulations driven by different meteorological data input. *Cold Regions Science and Technology*, 99: 27–37, Mar. 2014. ISSN 0165-232X. doi: 10.1016/j.coldregions.2013.12.004. URL <http://www.sciencedirect.com/science/article/pii/S0165232X13002036>.
- E. Schmucki, C. Marty, C. Fierz, and M. Lehning. Simulations of 21st century snow response to climate change in Switzerland from a set of RCMs. *International Journal of Climatology*, 35 (11):3262–3273, Sept. 2015. ISSN 1097-0088. doi: 10.1002/joc.4205. URL <http://onlinelibrary.wiley.com/doi/10.1002/joc.4205/abstract>.
- B. Schädler and R. Weingartner. Hydrological Atlas of Switzerland - Plate 5.4 Natural Runoff 1961 – 1980, 1992.
- J. Schöber, K. Schneider, K. Helfricht, P. Schattan, S. Achleitner, F. Schöberl, and R. Kirnbauer. Snow cover characteristics in a glacierized catchment in the Tyrolean Alps - Improved spatially distributed modelling by usage of Lidar data. *Journal of Hydrology*, 519, Part D:3492–3510, Nov. 2014. ISSN 0022-1694. doi: 10.1016/j.jhydrol.2013.12.054. URL <http://www.sciencedirect.com/science/article/pii/S002216941400016X>.
- D. Scott, J. Dawson, and B. Jones. Climate change vulnerability of the US Northeast winter recreation– tourism sector. *Mitigation and Adaptation Strategies for Global Change*, 13(5-6): 577–596, June 2008. ISSN 1381-2386, 1573-1596. doi: 10.1007/s11027-007-9136-z. URL <https://link.springer.com/article/10.1007/s11027-007-9136-z>.
- SDI-12 Support Group (Technical Committee). SDI-12 A Serial-Digital Interface Standard for Microprocessor-Based Sensors, Version 1.4, May 2017. URL <http://www.sdi-12.org/specification.php>.
- M. C. Serreze, M. P. Clark, R. L. Armstrong, D. A. McGinnis, and R. S. Pulwarty. Characteristics of the western United States snowpack from snowpack telemetry (SNOTEL) data. *Water Resources Research*, 35(7):2145–2160, 1999. ISSN 1944-7973. doi: 10.1029/1999WR900090. URL <http://onlinelibrary.wiley.com/doi/10.1029/1999WR900090/abstract>.
- B. Sevruck. Regional Dependency of Precipitation-Altitude Relationship in the Swiss Alps. In H. F. Diaz, M. Beniston, and R. S. Bradley, editors, *Climatic Change at High Elevation Sites*, pages 123–137. Springer Netherlands, Jan. 1997. ISBN 978-90-481-4890-5 978-94-015-8905-5.

Bibliography

- T. M. Shapland, R. L. Snyder, K. T. Paw U, and A. J. McElrone. Thermocouple frequency response compensation leads to convergence of the surface renewal alpha calibration. *Agricultural and Forest Meteorology*, 189–190:36–47, June 2014. ISSN 0168-1923. doi: 10.1016/j.agrformet.2014.01.008. URL <http://www.sciencedirect.com/science/article/pii/S0168192314000094>.
- S. Simoni, S. Padoan, D. F. Nadeau, M. Diebold, A. Porporato, G. Barrenetxea, F. Ingelrest, M. Vetterli, and M. B. Parlange. Hydrologic response of an alpine watershed: Application of a meteorological wireless sensor network to understand streamflow generation. *Water Resources Research*, 47(10):W10524, Oct. 2011. ISSN 1944-7973. doi: 10.1029/2011WR010730. URL <http://onlinelibrary.wiley.com/doi/10.1029/2011WR010730/abstract>.
- R. L. Snyder, D. Spano, and K. T. Pawu. Surface renewal analysis for sensible and latent heat flux density. *Boundary-Layer Meteorology*, 77(3-4):249–266, Feb. 1996. ISSN 0006-8314, 1573-1472. doi: 10.1007/BF00123527. URL <https://link.springer.com/article/10.1007/BF00123527>.
- C. G. Sommer, M. Lehning, and R. Mott. Snow in a Very Steep Rock Face: Accumulation and Redistribution During and After a Snowfall Event. *Frontiers in Earth Science*, 3, 2015. ISSN 2296-6463. doi: 10.3389/feart.2015.00073. URL <http://journal.frontiersin.org/article/10.3389/feart.2015.00073/abstract>.
- D. Spano, R. L. Snyder, P. Duce, and K. T. Paw U. Estimating sensible and latent heat flux densities from grapevine canopies using surface renewal. *Agricultural and Forest Meteorology*, 104(3):171–183, Aug. 2000. ISSN 0168-1923. doi: 10.1016/S0168-1923(00)00167-2. URL <http://www.sciencedirect.com/science/article/pii/S0168192300001672>.
- M. Spreafico and R. Weingartner. The hydrology of Switzerland. *Selected aspects and results. Reports, Bundesamt für Wasser und Geologie (BWG) Water Series*, (7), 2005.
- I. T. Stewart. Changes in snowpack and snowmelt runoff for key mountain regions. *Hydrological Processes*, 23(1):78–94, Jan. 2009. ISSN 1099-1085. doi: 10.1002/hyp.7128. URL <http://onlinelibrary.wiley.com/doi/10.1002/hyp.7128/abstract>.
- I. T. Stewart, D. R. Cayan, and M. D. Dettinger. Changes toward Earlier Streamflow Timing across Western North America. *Journal of Climate*, 18(8):1136–1155, Apr. 2005. ISSN 0894-8755. doi: 10.1175/JCLI3321.1. URL <http://journals.ametsoc.org/doi/abs/10.1175/JCLI3321.1>.
- R. B. Stull. *An Introduction to Boundary Layer Meteorology*. Springer Science & Business Media, 1988. ISBN 978-94-009-3027-8. Google-Books-ID: 2PjrCAAQBAJ.
- M. Sturm and C. Benson. Scales of spatial heterogeneity for perennial and seasonal snow layers. *Annals of Glaciology*, 38:253–260, 2004. ISSN 0260-3055, 1727-5644. doi: 10.3189/172756404781815112. URL <https://www.cambridge.org/core/journals/annals-of-glaciology/article/scales-of-spatial-heterogeneity-for-perennial-and-seasonal-snow-layers/67D46310C1A019AA959EE7D4DE1AD477>.

- W. C. Swinbank. The measurement of vertical transfer of heat and water vapor by eddies in the lower atmosphere. *Journal of Meteorology*, 8(3):135–145, June 1951. ISSN 0095-9634. doi: 10.1175/1520-0469(1951)008<0135:TMOVTO>2.0.CO;2. URL [http://journals.ametsoc.org/doi/abs/10.1175/1520-0469\(1951\)008%3C0135%3ATMOVTO%3E2.0.CO%3B2](http://journals.ametsoc.org/doi/abs/10.1175/1520-0469(1951)008%3C0135%3ATMOVTO%3E2.0.CO%3B2).
- T. Takasu and A. Yasuda. Development of the low-cost RTK-GPS receiver with an open source program package RTKLIB. In *International Symposium on GPS/GNSS, International Convention Center Jeju, Korea*, 2009.
- D. G. Tarboton. A new method for the determination of flow directions and upslope areas in grid digital elevation models. *Water Resources Research*, 33(2):309–319, 1997. ISSN 1944-7973. doi: 10.1029/96WR03137. URL <http://onlinelibrary.wiley.com/doi/10.1029/96WR03137/abstract>.
- J. E. Tillman. The Indirect Determination of Stability, Heat and Momentum Fluxes in the Atmospheric Boundary Layer from Simple Scalar Variables During Dry Unstable Conditions. *Journal of Applied Meteorology*, 11(5):783–792, Aug. 1972. ISSN 0021-8952. doi: 10.1175/1520-0450(1972)011<0783:TIDOSH>2.0.CO;2. URL <http://journals.ametsoc.org/doi/abs/10.1175/1520-0450%281972%29011%3C0783%3ATIDOSH%3E2.0.CO%3B2>.
- E. Trujillo, J. A. Ramírez, and K. J. Elder. Topographic, meteorologic, and canopy controls on the scaling characteristics of the spatial distribution of snow depth fields. *Water Resources Research*, 43(7):W07409, 2007. ISSN 1944-7973. doi: 10.1029/2006WR005317. URL <http://onlinelibrary.wiley.com/doi/10.1029/2006WR005317/abstract>.
- E. Trujillo, J. A. Ramírez, and K. J. Elder. Scaling properties and spatial organization of snow depth fields in sub-alpine forest and alpine tundra. *Hydrological Processes*, 23(11):1575–1590, 2009. ISSN 1099-1085. doi: 10.1002/hyp.7270. URL <http://onlinelibrary.wiley.com/doi/10.1002/hyp.7270/abstract>.
- E. Trujillo, N. P. Molotch, M. L. Goulden, A. E. Kelly, and R. C. Bales. Elevation-dependent influence of snow accumulation on forest greening. *Nature Geoscience*, 5(10):705–709, Oct. 2012. ISSN 1752-0894. doi: 10.1038/ngeo1571. URL <http://www.nature.com/ngeo/journal/v5/n10/full/ngeo1571.html>.
- M. T. Van Genuchten. A closed-form equation for predicting the hydraulic conductivity of unsaturated soils. *Soil science society of America journal*, 44(5):892–898, 1980. URL <https://dl.sciencesocieties.org/publications/sssaj/abstracts/44/5/SS0440050892>.
- M. Verbunt, J. Gurtz, K. Jasper, H. Lang, P. Warmerdam, and M. Zappa. The hydrological role of snow and glaciers in alpine river basins and their distributed modeling. *Journal of Hydrology*, 282(1–4):36–55, Nov. 2003. ISSN 0022-1694. doi: 10.1016/S0022-1694(03)00251-8. URL <http://www.sciencedirect.com/science/article/pii/S0022169403002518>.
- N. Vercauteren, E. Bou-Zeid, H. Huwald, M. B. Parlange, and W. Brutsaert. Estimation of wet surface evaporation from sensible heat flux measurements. *Water Resources Research*, 45(6):

Bibliography

- W06424, June 2009. ISSN 1944-7973. doi: 10.1029/2008WR007544. URL <http://onlinelibrary.wiley.com/doi/10.1029/2008WR007544/abstract>.
- D. Viviroli and R. Weingartner. The hydrological significance of mountains: from regional to global scale. *Hydrol. Earth Syst. Sci.*, 8(6):1017–1030, Dec. 2004. ISSN 1607-7938. doi: 10.5194/hess-8-1017-2004. URL <https://www.hydrol-earth-syst-sci.net/8/1017/2004/>.
- D. Viviroli, H. Dürr, B. Messerli, M. Meybeck, and R. Weingartner. Mountains of the world, water towers for humanity: Typology, mapping, and global significance. *Water Resources Research*, 43(7), 2007. ISSN 0043-1397. doi: 10.1029/2006WR005653.
- D. Viviroli, D. R. Archer, W. Buytaert, H. J. Fowler, G. B. Greenwood, A. F. Hamlet, Y. Huang, G. Koboltschnig, M. I. Litaor, J. I. López-Moreno, S. Lorentz, B. Schädler, H. Schreier, K. Schwaiger, M. Vuille, and R. Woods. Climate change and mountain water resources: overview and recommendations for research, management and policy. *Hydrol. Earth Syst. Sci.*, 15(2):471–504, 2011. ISSN 1607-7938. doi: 10.5194/hess-15-471-2011. URL <http://www.hydrol-earth-syst-sci.net/15/471/2011/>.
- C. Vögeli, M. Lehning, N. Wever, and M. Bavay. Scaling Precipitation Input to Spatially Distributed Hydrological Models by Measured Snow Distribution. *Frontiers in Earth Science*, 4, 2016. ISSN 2296-6463. doi: 10.3389/feart.2016.00108. URL <http://journal.frontiersin.org/article/10.3389/feart.2016.00108/abstract>.
- M. Warscher, U. Strasser, G. Kraller, T. Marke, H. Franz, and H. Kunstmann. Performance of complex snow cover descriptions in a distributed hydrological model system: A case study for the high Alpine terrain of the Berchtesgaden Alps. *Water Resources Research*, 49(5): 2619–2637, 2013. ISSN 1944-7973. doi: 10.1002/wrcr.20219. URL <http://onlinelibrary.wiley.com/doi/10.1002/wrcr.20219/abstract>.
- T. Watteyne, A. L. Diedrichs, K. Brun-Laguna, J. E. Chaar, D. Dujovne, J. C. Taffernaberry, and G. Mercado. PEACH: Predicting Frost Events in Peach Orchards Using IoT Technology. *EAI Endorsed Transactions on the Internet of Things*, June 2016. URL <https://hal.inria.fr/hal-01312685/document>.
- U. Wehn, M. Rusca, J. Evers, and V. Lanfranchi. Participation in flood risk management and the potential of citizen observatories: A governance analysis. *Environmental Science & Policy*, 48(Supplement C):225–236, Apr. 2015. ISSN 1462-9011. doi: 10.1016/j.envsci.2014.12.017. URL <http://www.sciencedirect.com/science/article/pii/S1462901114002457>.
- S. Weijs, R. Mutzner, and M. Parlange. Could electrical conductivity replace water level in rating curves for alpine streams? *Water Resources Research*, 49(1):343–351, 2013. ISSN 0043-1397. doi: 10.1029/2012WR012181.
- A. L. Westerling. Warming and Earlier Spring Increase Western U.S. Forest Wildfire Activity. *Science*, 313(5789):940–943, Aug. 2006. ISSN 0036-8075, 1095-9203. doi: 10.1126/science.1128834. URL <http://www.sciencemag.org/search?volume=313&submit=yes&firstpage=940>.

- N. Wever, C. Fierz, C. Mitterer, H. Hirashima, and M. Lehning. Solving Richards Equation for snow improves snowpack meltwater runoff estimations in detailed multi-layer snowpack model. *The Cryosphere*, 8(1):257–274, 2014. ISSN 1994-0424. doi: 10.5194/tc-8-257-2014. URL <http://www.the-cryosphere.net/8/257/2014/>.
- N. Wever, L. Schmid, A. Heilig, O. Eisen, C. Fierz, and M. Lehning. Verification of the multi-layer SNOWPACK model with different water transport schemes. *The Cryosphere*, 9(6):2271–2293, Dec. 2015. ISSN 1994-0424. doi: 10.5194/tc-9-2271-2015. URL <http://www.the-cryosphere.net/9/2271/2015/>.
- N. Wever, F. Comola, M. Bavay, and M. Lehning. Simulating the influence of snow surface processes on soil moisture dynamics and streamflow generation in an alpine catchment. *Hydrol. Earth Syst. Sci.*, 21(8):4053–4071, Aug. 2017. ISSN 1607-7938. doi: 10.5194/hess-21-4053-2017. URL <https://www.hydrol-earth-syst-sci.net/21/4053/2017/>.
- J. M. Wilczak, S. P. Oncley, and S. A. Stage. Sonic Anemometer Tilt Correction Algorithms. *Boundary-Layer Meteorology*, 99(1):127–150, Apr. 2001. ISSN 0006-8314, 1573-1472. doi: 10.1023/A:1018966204465. URL <https://link.springer.com/article/10.1023/A:1018966204465>.
- T. S. Winchell, D. M. Barnard, R. K. Monson, S. P. Burns, and N. P. Molotch. Earlier snowmelt reduces atmospheric carbon uptake in midlatitude subalpine forests. *Geophysical Research Letters*, 43(15):2016GL069769, 2016. ISSN 1944-8007. doi: 10.1002/2016GL069769. URL <http://onlinelibrary.wiley.com/doi/10.1002/2016GL069769/abstract>.
- A. Winstral, D. Marks, and R. Gurney. Simulating wind-affected snow accumulations at catchment to basin scales. *Advances in Water Resources*, 55:64–79, 2013. ISSN 0309-1708. doi: 10.1016/j.advwatres.2012.08.011. URL <http://www.sciencedirect.com/science/article/pii/S0309170812002394>.
- S. Wipf, V. Stoeckli, and P. Bebi. Winter climate change in alpine tundra: plant responses to changes in snow depth and snowmelt timing. *Climatic Change*, 94(1-2):105–121, May 2009. ISSN 0165-0009, 1573-1480. doi: 10.1007/s10584-009-9546-x. URL <https://link.springer.com/article/10.1007/s10584-009-9546-x>.
- M.-K. Woo. Snowmelt Runoff Generation. In *Encyclopedia of Hydrological Sciences*. John Wiley & Sons, Ltd, 2006. ISBN 978-0-470-84894-4.
- WSL Institute for Snow and Avalanche Research SLF. WFJ_mod: Meteorological and snowpack measurements from Weissfluhjoch, Davos, Switzerland. 2015. doi: 10.16904/1. URL <http://dx.doi.org/10.16904/1>.
- WSL Institute for Snow and Avalanche Research SLF. Weissfluhjoch test site, 2018. URL <https://www.slf.ch/en/about-the-slf/instrumented-field-sites-and-laboratories/flaechen-und-anlagen-fuer-schnee-und-eis/weissfluhjoch-test-site.html>.
- S. Würzer, N. Wever, R. Juras, M. Lehning, and T. Jonas. Modeling liquid water transport in snow under rain-on-snow conditions - considering preferential flow. *Hydrology and Earth System*

Bibliography

- Sciences Discussions*, pages 1–29, Aug. 2016. ISSN 1812-2116. doi: 10.5194/hess-2016-351. URL <http://www.hydrol-earth-syst-sci-discuss.net/hess-2016-351/>.
- S. Yamaguchi, K. Watanabe, T. Katsushima, A. Sato, and T. Kumakura. Dependence of the water retention curve of snow on snow characteristics. *Annals of Glaciology*, 53(61):6–12, 2012. URL <http://www.ingentaconnect.com/content/igsoc/agl/2012/00000053/00000061/art00002>.
- M. Zappa, F. Pos, U. Strasser, P. Warmerdam, and J. Gurtz. Seasonal Water Balance of an Alpine Catchment as Evaluated by Different Methods for Spatially Distributed Snowmelt Modelling. *Hydrology Research*, 34(3):179–202, June 2003. ISSN 0029-1277, 2224-7955. URL <http://hr.iwaponline.com/content/34/3/179>.

Tristan Brauchli

Chemin des Retraites 6
1004 Lausanne, Switzerland
☎ +41 76 527 53 97
✉ tristan.brauchli@gmail.com
Swiss nationality, 05.10.1984

Work experience

- 2013-2018 **PhD student in EDCE Civil and Environmental Engineering**, *Laboratory of Cryospheric Sciences CRYOS, École Polytechnique Fédérale de Lausanne, EPFL, Lausanne.*
- Study and modeling (*Alpine3D*) of snow ablation and its impact on runoff in the Dischma river basin (GR).
 - Analysis of the spatio-temporal snowmelt with the help of a Terrestrial Laser Scanner (TLS). Acquisition, post-processing and analysis of the data.
 - Analysis of the Sensible Heat Flux between the land surface and the atmosphere.
 - Deployment of different instruments (snow lysimeters, 3D Sonic anemometers, water level gauges) in the field.
 - Teaching assistantship in Physics and Hydrology of Snow, Physics and Chemistry of the Atmosphere (practical work), Fluid Mechanics (practical work).
- 2009-2013 **Specialist in hydrological forecast**, *Hydrique Ingénieurs, Le Mont-sur-Lausanne.*
- Operational management of several river forecast systems (flood, energy production).
 - Development and improvement of a hydrological model in mountainous area.
 - Flood management studies (Valais, Fribourg).
- 09/2008-03/2009 **Internship in the field of meteorology**, *Service des Routes et Cours d'Eau, Etat du Valais (in collaboration with MeteoSwiss Geneva), Sion.*
- Analysis of critical meteorological conditions related to floods in Canton Valais.
- 10/2003-07/2004 **Collaborator**, *CSD Ingénieurs Conseils SA, Lausanne.*
- Work in the field of the environment (traffic impact study, landscape impact assessment, energy balance).

Education

- 2007-2009 **Msc in Environmental Sciences**, *Eidgenössische Technische Hochschule Zürich, ETHZ, Zürich, Switzerland.*
- Major in Atmosphere and Climate
 - Minor in Physical Glaciology
- 2004-2007 **BSc in Environmental Sciences and Engineering**, *École Polytechnique Fédérale de Lausanne, EPFL, Lausanne, Switzerland.*

Computer skills

Programming Python, R, Shell, Matlab, C++, VB.NET
Office suite Latex, OpenOffice, Microsoft
GIS software Quantum GIS, ArcGis, MySQL, SQLite

Languages

French **mother tongue.**
English **professional working proficiency, level C1.**
German **spoken and written, level B2.**

Others

Photography, electronics tinkering
Cycling and mountain activities (hiking, ski touring, snowboarding)
Driving license (Category B, D1, BE, D1E)

